Improvement in Mechanical Properties through Structural Hierarchies in Bio-Inspired Materials

by

Dipanjan Sen

B.Tech., Mechanical Engineering
Indian Institute of Technology Delhi (2002)
M. S., Materials Science and Engineering
Ohio State University (2005)

Submitted to the Department of Materials Science and Engineering
in partial fulfillment of the requirements for the degree of

Doctor of Philosophy

at the

MASSACHUSETTS INSTITUTE OF TECHNOLOGY

February 2011

Author .....
Department of Materials Science and Engineering
Dec 9, 2010

Certified by .....
Markus J. Buehler
Associate Professor of Civil and Environmental Engineering
Thesis Supervisor

Accepted by .....
Christopher Sc
Chair, Departmental Committee on Graduate Stude...

Improvement in Mechanical Properties through Structural Hierarchies in Bio-Inspired Materials

by

Dipanjan Sen

Submitted to the Department of Materials Science and Engineering
on Dec 9, 2010, in partial fulfillment of the
requirements for the degree of
Doctor of Philosophy in the field of Material Science and Engineering

Abstract

Structural biological materials such as bone, nacre, insect cuticle, and sea sponge exoskeleton showcase the use of inferior building blocks like proteins and minerals to create structures that afford load-bearing and armor capabilities. Many of these are composite structures that possess the best of the properties of their base constituents. This is in contrast to many engineering materials, such as metals, alloys, ceramics and their composites which show improvement in one mechanical property (e.g. stiffness) at the cost of another disparate one (e.g. toughness). These excellent design examples from biology raise questions about whether similar design, and improvement in disparate properties, can be achieved using common engineering materials. The identification of broad design principles that can be transferred from biological materials to structural design, and the analysis of the utility of these principles have been missing in literature. In this thesis, we have firstly identified certain universal features of design of biological structures for mimicking with engineering materials: a) presence of geometric design at the nanoscale, b) the use of mechanically inferior building blocks, and c) the use of structural hierarchies from the nanoscale to the macroscale. We firstly design, *in silico*, metal-matrix nanocomposites, mimicking the geometric design found at the nanoscale in bone. We show this leads to improvements in flow strength of the material. A key finding is that limiting values of certain of these parameters shuts down dislocation-mediated plasticity leading to peak in flow strength of the structure. Metals are however, costly constituents, and we next confront the issue of whether it is possible to use a single mechanically inferior and commonly available constituent, such as silica, to create superior bio-inspired structures. We turn to diatom exoskeletons, protective armor structures for algae made almost entirely of silica, and create nanoporous silica structures inspired from their geometry. We show large improvements in ductility of silica through this design, facilitated by a key size-dependent brittle-to-ductile deformation transition in these structures. Nanostructuring, while improving ductility, affects the stiffness of these structures, softening them by up to 90% of bulk silica. Hierarchical assembly of silica structures is then used to regain the stiffness lost due to nanostructuring

while not losing their improvement in toughness. Finally, improvement in toughness with several levels of hierarchy is studied, to showcase a defect-tolerant behavior that arises with the addition of hierarchies, *i.e.*, tolerance of the fracture strength to a wide range of sizes of cracks present in the structure. The importance of R-curve behavior, *i.e.*, toughness change with the advance of a crack in the structure, to the defect-tolerance length scale is also established. These findings showcase the validity of using design principles obtained from biological materials for improvement in mechanical properties of engineering materials.

Thesis Supervisor: Markus J. Buehler
Title: Associate Professor of Civil and Environmental Engineering

Acknowledgments

I would like to take this opportunity to express my heartfelt gratitude to many who have supported me throughout my graduate studies at MIT. First, I am indebted to my advisor, Professor Markus Buehler, for his mentorship, advice and support during my PhD. Discussions and brain-storming sessions with him have been a great source of learning and inspiration for me. I am also grateful to my peers in my research group for their friendship, discussions, and collaborations; Sinan Keten, Theodor Ackbarow, Zhiping Xu, Andre Garcia, Jeremie Bertaud, Steve Cranford, Zhao Qian, Raffaella Paparcone, Graham Bratzel, and Rouzbeh Shahsavari. I would like to thank my collaborators from various labs and universities; Prof. Christian Thaulow, Prof. Pedro Reis, and Dr. Kostya Novoselov. Brainstorming, discussing research and writing papers with them have shown me the true value of collaborative research. I would also like to thank my UROPs and other undergraduate assistants, working with whom on short projects has been a great teaching and learning experience for me.

The rigor of a doctoral work could not have been undertaken without the constant support of my friends here. I am grateful to my roommates, Sukant Mittal, Srikanth Patala and Vivek Inder Sharma who have stuck by me through thick and thin. Coffee breaks, and discussions with Srujan Linga, Deep Ghosh, Vivek Ragunathan and Sumeet Kumar on every topic under the sun have always helped in breaks from research work.

Finally, I express my deepest gratitude to my family, who have supported and encouraged me in all my academic endeavors. I am humbled by the sacrifices made by my parents, so that I could have a better education and access to world-class opportunities.

This research was funded by grants by the Army Research Office (W911NF-06-1-0291), as well as the UROP office at MIT. Their support is greatly appreciated.

Dedicated to my parents, Sukla Sen and Siba Prasad Sen.

Contents

List of journal publications

1. **D. Sen**, A. P. Garcia, and M. J. Buehler, "Mechanics of nano-honeycomb silica structures: A size-dependent brittle-to-ductile transition", in review.

2. A. P. Garcia, **D. Sen**, and M. J. Buehler, "Hierarchical silica nanostructures inspired by diatom algae yield superior deformability, toughness and strength", *Metallurgical and Materials Transactions A*, accepted.

3. **D. Sen**, and M. J. Buehler, "Atomistically-informed mesoscale model of deformation and failure of hierarchical silica nanocomposites", *International Journal of Applied Mechanics*, 2010, 2(4).

4. **D. Sen**, C. Thaulow, S. V. Schieffer, A. Cohen, and M. J. Buehler, "Atomistic Study of Crack-Tip Cleavage to Dislocation Emission Transition in Silicon Single Crystals", *Physical Review Letters*, 2010, 104: p. 235502.

5. **D. Sen**, K. Novoselov, P. Reis, and M. J. Buehler, "Tearing graphene sheets from adhesive substrates produces tapered nanoribbons", *Small*, 2010, 6(10): p. 1108. (Cover article)

6. R. Jack, **D. Sen**, and M. J. Buehler, "Graphene nanocutting through nanopatterned vacancy defects", *Journal of Computational and Theoretical Nanoscience*, 2010, 7: p. 354-359.

7. **D. Sen**, and M.J. Buehler, "Size and Geometry Effects on Flow Stress in Bioinspired de novo Metal-matrix Nanocomposites", *Advanced Engineering Materials*, 2009, 11(10): p. 774.

8. S. Cranford, **D. Sen**, and M. J. Buehler, "Meso-Origami: Folding Multilayer Graphene Sheets". *Applied Physics Letters*, 2009, 95: p. 123121.

9. T. Ackbarow, **D. Sen**, C. Thaulow and M. J. Buehler, "Alpha-Helical Protein Networks Are Self-Protective and Flaw-Tolerant", *PLoS ONE*, 2009, 4(6): p. e6015.

10. **D. Sen**, and M.J. Buehler, "Crystal size controls deformation mechanism: Breakdown of dislocation mediated plasticity at nanoscale", *Physical Review B*, 2008, 77: p. 195439.

11. **D. Sen** and M.J. Buehler, "Shock loading of bone-inspired metallic nanocomposites". *Solid State Phenomena*, 2008, 139: p. 11-12.

12. M. J. Buehler, A. Cohen, and **D. Sen**, "Multi-paradigm modeling of fracture of a silicon single crystal under mode II shear loading", *Journal of Algorithms and Computational Technology*, 2008, 2(2): p. 203-221.

13. **D. Sen** and M.J. Buehler, "Simulating chemistry in mechanical deformation of metals", *International Journal for Multiscale Computational Engineering*, 2007, 5(3-4): p. 181-202.

List of Figures

List of Tables

Chapter 1

Background

1.1 Optimizing mechanical properties: learning from nature

There exist several natural materials with exceptional mechanical properties. Silk has a strength per unit weight larger than steel; bone, nacre and sea shell have excellent toughness properties given their weak and brittle constituents (hydroxyapatite, silica, protein). Several of these structural biological materials are composites, with very good deformation-resisting and load-carrying capacities. The composite constituents are usually different proteins, such as collagen or chitin, and minerals such as calcite, aragonite and hydroxyapatite. These composites are typically lightweight, but possess an unusual stiffness, strength, toughness and fatigue resistance for their composition and weight. Very importantly, the final material properties are seen to be a combination of the best properties of the base constituents and cannot be approximated a rule-of-mixtures calculations of their base material properties [1]. Most engineering analogs, on the other hand, show the characteristic 'banana-curve' type behavior, that is, they do not enable the combination of high levels of strength, stiffness and toughness (Figure 1-1).

There is nothing remarkable about the mechanical properties of the individual constituents of these natural materials. Hydroxyapatite or silica possess fracture

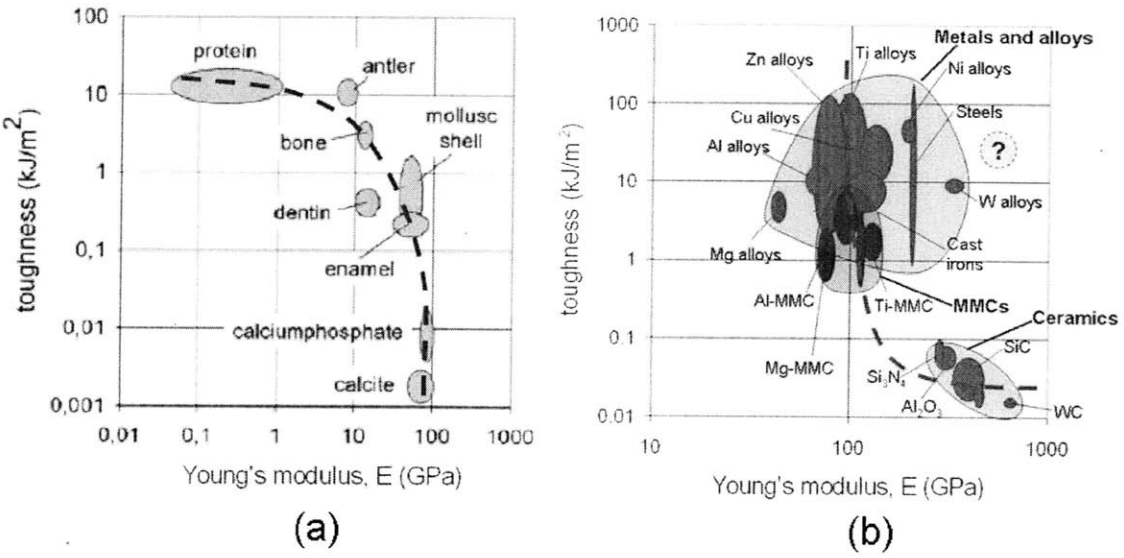

Figure 1-1: (a) Toughness versus stiffness for a number of biological materials (based on the data compilation in [2]. Biological composites, such as antler, dentin, bone and enamel combine the good properties of the protein and mineral components and are typically both stiff and tough. Generally speaking, the stiffness increases and the toughness decreases with mineral content from antler to dentin/bone and enamel [3]; (b) Toughness vs. stiffness for metals, alloys, ceramics, and metal-matrix composites (MMC), lie on the 'banana-curve', an inverse relation between increasing toughness and decreasing stiffness. The circular yellow region shows the property region of high toughness and stiffness that may be accessible through designing bio-inspired composite structures. Figure adapted from [4].

toughness much like man-made ceramics, proteins have stiffness close to synthetic polymers. It is thus to be reasoned that it is the structure and geometry of these materials that give rise to excellent properties. A key common feature of these composite biological materials seen is the presence of remarkable designs with building blocks, often hierarchically arranged from the nanometer to the macroscopic length scales [5, 6, 7] that give rise to excellent properties. Every structural level (hierarchy) is postulated to contribute to the mechanical stability and properties of the resulting design. This endows them with a far greater level of structural complexity and organization than synthetic composites. However, the extent to which the presence of hierarchies quantitatively affects structural properties is not clearly understood, and a broad framework for studying structural hierarchies is missing in prior literature. Hierarchical organizations have already been studied in numerous fields far removed from structural materials, e.g. ecology, transportation, and engineering control systems [8, 9, 10], and recent attempts to draw parallels from these fields to the study of hierarchies in biological structures point to exciting, uncharted territories in the study of structure of biological materials [11, 12, 13].

An application of this emerging science would be in the design of synthetic hierarchical materials [14]. The materials used can be based on metals, ceramics, polymers and proteins [15, 16, 17, 18]. The broad vision would be to design these materials using a bottom-up approach, starting at the nanoscale, and building in structure, as the length scale is increased. The design at the lowest length scales (nano- to micro-) is particularly suited for computational nanoscale experiments, as carried out through molecular dynamics (MD) and mesoscale simulations. Atomic scale molecular dynamics simulations have been used previously to probe size-scale and temperature scale effects in the deformation of nanomaterials, often providing design templates [19, 20, 21].

Many of these biological materials are seen to possess the following design features: a) use of inferior base constituent materials, (b) composite sub-structure starting at nanoscale dimensions; and (c) hierarchical arrangement of structure from nanoscale to macroscale. We describe what hierarchies are in the next section and provide a

few examples.

1.2 Structural hierarchies in nature

Structural hierarchies in natural biological materials are defined as the quality of certain materials possessing structure and organization at several levels of length scale [22, 23]. A natural definition of hierarchical systems arises from the field of systems theory [24, 25], where they are defined as composition of stable, observable sub-elements that are unified by a super-ordinate relation [8]. The stability of sub-elements at different levels makes them building blocks for the next higher level. Averaging or coarse-graining of properties over one hierarchy level to derive information for the next higher level is usually not feasible, owing to linking of behavior across several levels, unless there is a large separation of length scales across successive levels [22].

A key feature of hierarchical biological systems, structural or otherwise, is their *robustness*. Robustness has been studied by systems scientists for biological systems and classified in the following ways: (a) adaptation - the ability to cope with external changes, (b) parameter insensitivity, and (c) graceful degradation- slow degradation of a system's function after damage, rather than catastrophic failure [25]. Hierarchical systems in biology, studied from a system-theoretic point of view show optimality of several properties and robustness, at the same time [11]. Hierarchical systems also show improved behavior (optimality) over a large number of mechanical properties simultaneously, as compared to their base elements at the lowest level of hierarchy. Whether individual properties are improved by design elements at individual levels of hierarchy, or arise from a combination of properties at different scales is debatable (e.g. see Section 1.3, "Effect of hierarchies on failure across length scales").

Here, we provide two examples of hierarchical structural geometries. Human cortical bone [26] is seen to be composed of 7 structural levels of hierarchical arrangement and possesses excellent strength and toughness properties while being lightweight. This is thus an ideal material to mimic for high toughness applications, while probing

effect of hierarchies on mechanical properties. Bone is a composite of organic and inorganic constituents: 30% bone, by weight, is organic: of which 90-95% is collagen, rest is non-collagenous proteins. At the nanoscale, bundles of collagen molecules are arranged in fibrils, which are twisted in a coil (fiber). 70% of bone is made up of the inorganic mineral hydroxyapatite, which includes calcium phosphate, calcium carbonate, calcium fluoride, calcium hydroxide and citrate. This inorganic component ($([Ca_3(PO)_4)_2]_3 \bullet Ca(OH)_2)$) is predominantly crystalline. The crystals are platelets or rods, about 8 to 15 Å thick, 20 to 40 Å wide and 200 to 400 Å long and arranged in a regular array at the nanoscale (see Figure 1-2). The mineralized collagen fibers form planar arrangements called lamellae (3-7 μm wide). These sheets (lamellae) of mineralized collagen fibers wrap in concentric layers around a central canal to form osteons. Osteons appear like cylinders ≈200-250 μm in diameter running parallel to the long axis of the bone. Figure 1-2 shows all these levels of hierarchy in bone from the nanoscale up to the macroscale.

Diatom exoskeletons are a composite of 97% silica and remaining 3% protein material such as silicateins. The structure consists of 4 levels of hierarchy. At the nanoscale is the basic constituent, biosilica, made of fused silica nanospheres connected via an organic matrix. This biosilica is designed into a porous nanostructure, the cribellum, at the smallest assembly scale, in a regular lattice arrangement of pores with pore diameters ≈45 nm and distances ≈68 nm. The second layer, the cribrum possesses a hexagonal porous structure with larger pore sizes of ≈200 nm. The largest porous layer, the areola has a pore size of ≈1.1 μm [27].

The importance of hierarchical design to improving divergent mechanical properties in biological applications has been proposed by many authors. For example, the structural hierarchy seen in skeleton of sea sponge [28, 29, 30] is supposed to be responsible for its high strength and crack resistance despite being made almost completely of brittle silica. Hierarchical arrangements in protein structures from amino acids up to secondary structures, have been proposed as an arrangement for improving robustness of the structures [13]. Hierarchical assembly thus might hold the key to scaling up excellent mechanical properties seen in many synthetic nanoma-

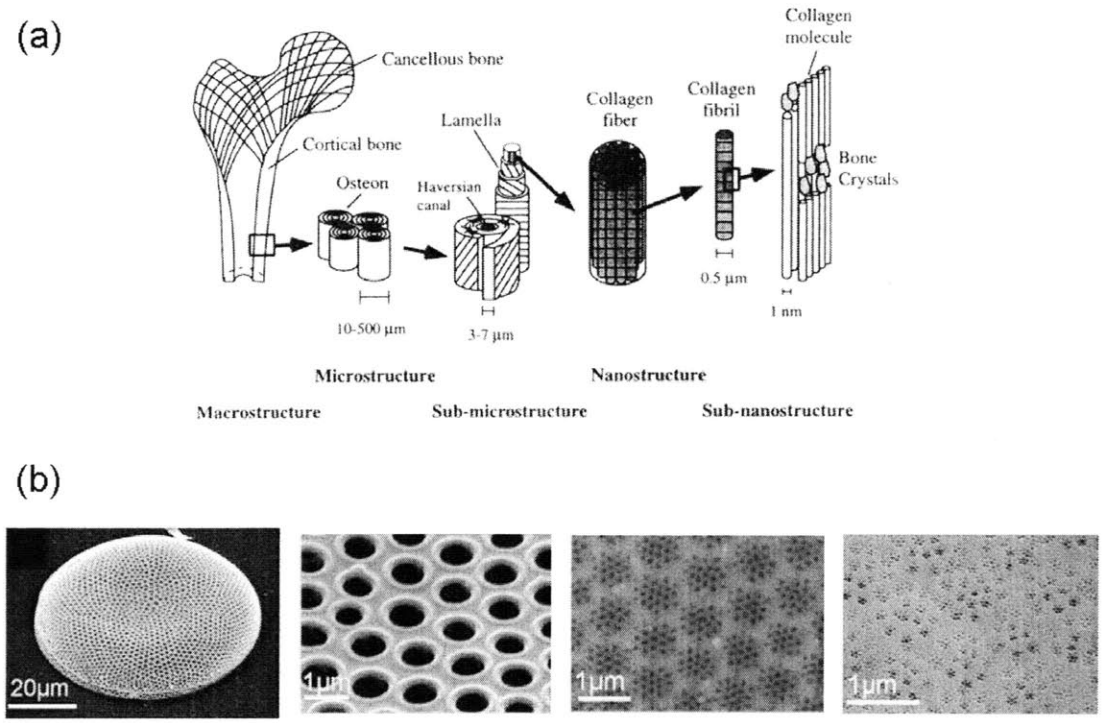

Figure 1-2: Structural hierarchies in two different biological materials, (a) bone, showing from left to right, cortical and cancellous bone (different types of bone); osteons; lamellae; collagen fiber assemblies of collagen fibrils; bone mineral crystals, collagen molecules, and non-collagenous proteins (Figure reproduced from [1]); and (b), marine diatom species (*Concinodicus* sp.), a silica-based exoskeleton (called frustule) made up of porous parts arranged in a hierarchical fashion, showing, from left to right, the whole frustule member (external surface of the diatom); areola pores, the internal surface of the diatom; the 2nd central porous layer, the cribrum; the cribellum, the external porous layer. The three layers are arranged on top of each other (Figure reproduced from [27]).

terials up to macroscale engineering structures. Carbon nanotubes, graphene, metal nanowires have excellent strength but cannot be presently used in engineering structures because the procedure for connecting disparate length scales while maintaining nanoscale properties remains unknown [31].

1.3 Effect of hierarchies on failure across length scales

Loading and fracture experiments on structural biological materials have revealed a complex set of mechanisms across wide length scales. The question of which are the dominant mechanisms in the failure of a particular material, and, are hierarchies and the multiple scale mechanisms they engender, essential for the improved fracture properties, are still hotly debated. Experimentally, this is difficult to observe because of the difficulty of testing substructures of a material at different length scales, and the problem with separating the contribution of different mechanisms to the overall toughness. Here, we briefly review the experimental evidence of effect of hierarchies on failure in two biological systems with different basal components, bone (hydroxyapatite-based) and diatoms (silica-based). These materials are chosen as two representative systems which we will use as design templates using engineering materials in later sections of the thesis.

A major property of bone is its fracture resistance and toughness. This has been attributed to distinct mechanisms on different length scales by various authors. On the micron length scale, where the bone structure consists of osteons, this has been attributed to two mechanisms (a) crack bridging and (b) microcracking [32]. On the nanometer length scale, this has been attributed to flaw tolerance of size of mineral platelets [33]. The modular domain nature of the organic matrix at different scales, and its stepwise unfolding has been proposed as a mechanism for the intrinsic toughness of the protein matrix [34]. Below we provide brief descriptions of both mechanisms.

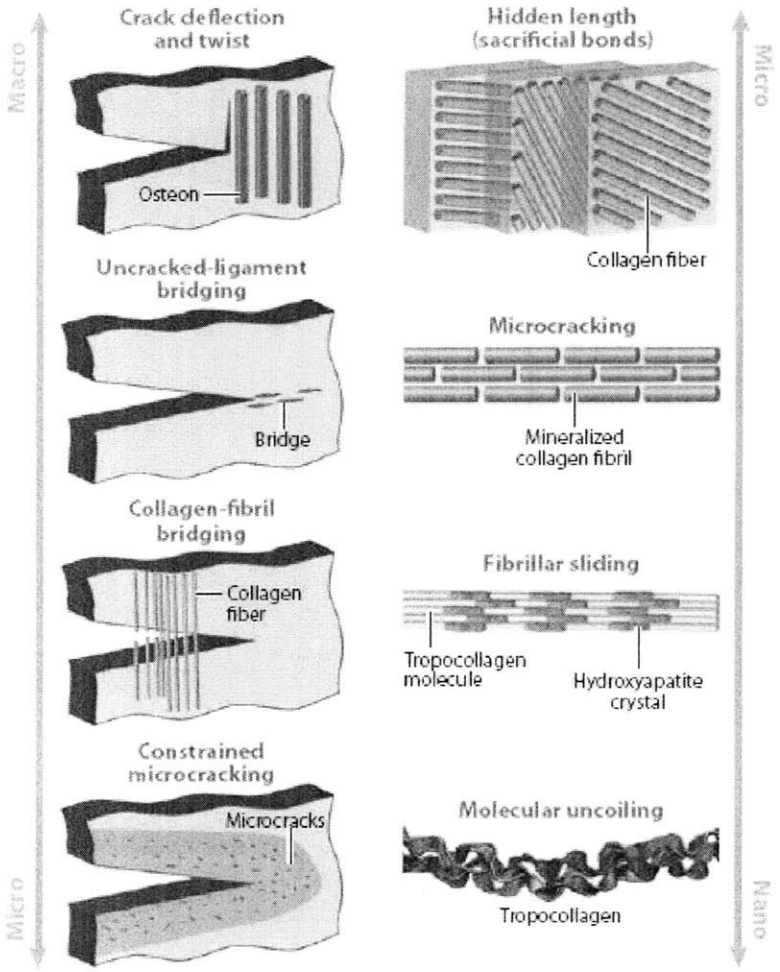

Figure 1-3: Toughening mechanisms exist at different levels of hierarchy in bone. These are molecular uncoiling and sliding at the protein domain level, and flaw-tolerance at the individual hydroxyapatite crystal level, microcracking, crack-bridging, and crack deflection at the larger scales. Figure reproduced from [35].

From critical stress intensity factor (K_{Ic}) studies of bending loading of notched bone specimen to failure, formation of microcracks are seen, which are of the order of osteons in length. It is hypothesized that microcracks tend to originate around osteons due to debonding at osteon-matrix interface or osteon pull-out. The presence of microcracks in the wake of a crack have been shown to result in the residual opening of the crack tip, and a redistribution of stresses in the crack tip region, which reduces the crack extension force and increases the toughness of the material. Crack bridging in the wake of a crack has also been proposed as a crack tip shielding mechanism. Crack bridging involves formation of unbroken regions that span the crack in the wake of the crack tip and act to resist crack opening. Such bridging can results from uncracked ligaments and intact collagen fibrils. Both these mechanisms thus reduce crack propagation, and the dominant mechanism is still under debate [32].

Another research direction has been considering the characteristic nanostructure of bone, a geometric motif that is common to other hard structural biomaterials such as nacre and dentin. The nanostructure of bone is seen in Figure 1-2, consisting of mineral platelets arranged in a staggered pattern in a collagen matrix. The commonality of this structural motif across structural materials suggests some intrinsic properties in the design that improve mechanical properties. A mechanism has been proposed by Gao, Fratzl *et al.* [36] whereby under tensile loading, staggered mineral platelets carry tensile load and the protein matrix transfers the load between mineral crystals via shear. The fracture toughness of the composite depends on the tensile strength of the mineral platelets. It has been showed that the nanoscale width of the mineral platelets embedded in the collagen matrix is such that the material becomes insensitive to crack like flaws at this length scale (approximately 30 nm) and fails under tension at the theoretical strength for a perfect crystal [33]. When the mineral size exceeds a length scale of order of 30 nm, fracture strength is sensitive to structural size. This concept is called the flaw tolerance of size of mineral platelets. The theory claims that the size of mineral platelets in bone is optimized at this flaw tolerant size. The optimum aspect ratio (height/width) of these platelets can be obtained by assuming that protein and mineral fail at the same time. However,

major shortcomings of this simplified model are that it fails to take into account the complex non-stoichiometric chemistry at mineral-protein interfaces [37, 38] and size limitations of mineral owing to the same.

Diatom algae form a very different kind of protective exoskeleton. This protective covering is porous and made of up to 97% silica. Several studies reported in the recent literature have revealed the mechanical properties of diatom shells. Hamm *et al.* [39] used a glass needle to load and break diatom frustules in order to probe their mechanical response at failure, and found high strength (between ≈1 and 7 MPa compressive stress for fracture) and reversible elastic strains (e.g. 2.5% reversible strain in a frustule section). A three-dimensional finite-element model of the frustule in the same work showed that the highest stresses within the frustule before failure was ≈540 MPa. The geometric design of the frustule led to the applied external pressures creating homogeneous stress distributions within the structure. Other researchers [40, 41] have used AFM nanoindentation to study the nanoscale material properties of the porous frustule layers of diatoms, identifying pore sizes on the order of several tens of nanometers at the smallest levels in the hierarchy, with ultra-thin silica walls on the order of several nanometers. They observed that the variation of mechanical properties between the hierarchical frustule layers could be influenced by the pore size, pore distance, porosity, and under different biomineralization processes.

This brief review of the physics of toughness and fracture strength of bone and diatoms show the importance of hierarchical levels in optimizing mechanical properties. Structures at very different length-scales have been seen to play a prominent role in their stiffness, strength and toughness [32, 33, 41].

1.4 Aim of study: hypotheses

The aim of this thesis is the investigation of the effect of mimicking certain universal features found in biological structural materials, and to assess their potential for use in the design of engineering materials. The key hypotheses are that these universal features that can be transferred to the design of engineering materials are:

(a) geometric design at the ultimate scale (nanostructure) of biological structure, with the underlying effects on deformation mechanisms at the nanoscale,

(b) the use of mechanically inferior constituent materials,

(c) attempting bottom-up design with hierarchical molecular-scale (nm) assemblies up to macroscale (mm/cm) dimensions.

The particular individual materials used in the design is not the important concept, rather it is differentiating the requirement of nanostructuring and hierarchical assembly in the improvement of mechanical properties. Addressing these issues by laying out a computational and theoretical framework is the fundamental goal of this thesis.

1.5 Approach

The scope of our study lends itself to the use of bottom-up computational simulations as a design and analysis tool. Figure 1-4 shows computational methods across size and time scales that are available in the computational mechanics literature.

In this thesis, we study the mechanical properties at the nanoscale using atomistic simulations, and at the sub-micron and micro-scale using mesoscale modeling. These methods are outlined in greater detail in Chapter 2.

1.6 Outline

The content of this thesis is arranged as follows: Chapter 2 outlines all of the computational methods used in this thesis, from the atomistic to multiscale modeling approaches. It also provides some background on the analysis techniques, and visualization methods used. In chapter 3, we take inspiration from the design of bone nanostructure and describe the design and mechanical properties of a metal-matrix nanocomposite based on it. Metals, however, are costly materials to use as constituents. Is it possible to use cheaper and more readily available materials as build-

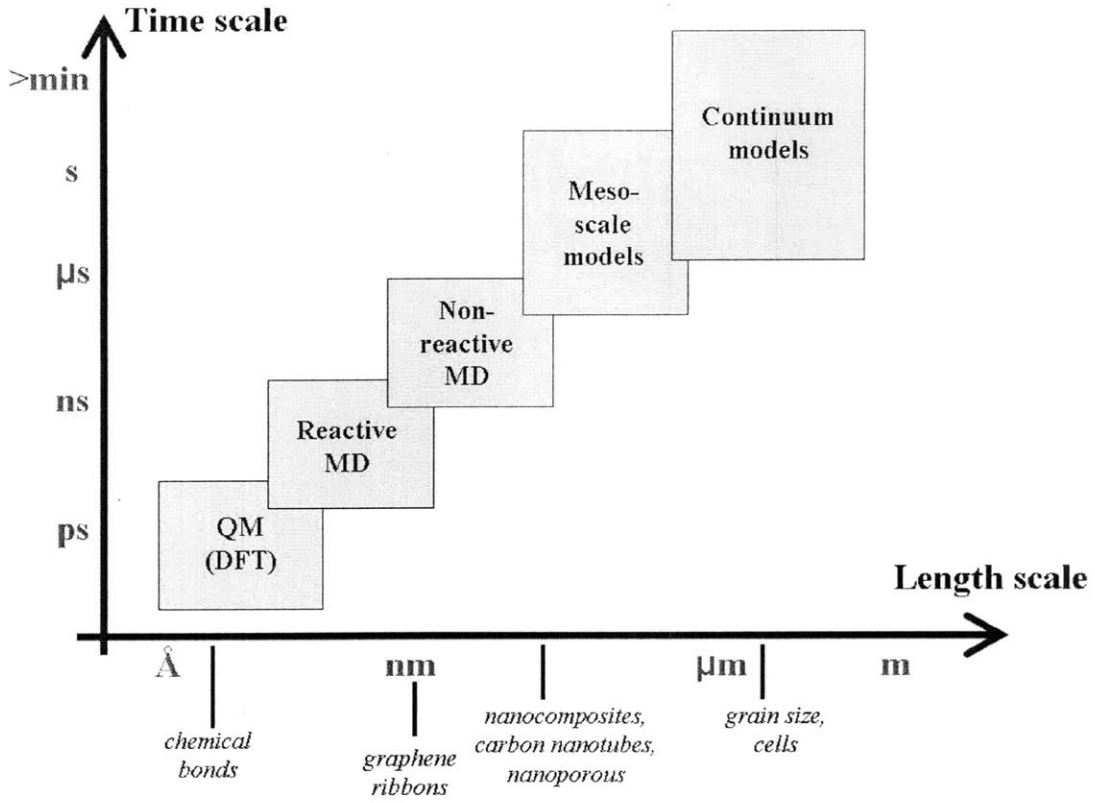

Figure 1-4: Overview of computational methods across scales, scanning from quantum calculations at the Angstrom scale to continuum models at the meter scale. Multiscale coupling of methods can be used to traverse through a wide range of time- and length scales. Figure adapted from [42].

ing blocks, such as silica, abundantly found in sand? Bulk silica, however, is a 'weak' material for structural purposes, due to low toughness and brittle failure behavior. We tackle the problem of enhancing the ductility of silica in chapter 4, by taking inspiration from a silica-based biomaterial, the diatom, and describe the design and mechanical properties of a nanoporous silica structure inspired from its nanostructure. The next question is how to measure the mechanical properties of hierarchical structures built from the bottom-up using these nanostructures, and we proceed, in Chapter 5, to develop a mesoscale modeling method to describe the mechanics of hierarchical silica nanocomposites. Chapter 6 describes the use of this mesoscale method in measuring toughness improvements over several levels of hierarchy. Chapter 7 summarizes major findings of this thesis, and provides an outlook for future research.

Chapter 2

Methodology

In this Chapter, a brief overview of computational techniques used in this work is presented. The focus is on computational methods to study mechanical behavior of materials, and they are classified here by the length scales accessible to the different methods. Firstly, different schemes of atomistic simulations are reviewed which can access nanometer and sub-nanometer length scales. Then we cover multiscale modeling methods which can access sub-micron and micron length scales. In the next section, we establish the link between the data from atomistic and mesoscale simulations and material properties measured at a continuum level. Finally, visualization techniques and packages are covered.

2.1 Atomistic modeling

This section describes the atomistic modeling approaches used in this thesis. Particular emphasis is given to the molecular dynamics method and its variants. An extensive discussion of atomistic force fields, which are a key factor in the success of any atomistic simulation, is also undertaken. Finally, scaling and computational limitations of atomistic modeling are briefly touched upon.

2.1.1 Classical molecular dynamics

Molecular dynamics (MD) is a computer simulation tool for studying the real-time motion of a group of atoms or molecules under their mutual interactions for a certain period of time. Since its development in the late 1950s [43, 44], it has been used to simulate groups of atoms in sizes from a few to several billions recently, and over a time of femtoseconds (fs) to fractions of microseconds. It has found several applications in materials science, chemistry, solid-state physics, fluid mechanics, biomechanics and other fields. In the field of materials science, the MD method is capable of capturing atomistic mechanisms that play a key role in several materials phenomena e.g. deformation, fracture, diffusion, chemical reactions, self-assembly, and phase transformations.

The core requirement for an atomistic simulation using MD is a (2-body to multi-body) atom interaction potential or force description. This is a coarser system description than the use of *ab-initio* quantum methods [45] to describe atomic interactions that allows an accurate description of ground-state and excited-electronic states of a group of atoms, leading to *ab-initio* molecular dynamics. However, *ab-initio* methods are hugely expensive in terms of computational time and power, and can only be used for systems with a few 100 atoms. What we will discuss further is classical molecular dynamics, where the ground-state of the system is used to obtain an atomic interaction potential, losing all electronic states information. The atomistic potentials can however be designed to capture reactions and bond making or breaking events. The main idea then is to compute the dynamical trajectory of each atom in the group, considering their atomic interaction potentials, by solving each atom's equation of motion according to $F = ma$, where F, m and a are force, mass and acceleration respectively, leading to atomic positions $r_i(t)$, velocities $v_i(t)$ and accelerations $a_i(t)$ for the ith atom. The numerical integration of Newton's law by considering proper interatomic potentials to obtain interatomic forces enables one to simulate a small/ large group of atoms. The basic concept of molecular dynamics is shown in Figure 2-1(a,b).

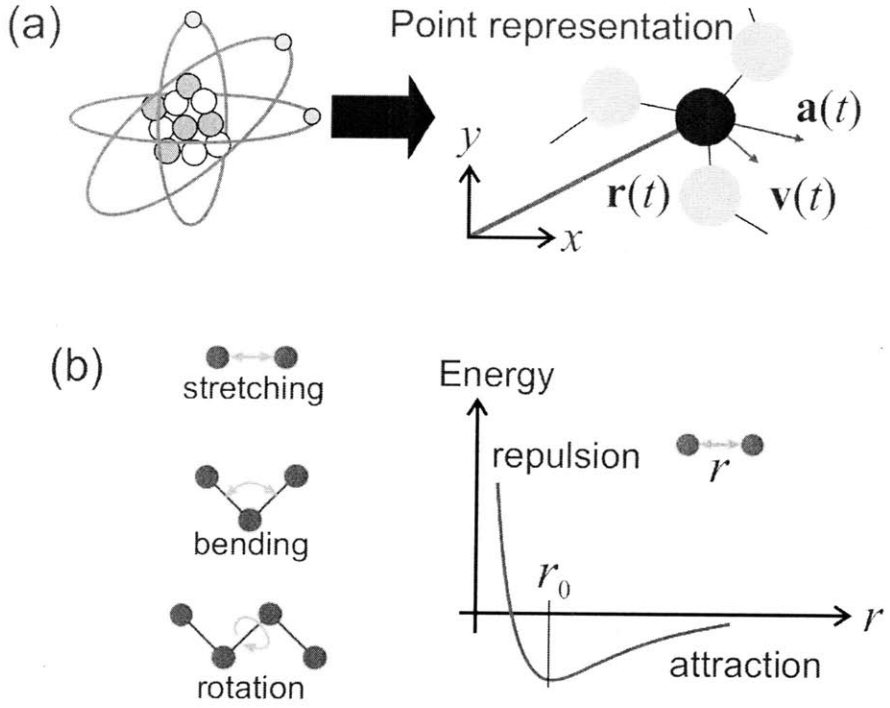

Figure 2-1: Model of the individual energy contributions due to bond stretching, bond bending, bond rotation as well as electrostatic and vdW interactions. The combination of these terms constitutes the entire energy landscape of interatomic and intermolecular interactions. Figure reprinted from Ref. [46].

Classical molecular dynamics generates the trajectories of a large number of particles, interacting with a specific interatomic potential. Thereby, the complex 3D structure of an atom (composed of electrons and a core of neutrons and protons) is approximated by a point particle, as shown in Figure 2-1(b)). The total energy of the system is written as the sum of kinetic energy (K) and potential energy (U),

$$E = K + U \tag{2.1}$$

where the kinetic energy is

$$K = \frac{1}{2} m \sum_{j=1}^{N} v_j^2, \tag{2.2}$$

and the potential energy is a function of the atomic coordinates r_j,

$$U = U(r_j), \tag{2.3}$$

with a properly defined potential energy surface $U(r_j)$. The numerical problem to be solved is a system of coupled second order nonlinear differential equations:

$$m\frac{d^2r_j}{dt^2} = -\nabla_{r_j}U(r_j) \qquad j = 1..N, \tag{2.4}$$

which can only be solved numerically for more than two particles, $N > 2$. Typically, MD is based on updating schemes that yield new positions from the old positions, velocities and the current accelerations of particles. In the commonly used Verlet scheme, this can be mathematically formulated as

$$r_i(t_0 + \Delta t) = -r_i(t_0 - \Delta t) + 2r_i(t_0) + a_i(t_0)\,(\Delta t)^2 + O((\Delta t)^4) \tag{2.5}$$

The forces and accelerations are related by $a_i = f_i/m$. The forces are obtained from the potential energy surface – sometimes also called force field – as

$$F = m\frac{d^2r_j}{dt^2} = -\nabla_{r_j}U(r_j) \qquad j = 1..N. \tag{2.6}$$

Molecular dynamics simulations can be used as a tool for discovering mechanisms or reaction pathways in a small group of atoms, where the simulated system is the actual designed experimental sample. Thus it can be used for small molecule reactions, and nano-sized systems such as carbon nanotubes, proteins, nanofluids etc. However, it is also extensively used to create a sample picture of much larger systems in length scale. The idea then is to use molecular dynamics as a tool for statistical mechanics for studying systems under equilibrium or evolving boundary conditions. In either case, the actual system, may be under certain thermodynamic conditions e.g. a certain temperature or pressure or energy constraint. These thermodynamic boundary conditions need to be applied to the MD simulation. Time-averaged thermodynamic variables can then be estimated over the length of the MD run. The ergodic hypothesis then postulates that the time averaged statistical quantities for a system approach the ensemble average over all possible states of the system at very large times.

The primarily used thermodynamics conditions, or statistical ensembles in MD

are the micro-canonical (also called NVE -conserved number of atoms, volume and energy), the canonical (also called NVT- conserved number of atoms, volume and temperature) and the isobaric-isothermal (also called NPT - conserved number of atoms, pressure and temperature). Next we provide a brief overview of how these ensembles are implemented in various molecular dynamics codes.

2.1.1.1 NVE ensemble

In the NVE ensemble, the group of atoms is isolated from any changes in number of atoms (N), system volume (V), and total system energy (E). The system evolution is by the same equations provided in (2.5). It is critical to ensure energy conservation in the numerical approximation of these equations, which require a judicious choice of the timestep of integration in (2.5).

2.1.1.2 NVT ensemble

In the NVT ensemble, the number of atoms (N), system volume (V) and system temperature (T) are conserved. The system is thus allowed to exchange energy with a virtual heat bath, to maintain constant temperature. The implementation is through the interactions of the atoms in the system with a thermostat. A simple and common implementation is the Berendsen thermostat [47], which scales the velocities of the atoms every few steps in the simulation so that the temperature approaches the desired value, thus mimicking a heat bath. This is realized by calculating a rescaling parameter λ,

$$\lambda = \sqrt{1 + \frac{\Delta t}{\tau}(\frac{T}{T_{set}} - 1)}, \tag{2.7}$$

where Δt is the MD time step and τ is a parameter that describes the strength of the coupling of the system to the virtual heat bath. The velocities are then rescaled by,

$$\mathbf{v}_{new,i} = \lambda \mathbf{v}_i, \tag{2.8}$$

for each atom i. Other approaches to enforce the NVT ensemble include the Nose-Hoover scheme [48] and methods based on Langevin dynamics [49].

2.1.1.3 NPT ensemble

In the NPT ensemble, the number of atoms (N), system pressure (P) and system temperature (T) are conserved. In addition to a thermostat, a barostat is needed, and the system volume is adjusted for the system pressure to converge to an applied pressure tensor. Here the popular schemes are the Nose-Hoover [50], and Parrinello-Rahman [51].

The availability of interatomic potentials for a specific material is often a limiting factor for the applicability of the MD method, since, the complete material behavior is determined by this choice. Designing appropriate models for interatomic interactions provides a rather challenging and crucial step that remains the subject of very active discussions in the scientific community. A variety of different interatomic potentials are used in the studies of metals, inorganic materials and biological materials, with various degrees of accuracy and speed, and the choice of potential depends heavily on the application area, and not just a stand-alone description of the material behavior. Designing or choosing a potential that is accurate enough to capture all possible phenomena expected in the application under study, and not too complex that it slows down computation time and size scale considerably is an art in this field.

The goal of the next section, 2.1.2, is to provide a brief overview of popular interatomic force fields and modeling approaches suitable for simulating the behavior of metals and brittle inorganic materials, which are the focus of study here. For additional information, the reader may refer to extensive review articles, in particular regarding force field models [52, 53].

2.1.2 Force fields

All-atom force fields are used in molecular dynamics simulations of metals and inorganic materials at the nanoscale. Some classes of force-fields can be tuned and made

applicable to a wide range of materials whereas others exist for only specific elements and compounds. For the sake of brevity, we will only cover the atomistic force-fields used in this work, *i.e.*, the two-body Lennard-Jones (LJ) and Morse potentials, and, the multi-body Embedded Atom Method (EAM) and Reactive Force Field (ReaxFF) potentials.

2.1.2.1 Two-body potentials—LJ, Morse and harmonic

The simplest atom-atom interactions are ones in which the potential energy only depends on the distance between two particles. The total energy is then given by,

$$U_{total} = \frac{1}{2} \sum_{i \neq j=1}^{N} \sum_{j=1}^{N} \phi(r_{ij}), \tag{2.9}$$

where $\phi(r_{ij})$ is the distance between particles i and j. Two-body (pair) potentials must capture attraction at far distance leading to creation of a bond, and repulsion at very close distances arising from the quantum-mechanical Pauli exclusion principle.

The Lennard-Jones pair potential can be used to model realistically the behavior of noble gases (e.g. argon, neon). The form of the energy functional is:

$$\phi(r_{ij}) = 4\epsilon_0 \left[\left(\frac{\sigma}{r_{ij}} \right)^{12} - \left(\frac{\sigma}{r_{ij}} \right)^{6} \right], \tag{2.10}$$

where ϵ_0 is a measure of the energy minimum of the pair potential, and σ is a measure of the equilibrium distance between two atoms, where the force is zero. A crystal made up of LJ interactions allows for the formation and existence of defects, dislocations and vacancies. Though very rudimentary, the LJ potential can also be used as the simplest model for metals in some situations, and can be fitted to the elastic constants and lattice spacing of a metal crystal. However, the model has shortcomings with respect to stacking fault energies and anisotropic elasticity of metals. Other simple models for metals are the Morse potential and the harmonic potential.

The Morse energy functional is defined as,

$$\phi(r_{ij}) = D\left[1 - exp\left(-\beta\left(r_{ij} - r_0\right)\right)\right]^2, \tag{2.11}$$

where r_0 stands for the nearest neighbor lattice spacing and D and β are additional fitting parameters. A fit of this potential for different metals, can be found, for instance in [54]. The Morse potential allows greater freedom in fitting to experimental properties than the LJ because of the higher number of parameters.

In some cases, it is advantageous to linearize potentials around their equilibrium position; this leads to the harmonic bond potential:

$$\phi(r_{ij}) = a_0 + \frac{1}{2}k\left(r_{ij} - r_0\right)^2, \tag{2.12}$$

where k is a spring constant, r_0 is the equilibrium spacing between atoms, and a_0 is a constant parameter. The harmonic bond potential can be augmented with harmonic 3-body angle and 4-body dihedral potentials. The major strength of harmonic potentials is their computational simplicity, and thus, the ability to model systems of large sizes of micron length scale.

The LJ, Morse and harmonic potentials are also used for testing 'model' materials, *i.e.*, to obtain general qualitative and order of magnitude insight into behavior of different classes of materials. The low number of parameters and their relative magnitude can be varied easily to study the impact of atomistic parameters on large-scale materials behavior.

2.1.2.2 EAM potential

One of the most widely used force-fields for metals is the Embedded Atom Method (EAM) and its modifications [55, 53, 56, 57]. The EAM is a multi-body force-field that takes into account not only interactions between pairs of atoms, but also atoms with their entire surrounding neighborhood.

An EAM potential for metals is typically given in the form,

$$\begin{aligned} E_{\text{tot}} &= \textstyle\sum_i F_i\left(\rho_{h,i}\right) + \frac{1}{2}\sum_i \sum_{j(\neq i)} \phi_{ij}\left(R_{ij}\right) \ , \\ \rho_{h.i} &= \textstyle\sum_{j(\neq i)} \rho_j^a\left(R_{ij}\right) \ . \end{aligned} \tag{2.13}$$

where E_{tot} is the total energy of the system, $\rho_{h,i}$ is the density contribution at

atom i due to remaining atoms of the system, $F_i(\rho)$ is the energy to embed atom i in the density ρ, $\phi_{ij}(R)$ is the pair-pair interaction between atoms separated by a distance R. The electron density depends on the local environment of the atom i, and is captured here by the distribution of other metal atoms around the atom i within a cutoff distance. It is usually captured by a two-body density measure that describes how the electron density changes as a function of the distance between two atoms. The embedding function F describes how the energy of the atom depends on the local electron density. Several different analytical forms are used to represent these two functions for different metals. The other half of the potential is the two-body term ϕ that captures the basic attraction or repulsion of two atoms.

EAM potentials allow a much better representation of the anisotropy of elastic properties and dislocation properties than two-body pair potentials. They have been used successfully in modeling several FCC metals such as silver, gold, copper, nickel, platinum and their alloys [53, 58]. They have been widely used to unlock mechanisms and predict properties in nanoscale metals size regime, e.g. in predicting strengths and phase transformations in metal nanowires, and crystal size-strength relations in nanocrystalline metals. They are, however, incapable of modeling effects of directional bonding, which is important in metals with some covalent character. To address directional bonding in metals, modified EAM methods (MEAM) have been proposed for materials such as aluminum, iron and several others [59, 60].

2.1.2.3 Reactive force field — ReaxFF

Reactive force fields [61, 62, 63] represent a strategy to overcome some of the limits of classical force fields, in particular their inability to model chemical reactions. Capturing the response of chemical bonds far from equilibrium turns out to be very important for modeling mechanical response in some materials.

Reactive potentials start off with a bond-length to bond-order relationship. This is used to obtain smooth transitions between different bond types, including single, double and triple bonds. All connectivity-dependent interactions such as valence and torsion angles are formulated to be bond-order dependent. Energy contributions

disappear smoothly upon bond dissociation, so that no energy or force discontinuities appear during reactions. They also feature shielded nonbonded interactions such as Van der Waals and Coulomb interactions, without discrete cutoff distances to ensure smoothness. The method uses a geometry-dependent charge equilibration scheme (QEq) [64] that accounts for polarization effects and redistribution of partial atomic charges as a cluster of atoms changes its shape.

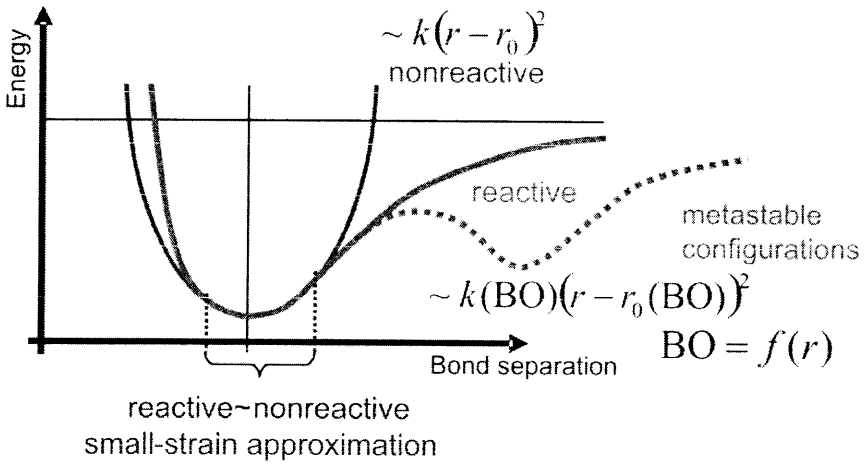

Figure 2-2: Concept of developing reactive potentials [42]. In a nonreactive potential, the potential expression does not change during deformation of the molecule. The reactive potential is based on the idea that the potential parameters, e.g. the tangent spring constant k, depends on the local atomic environment. In this example, the bond order (BO) modulates both the tangent spring constant and the equilibrium distance r_0. This approach enables one to express a continuous energy landscape with several metastable states. The bond order can be directly related to the bond distance between atoms.

A characteristic feature of the ReaxFF force fields is that all parameters of the force field are derived from fitting against quantum mechanical (QM) data (density functional theory (DFT) calculations). This process is referred to as *force field training* and the group of QM experiments is called the *training set*. The basic concept is to obtain a close-as-possible fit to properties of several reactions and deformations of groups of atoms from DFT calculations and ReaxFF results. Typically these properties include elastic properties and equations of state, surface energies, dissociation energies, and energy landscapes. The absence of any empirical fitting to experimental data makes this a completely QM-based force field.

Several flavors of the ReaxFF potential have been developed. The reactive potentials, originally only developed for hydrocarbons, have been extended recently to cover a wide range of materials, including metals, semiconductors and organic chemistry in biological systems such as proteins [65, 66, 61, 63, 67]. Among other applications, they have been used successfully to reproduce properties of several carbon nano-systems such as nanotubes, buckyballs and graphene. They have also been used successfully in reproducing silicon oxidation and fracture in silicon and silica [68, 69, 70, 71].

However, due to the increased complexity of the force field expressions and the cost of the charge equilibration steps, the ReaxFF simulations are usually between 50 to 100 times more expensive than non-reactive force fields, in terms of computational power. Still they are several orders of magnitude faster, and can model systems much larger than DFT calculations, which can also be used to model bond rupture.

2.1.3 Scaling and computational issues

All-atom simulations are an expensive proposition as far as computational resources and time are concerned. Large number of atoms, and complexities of force-field expressions often lead to the requirement for parallel computing techniques and the use of supercomputers with several computing nodes. The state-of-the-art in terms of system size modeled have been several-billion atom simulations [72, 73], e.g. shock loading response of crystals [74] and reactions in energetic materials [75]. Most of these calculations have been carried out on parallelized codes on supercomputers with $> 1,000$ computing nodes. The increase in computational speed, (now $\approx 10^{15}$ floating point operations per second (PFLOPS)), over the last few decades has definitely helped in the success of molecular dynamics as a widely used tool. However, this size is still a minuscule part of a macroscopic sample with approximately 10^{23} atoms (corresponding to 1 mole). This size is clearly not achievable today, and even if possible, would provide huge challenges for data handling, storage, analysis and visualization. However, for many material properties it is not necessary to consider 10^{23} atoms. Many thermodynamic and mechanical properties can be captured in systems of thousands of atoms or much less.

Another scaling issue of molecular dynamics is of time-scaling. The unit computational step in time is of the order of a femtosecond in most MD simulations, to ensure system energy conservation and the capture individual atomic vibration events. This implies a MD simulation run over a few days will capture a system evolution over a few nanoseconds only. However, in many applications, such femtosecond accuracy is not helpful, as significant changes in the system are rare events, and a lot of computational time is wasted following atomic vibrations. This also requires the use of artifices to speed up rare event encounters, by imposing unrealistically high loading rates on the system.

Some of these problems can be overcome by methods for modeling across length and time scales, called multiscale modeling. The core philosophy here is to use combinations of quantum, atomistic or continuum methods to tackle problems of large scale, while keeping computational costs tractable. An excellent example is the problem of chemical complexity (e.g. reactions at a crack tip) in the deformation of a material. The reaction may be highly localized to the crack tip region, requiring quantum or reactive force field usage in that region, but the effect on stress fields will be large length scale, requiring the entire system to consist of thousands of atoms or more.

2.2 Multiscale modeling

The properties of materials are often determined by highly localized phenomena that influence the material at wider spatial and temporal scales. Materials whose properties are affected by such localized processes occurring at specific spatial and temporal scales can be handled efficiently with multiscale methods, based on the idea of decomposing the computational domain to reflect requirements for spatial variations of computational accuracy, depending on specific mechanisms that occur.

The deformation and fracture mechanics of materials is one such area where processes occur over a wide range of length scales, while processes can be highly localized at defects such as grain boundaries or crack tips. Chemistry and mechanics are typically considered independently for material deformation studies in large-scale

simulations using non-reactive force fields. However, the details of bond breaking and formation have been shown to have significant influence on the macroscopic fracture mechanics of materials, and can not be neglected in order to obtain predictive models of the material behavior under extreme conditions and harsh environments.

Multiscale methods for deformation and stress analysis in materials can be broadly categorized into two types, depending on information passing between different length scales: hierarchical and concurrent [76]. Hierarchical schemes include MD methods whose underlying potentials are derived from *ab-initio* quantum calculations e.g. ReaxFF [61, 62], and many EAM [60] potentials. Some of these methods use phenomenological parameters derived from smaller length scale behavior, used to characterize the coarser length scale. The primary challenge for these methods is the need for complete knowledge of all relevant mechanisms and processes at the lower scale. Moreover, the lowest length scale method in these schemes has to have no or minimal empirical character like Density Functional Theory (DFT) [77, 78, 79] or quantum chemistry [80] methods.

Concurrent schemes link methods across length scales simultaneously. They communicate through *handshaking* approaches - often featuring regions where two distinct methods are used to implement the transition from one method to another. There are many systems and processes where concurrent modeling across scales is useful in analysis, for example, in interface-controlled materials phenomena like grain boundary diffusion, crack propagation, material embrittlement or thin film adhesion. A major challenge is to obtain smooth coupling of the disparate simulation methods, with no ghost forces or barriers at the method interfaces, to provide a smooth energy landscape. Several concurrent multiscale schemes have been developed, among them the MAAD method (microscopic, atomistic and *ab-initio* dynamics) [81, 82] for studying fracture in silicon, the quasi-continuum method [83, 84] for coupling atomistic and finite-elements, and the CADD method (coupled atomistic and discrete dislocation method) [85]. A recent scheme developed is a hybrid ReaxFF-EAM coupling, developed within the Computational Materials Design Framework [86, 87], a set of computational tools that allows for easy integration of simulation methods

across various length scales.

2.3 Link to continuum state variables

It is often useful to be able to derive continuum thermodynamic and mechanical state variables from atomistic simulations. Temperature and pressure of a system can be easily measured as statistical quantities over a certain time length of a simulation [52]. Below are outlined how stress and strain are measured from atomistic simulations.

2.3.1 Stress

The challenge in defining an atomistic stress tensor is relating it to a continuum stress valid at every point in space is the discreteness of an atomistic materials simulation.

The virial stress is defined as,

$$\sigma_{ij} = \frac{1}{V}\left(-\sum_{\alpha} m_\alpha v_{\alpha,i} v_{\alpha,j} + \frac{1}{2}\sum_{\alpha,\beta,\alpha\neq\beta}\left(r_{\alpha\beta,i} f_{\alpha\beta,j}\right)\right), \tag{2.14}$$

where $v_{\alpha,i}$ is the velocity of atom α in the direction i, m_α is its mass, $r_{\alpha\beta,i}$ is the distance vector from atom α to atom β in the direction i and $f_{\alpha\beta,j}$ is the force exerted on atom α by atom β in the direction j.

The first term on the right is the kinetic contribution, and the second the contribution from forces between the atoms. The virial stress needs to be averaged over space and time to converge to the Cauchy stress tensor of continuum mechanics [88, 89].

2.3.2 Strain

Local atomistic atomic strains can be defined in terms of the affine transformations that transform the neighborhood of an atom from the unstrained configuration to the strained state.

To fit a transformation in a least squares sense, we seek the transformation matrix $\mathbf{J}_\alpha$ at atom α that minimizes $\sum_{\beta\in N_\alpha}\left|\mathbf{J}_\alpha \mathbf{r}^0_{\alpha\beta} - \mathbf{r}_{\alpha\beta}\right|^2$ where β runs over all the neighbors of atom α and $\mathbf{r}^0_{\alpha\beta}$ is the undeformed distance vector from atoms α to β and $\mathbf{r}_{\alpha\beta}$ is

the deformed distance vector (both written in column form here). The solution of this least squares minimization is,

$$\mathbf{J}_\alpha = \mathbf{V}_{alpha}^{-1}\mathbf{W}_{alpha}, \text{where} \mathbf{V}_\alpha = \sum_{\beta \in N_\alpha} \mathbf{r}^0_{\alpha\beta}\mathbf{r}^{0T}_{\alpha\beta}, \mathbf{W}_i = \sum_{\beta \in N_i} \mathbf{r}^0_{ij}\mathbf{r}^T_{ij}, \tag{2.15}$$

where the superscript T denotes the transpose of the matrix. The Lagrangian strain matrix can then be calculated as

$$\eta_\alpha = \frac{1}{2}\left(\mathbf{J}_\alpha^T\mathbf{J}_\alpha - \mathbf{I}\right), \tag{2.16}$$

where $\mathbf{I}$ is the identity matrix [90].

2.4 Visualization and data analysis

Molecular dynamics simulations produce large quantities of data, sometimes running into several terabytes. This is because they usually save snapshots of the system state as the simulation proceeds, storing atom positions, velocities, energies, forces, stresses, and system temperatures and pressures. It is necessary to have scripts and programs that can post-process such huge data sets to filter out useful information and display it in a user-friendly fashion. For example, a billion-atom simulation of a single crystal under shock loading can provide a very useful visualization if only the resulting defects in the crystal are visualized and not the entire system.

For the analysis of atomistic simulations for mechanical properties, measures like strain, stress or potential energy of atoms are important quantities that provide insight with respect to continuum mechanics theories. However, it is often also useful to post-process the data and derive new quantities providing information about defect structures within condensed-matter systems.

Next we discuss a few examples for the analysis of crystal defects in metals and inorganic crystals that will be useful in the later chapters.

2.4.1 Energy method

An easy way to 'see' in the interior of solids and find defects is to use the energy method. Here only atoms with potential energy greater than a critical energy ϕ_{cr} above the bulk energy ϕ_b are visualized. This method is very effective for plotting dislocations, microcracks, surfaces, grain boundaries, voids and other sites of high energy. The method, however faces difficulties in visualization for defects with very low energies of formation, or systems at high temperatures, when the thermal energies of ordered bulk atoms become comparable to certain defect energies. It is very useful in crack propagation simulations, as it can quickly identify the position of a crack tip and formation of new microcracks/ defects in the vicinity of an existing crack.

2.4.2 Slip vector analysis

The slip vector analysis [91] provides visualization of slip planes, dislocation cores and stacking faults in crystalline materials. It provides the exact Burgers vector and direction of slip and can also visualize incipient slip (before a dislocation core is completely formed). The slip vector of an atom α is defined as

$$s_i^{\alpha} = -\frac{1}{n_s} \sum_{\alpha \neq \beta}^{n_\alpha} \left\{ x_i^{\alpha\beta} - X_i^{\alpha\beta} \right\}, \tag{2.17}$$

where n_s is the number of slipped atoms, $x_i^{\alpha\beta}$ is the vector difference of positions of atoms α and β at the current configuration, and $X_i^{\alpha\beta}$ is the vector difference of these atomic positions at no mechanical deformation.

The slip vector analysis was originally used in visualizing defect structures formed during the nanoindentation of metals. It has also proved very useful in simulations of ductile fracture.

2.4.3 Centrosymmetry parameter

Centrosymmetry parameter [92] measurement is used for crystalline structures with a center of symmetry. It uses the fact that centrosymmetric crystals remain cen-

trosymmetric after homogeneous deformation. Each atom has pairs of equally oppositely placed neighbors in a centrosymmetric crystal. This rule breaks down when a defect is in the neighborhood of the atom under consideration. The method is particularly useful to distinguish different types of defects, and to display stacking faults (which are hard to observe using the energy method). For example, defining the centrosymmetry parameter in a face-centered cubic (FCC) crystal as,

$$c_i = \sum_{j=1}^{6} \left\{ \left| \sum_{k=1}^{3} r_{k,j} + r_{k,j+6} \right|^2 \right\}, \tag{2.18}$$

where $r_{k,j}$ is the kth component of the bond vector of atom i with its neighbor atom j, and $r_{k,j+6}$ is the same quantity with respect to the opposite neighbor in the FCC crystal. The method can display defects at high temperatures also, where the energy analysis starts to fail due to the thermal fluctuations of the atoms. It has been used successfully in many simulations of FCC metals to display stacking faults and partial and full dislocation cores.

2.4.4 Common neighbor analysis

The common neighbor analysis [93] is also used for crystalline structures, to classify atoms according to their local crystalline structure (FCC, BCC, HCP etc.). This analysis method is based on a nearest-neighbor graph, *i.e.*, a mathematical graph structure consisting of edges that connect nearest neighbor atoms. Which atoms are considered nearest neighbors is determined by a user-defined cutoff distance. Each crystal structure exhibits a characteristic local topology of the nearest-neighbor graph, and each atom is the classified as belonging to a certain local crystal structure. It is again very useful for visualizing stacking faults in FCC crystals as the atoms lying within the fault have a local HCP structure.

A wide variety of scripts in Python, C and FORTRAN have been written in this thesis for analyzing data from MD simulations. A wide range of functions available in MATLAB have also been used in this thesis to use raw data from simulations to extract material properties, displacement profiles and strain distributions. All scripts

used in this thesis are provided in Appendix A with appropriate descriptions within the script.

2.4.5 Visualization programs

Visualization plays a crucial role in the analysis of MD simulation results, as the raw data represents a collection of positions, velocities and accelerations as a function of time [42]. In particular, structural defects and patterns of cooperative atom motion are difficult to analyze. To address this point, many visualization tools have been developed for displaying atoms, molecules and assemblies such as nanostructures and bulk systems. A rather versatile, powerful and widely used visualization tool is the Visual Molecular Dynamics (VMD) program [94]. VMD enables one to render complex molecular geometries using particular coloring schemes. VMD however suffers from a drawback of being unable to process large systems with $> 100,000$ atoms. Atomeye [95] is another visualization program used extensively in this thesis for visualizing large systems. Aimed at crystalline materials, it possesses several tools for the analyses of crystals and crystalline disorder. Very large systems possessing O(10 million atoms/particles) are visualized using OpenDX [96] and Ovito [97]. These visualizations are often the key to understanding complex correlated dynamical processes and mechanisms in analyzing the motion of atoms, and they represent a filter to make useful information visible and accessible for interpretation.

Chapter 3

Strength enhancement through bone-inspired metal-matrix nanocomposite design

Bone, a natural composite material, comprises of particularly 'weak' constituent phases, soft protein matrix and hard hydroxyapatite mineral platelets. These constituents possess very poor mechanical properties to be used as stand-alone structural materials. Hydroxyapatite is as brittle as commercial ceramics, and fractures catastrophically, whereas proteins have the same order of stiffness of soft polymers such as polythene. In fact, the nanostructural makeup of bone has been shown to be of crucial importance for its superior mechanical properties over its constituent phases, providing high strength at high stiffness (see Chapter 1, section 1.3). This raises, as discussed in Chapter 1, interesting questions about the viability of the transfer of similar mechanical property enhancement strategies to engineering materials and structures. In particular, the application to the design of metal-matrix composite materials seems promising due to the availability of corresponding 'soft' and 'hard' metal constituents. The scope and viability of the application of bone nanostructure to functional metal-matrix composites, however, remains unresolved. In this chapter, a novel class of biomimetic nanocomposites inspired by the structural motif found in bone and nacre is proposed, and used to formulate structural composites for mechan-

ical loading applications. We then report a series of computational experiments using molecular dynamics simulation to study the yield response of the metal-matrix composite subject to tensile loading, and study the changes in mechanisms and properties that arise.

3.1 Structure inspiration from nanostructure of bone

Metal-based nanocomposites provide a great potential for applications in high hardness and toughness material design. Potential applications include coatings for friction and wear-resistant cutting tools, shock impact-dissipating structures and other tribological applications where strong functional materials are the key to initiate further technological development [98, 99, 100, 101]. Recent advances in the development of nanocomposite materials have suggested that a new paradigm of composite design might be to systematically engineer the nanostructural arrangement of components by designing their properties, interfaces and geometry to tailor desired macroscopic functional properties. These efforts extend earlier studies of creating nanomaterials out of metallic constituents (e.g. nanowires, thin films) towards bulk materials [102]. However, the optimal choice of nanostructural arrangement of material constituents to maximize performance remains unknown, preventing us from systematically carrying out a bottom-up design approach.

A variety of biological structural materials such as bone and nacre are known to feature a common "brick-and-mortar" structural motifs at the nanoscale, composed of material constituents with disparate properties [103, 33, 46, 23, 7] (Figure 3-1). These universal nanostructures are seen to combine inferior building materials, soft protein and brittle calcite or hydroxyapatite crystals to obtain structures with high strength and high toughness at biological scales [1, 104, 13]. Their improved properties have been attributed to their hierarchical structure, as well as their fundamental structural organization of constituting elements at the nanoscale [36] (see Chapter 1). The biological role of these materials is strongly related to load carrying and armor protection in nature. Based on their intriguing properties, these materials

raise an important question whether their design strategies could provide directions for conventional structural engineering material design. However, for materials development, the use of proteins is not a viable option, because these materials are rather difficult to synthesize and engineer. Here we propose an alternative approach, based on using metal-metal nanocomposites that utilize the material concepts identified from biological analogs as guiding principles in the design process. However, despite earlier studies [36, 105, 106], the transferability of designs found in biological structures towards conventional metal and ceramic based composites remains an unresolved question, partly because the fundamental mechanisms of how structure and properties are related have not yet been explored. Specifically, the wide parameter space associated with different platelet shapes and orientations has not been described in the literature.

Mimicking the universal design motif found in mineralized protein tissues (Figure 3-1) using metals requires a systematic design of a soft metal/hard metal composite structure. To address this issue, here we report a systematic analysis of the deformation mechanisms and yield strength for a broad variation of nanostructural arrangements, by using full atomistic molecular dynamics simulations. This study elucidates the different deformation mechanisms under plasticity and effect of the nanostructure design parameters on their yielding behavior. We identify optimal design solutions by providing specific length-scales and geometries that yield maximum strength at efficient material use.

3.2 Model construction

All simulation studied are performed using fully atomistic simulations, using EAM potentials (see section 2.1.2). All nanocomposite structures under study are constructed out of single crystals of the matrix and platelet phases. Face-centered cubic (FCC) metals are chosen for both phases, due to availability of well-tested atomistic potentials [55, 107]. Structures are designed such that crystal orientations of both matrix and platelets are $X=[\bar{1}10]$ $Y=[111]$ $Z=[11\bar{2}]$ (for geometry see Figure 3-1(b)).

To replicate uniaxial tensile load, load is applied in X direction, allowing system relaxation in the Y and Z directions to zero applied bulk normal stresses in these two directions (Figure 3-1(b)).

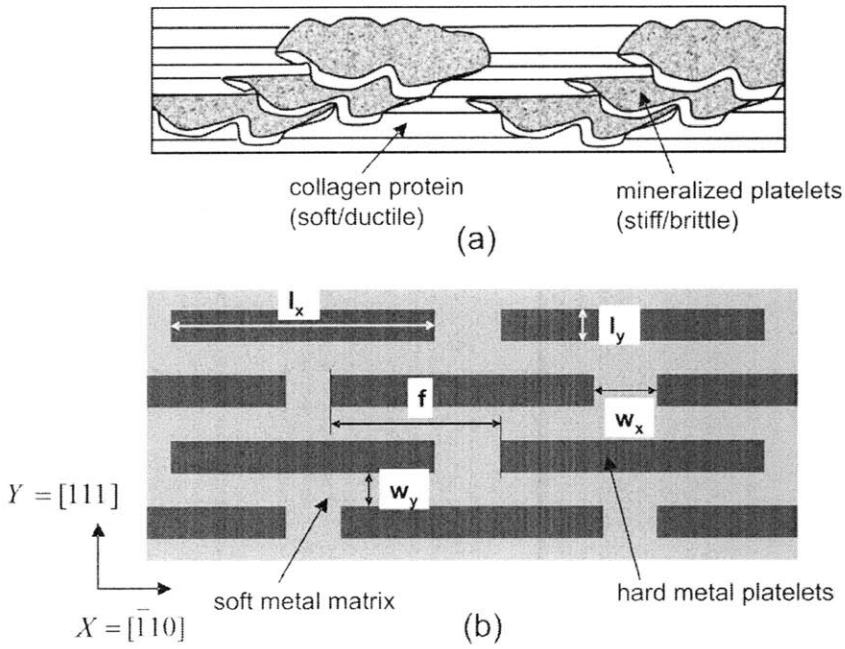

Figure 3-1: Panel (a) The ultrastructure of bone showing hard mineral platelets 2-4 nm thick and up to 100 nm long embedded in a soft collagen-rich matrix (figure adapted and redrawn from reference [33]). Panel (b): A geometrically two-dimensional, simple schematic model of hard/soft phases arranged in a nanocomposite, based on the ultrastructure of bone. This structure is realized with metallic components using a "soft" Cu metal matrix and modified "hard" EAM *model* metal platelets. To create this composite structure, a single copper crystal is arranged in the $[\bar{1}10]$ x $[111]$ (X-Y) orientation, and a regular array of rectangular voids is created. The platelet crystals are inserted in the voids in the same crystallographic orientation, ensuring no overlapping atoms (by avoiding any distance closer than Cu-Cu nearest neighbors). The resulting structures are relaxed to minimize the global normal stresses. The plot also shows the various parameters that determine the geometrical arrangement of such a system. See Eq. 3.2 for the relation between these parameters and the ones used in our study.

To implement a fully atomic-scale study of deformation in these materials, atomistic interaction potentials are required for an accurate description of deformation in the soft matrix phase, the hard platelet phase, and a cross-potential for interactions across the matrix-platelet interfaces. The embedded atom method (EAM) alloy potential [53, 58] is chosen to model the two phases and their interactions. The EAM model has been shown extensively to provide an accurate description of FCC met-

als and their alloys [56]. The use of the EAM alloy potential allows the freedom of modeling of two distinct metals with quite different stiffness and strength properties.

The samples are subject to energy minimization to relax internal stresses, followed by quasi-static tensile loading using molecular statics. System sizes chosen for simulations are approximately 500 Å x 200 Å x 25 Å, with approximately 200,000 atoms in each system. Periodic boundary conditions are applied in all three directions, to mimic large crystal systems. The system size is large enough to allow dislocation interactions across 4 layers of platelets, but not too large to slow down computation. Larger sized samples with periodic boundary conditions show similar flow stress values. Load application is achieved in two steps- system global stress relaxation, followed by application of uniaxial tensile load. Quasistatic loading is achieved using displacement boundary conditions along with an energy minimization scheme implemented using a micro-convergence integrator. Flow stresses are calculated as system averaged virial stresses [52] at large strains, where the system stress fluctuates around constant values. The flow stress calculation is averaged over a strain range from 0.15 to 0.2, over a range where plasticity has initiated, and the stress is about constant. The local stress distribution in the sample is calculated through atomic level virial stresses [89].

3.3 Interatomic potential development and testing

The model developed here is not designed to represent a particular pair of materials. Rather, it is developed to allow the freedom to modify material properties in their absolute values and ratios for matrix, platelets and interfaces, in the spirit of a model material [108]. The concept behind using such an approach is driven by the desire to explore a wide parameter space and to understand the material behavior of a wide range of material properties, without focusing on a single, specific material. This facilitates a computational engineering approach in which we systematically investigate the sensitivities of key design parameters on the overall material behavior to provide generic understanding of the relationship between structure and properties.

We specific avoid focusing on modeling a specific material. The atomistic model in this study is based on earlier EAM potentials developed for two species alloy systems such as Ni-Al, Cu, and Ag alloys [53, 109]. The Baskes-Daw model of an EAM potential for face-centered cubic (FCC) metals is reproduced here from Chapter 2, since, it will be used for the modified potential development (see eq. (3.1) below). It consists of a pair interaction term, and an electron density term which contributes through an embedding energy term that charges an energy penalty for deviating from an FCC environment. The development of an alloy potential requires the development of a cross-pair potential, and density functions for atoms of type A in an environment of type B, and vice versa. The total potential energy is given by,

$$\begin{aligned} E_{\text{tot}} &= \sum_i F_i\left(\rho_{h,i}\right) + \tfrac{1}{2}\sum_i \sum_{j(\neq i)} \phi_{ij}\left(R_{ij}\right) \ , \\ \rho_{h,i} &= \sum_{j(\neq i)} \rho_j^a\left(R_{ij}\right) \ , \end{aligned} \tag{3.1}$$

where E_{tot} is the total energy of the system, $\rho_{h,i}$ is the density contribution at atom i due to remaining atoms of the system, $F_i(\rho)$ is the energy to embed atom i in the density ρ, $\phi_{ij}(R)$ is the pair-pair interaction between atoms separated by a distance R.

The matrix material is chosen as a soft metal, copper, modeled using the Mishin potential [107]. A model material of higher stiffness and higher strength is chosen as the platelet phase. To achieve this, a modified copper EAM potential is used to model elemental second phase material. This provides the freedom to modify stiffness and strength ratios between matrix and platelets. The inter-elemental potential terms consist of the cross-potential pair potential, which has also been chosen as a modified Mishin potential. Use of a modifiable cross-potential allows us to vary the interfacial strength, and effect of the same on flow stress. To design the modified interatomic potentials, we selectively change the pair interaction of the copper EAM potential while keeping the density and embedding energy terms unmodified. Modification of only the pair term allows us to modify the bulk modulus, cohesive energy, and unstable and stable stacking fault energies, while maintaining lattice parameter of the FCC phase constant. We use the modified potentials for describing the platelets

and interface, which yields the potential properties shown in Figure 3-2. The ratio of elastic moduli of the metal phases, are not as dissimilar as for bone constituents, due to limitations of the materials used.

3.3.1 Interatomic potential properties

The cross-species potential parameters are adjusted so that the matrix-platelet interface is always weaker than both the matrix and platelets. In the present study, two different interfacial strength levels are used, referred to as "strong" and "weak" interface, defined in this fashion by the adhesion energy across the (111) interface. The work of adhesion for these two interfaces in the (111) orientation is compared with several example metal/ceramic interfaces from literature in Table 3.1 (where the "strong" interface resembles the surface energies of an Al/TiC structure, and the "weak" interface a Cu/Al_2O_3 structure). The freedom in variation of interfacial strength allows mechanisms of matrix-platelet decohesion and interfacial sliding to be activated and become dominant deformation mechanisms at different stress levels. The strength and stiffness of the matrix, platelets, and interfaces are summarized in Figure 3-2a. The stiffness of the platelet material is approximately two times that of the matrix material. This is close to actual stiffness ratios of soft and stiff metals such as Cu/Fe and Cu/Pt. The generalized stacking fault curves [110] have also been calculated for the matrix, platelets and interfaces, and are shown in Figure 3-2b. The large unstable stacking fault energy [111] for the platelet material shows the difficulty of nucleating dislocations in this material, thus making it a "strong", less ductile material.

Interface type	W_{adhesion} **(in J/m^2)**
Strong interface	2.42
Weak interface	1.12
Al/TiC	2.63
Cu/Al_2O_3	1.09-1.30

Table 3.1: Work of adhesion across a "strong" and "weak" interface and comparison to actual metal-ceramic interfaces.

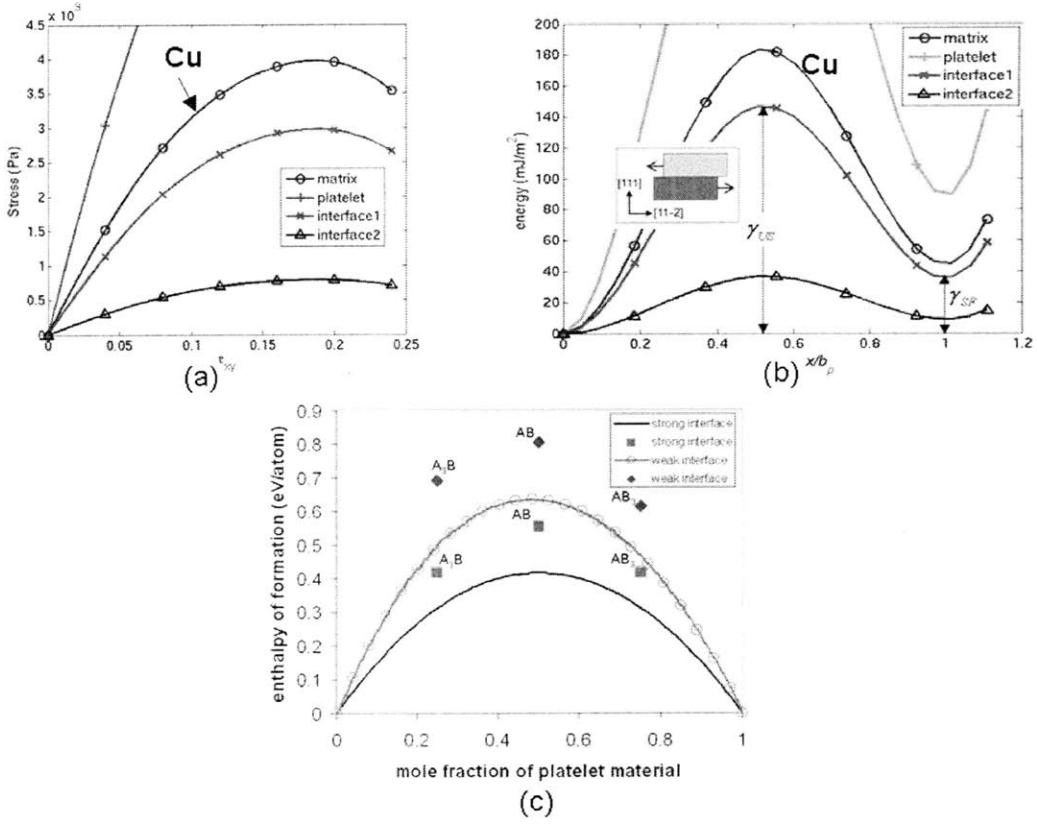

Figure 3-2: Properties of the interatomic potentials, for the various cases considered here. Panel (a) shows the theoretical shear strength against (111) plane shearing in the $[11\bar{2}]$ direction, for matrix (Mishin Cu potential), platelet, "strong" interface (interface1) and "weak" interface (interface2) EAM potentials, showing matrix:platelet stiffness ratio of 1:2. Panel (b) depicts generalized stacking fault curves for the same, showing high dislocation nucleation barrier in platelet phase. Panel (c) shows enthalpies of formation of intermetallics and heats of mixing of disordered alloys between matrix (A) and platelet (B) materials at both "strong" and "weak" interfaces, showing very high positive values leading to low solubility of one material in another [106].

The thermodynamic stability of atomically sharp interfaces between matrix and platelets as they appear in these models is also investigated. The heat of formation has been calculated for alloys of matrix and platelets materials with both types of interfaces over the entire composition range. The heat of formation of possible intermetallic structures AB_3 and A_3B (where A is matrix and B is platelet material) are calculated assuming a $L1_0$ structure, and for AB assuming a $L1_2$ structure (Figure 3-2c) [57, 112]. The heats of formation of the disordered alloys over the entire composition range are calculated from these values using the cluster expansion method (Figure 3-2c) [113]. The large positive heats of formation for the intermetallics show no possibility of them forming at the interfaces. The positive and large heats of formation of the disordered alloys also hint at very low solubility of one element in another and vice versa. Thus overall the implicit assumption of stable interfaces between matrix and embedded platelets is justified.

3.3.2 Design Parameters

The quasi-two dimensional geometrical arrangement of platelets is characterized uniquely in terms of five independent geometric parameters (shown in Figure 3-1b). These parameters are assuming rectangle shaped platelets arranged on a regular two-dimensional motif. Irregular shaped platelets can also be considered in terms of average platelet sizes and distances, to be specified by the five independent parameters. The relation between different parameters is given below:

$$\begin{aligned} V_f &= \frac{l_x\, l_y}{(l_x+w_x)(l_y+w_y)}, \\ \lambda &= l_x/l_y, \\ A_p &= l_x\, l_y, \end{aligned} \tag{3.2}$$

where V_f, l_x, l_y, w_x, w_y, λ and A_p are volume fraction, length and width of platelets, axial and transverse spacing of platelets, aspect ratio, and area of a single platelet. The axial and transverse spacing between platelets are defined as spacing parallel and perpendicular to the loading direction X respectively. The independent parameters

chosen here are V_f, λ, w_x, w_y and f, where f is defined as the stagger between platelets across successive rows as a fraction of the axial repeat distance.

The choice of these parameters helps us to answer questions as: are elongated platelets needed and why? How far apart should the platelets be spaced? What is the effect of volume fraction of platelet phase on flow stress? Changes in other parameters can be studied as a combination of changes of any of these five. First order effects of each of these parameters are studied by varying one particular parameter while keeping the other four constant.

3.4 Atomistic simulations under tensile deformation

3.4.1 Effect of geometric parameters

Studies of effect on flow stress of varying all geometric parameters are presented in the subsequent sections.

3.4.1.1 Effect of platelet volume fraction V_f

First the platelet volume fraction is varied from ≈10% to ≈45%, and effect on flow stress is measured. Keeping the aspect ratio and spacing between platelets constant, the increase in volume fraction is achieved by increasing absolute size of the platelets. There is a slight decrease in flow stress as volume fraction is increased, but the effect is not very strong. The results are shown in Figure 3-3.

3.4.1.2 Effect of platelet offset f

Platelet rows parallel to the axial direction have a pronounced offset from one row to the next in structures such as nacre and bone (see Figure 3-1a). To explore the significance of this offset, a systematic analysis using the present model system is carried out. The offset in the present experiments is measured as a fraction of the

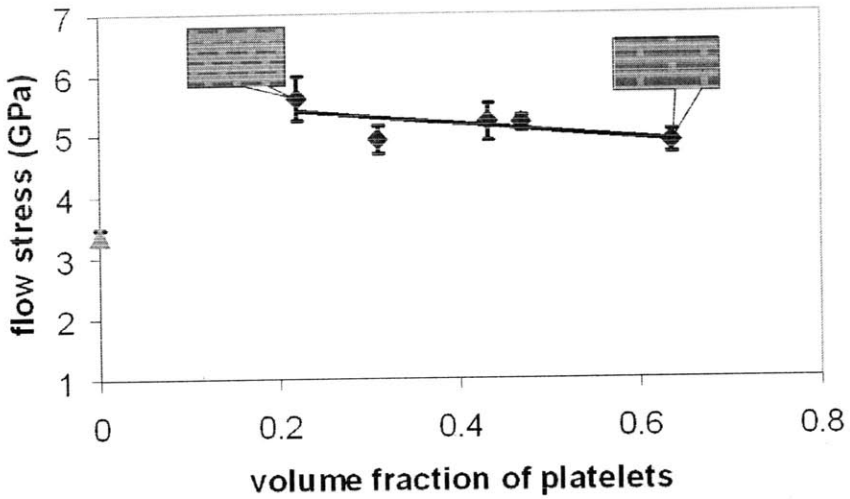

Figure 3-3: Effect of volume fraction on flow stress. Volume fraction is varied from ≈10% to 45% and a slight dependence of flow stress is seen within this range. Black line depicts best linear fit to data. Insets show nanostructure at different volume fractions. The flow stress of the pure copper matrix is shown for comparison (triangular marker on the left; with 1,800 parts per million platelet material, to induce heterogeneous dislocation nucleation).

repeat unit length in the axial direction, and thus, can vary from 0 to 1. The flow stress is measured as a function of this offset and results are shown in Figure 3-4a.

A significant change of ≈10 times is identified in the flow stress, with a saturation observed at a platelet offset of ≈0.25. The load distribution within the structure is studied through the local shear stress distribution σ_{xy} in the regime of elastic deformation (just prior to plasticity), as depicted in Figure 3-4b. Significant effects of the details of shear stress distribution as a function of nanostructured geometry is observed, with large homogeneous domains of shear stress transfer found at platelet offsets beyond 0.25. Gao's shear-tension load sharing model [33] is seen to be applicable to this case, since at offsets of ≈0.25 to ≈0.75 there is sufficient overlap between platelets in subsequent rows to induce predominant shear loading of the matrix material situated between platelet rows. This optimal platelet overlap leads to an effective distribution of load that plays to the respective strengths of platelet and matrix material. Specifically, platelets are subjected to tensile load with very small shear loading, and the ductile matrix material is under shear loading with very small tensile loading. These results show a critical platelet offset beyond which the

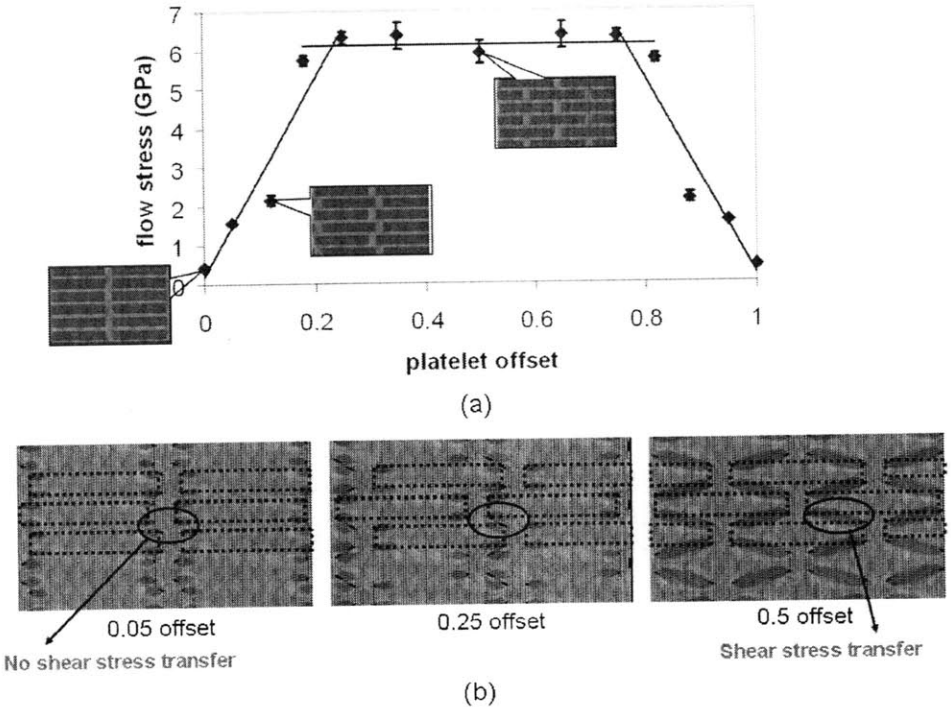

Figure 3-4: Effect of platelet offset on flow stress, (a) shows large effect of variation of offset on flow stress, and a saturation of value at ≈ 0.25 offset; insets show the nanostructure at different offset amounts (b) shows the X-Y plane local shear stress distribution in the nanostructure, with dashed-line bars indicating the location of platelet. The results show that effective load transfer between platelets through shear of matrix material occurs at offsets larger than ≈ 0.25 (note the symmetry of the problem).

shear-tension model provides an accurate model.

3.4.1.3 Effect of aspect ratio λ

The aspect ratio of second phase particles plays an important role in load transfer and anisotropic properties in composites. The discontinuous reinforcement material shape can vary from a needle geometry (oriented in the direction of loading) to a flat disk shape in the other extreme. Platelets in nacre and bone are typically observed to be of flat disk shape with large aspect ratios in length/thickness to width.

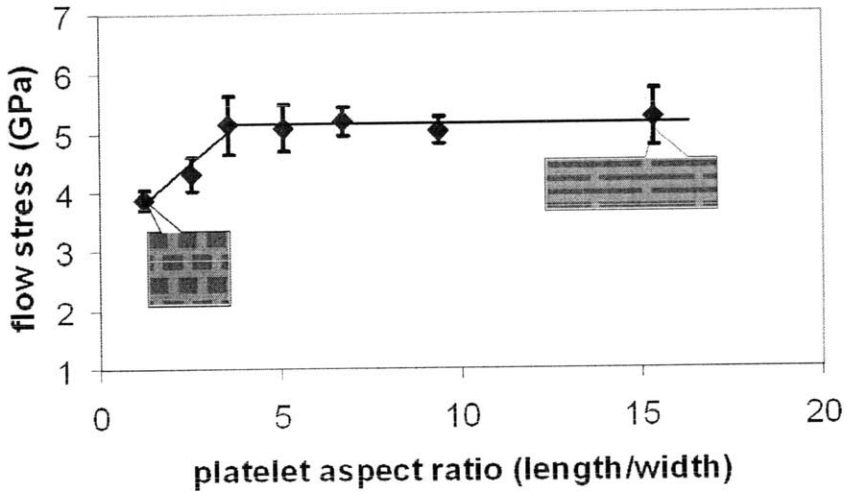

Figure 3-5: Effect of platelet aspect ratio on flow stress. The results reveal that large aspect ratio platelets provide a better mechanical performance, as the flow stress saturates at a maximum value. Insets show the nanostructure at different aspect ratio values.

In the two-dimensional geometric nanostructure, we measure the aspect ratio as the relation of length of platelets in the axial direction to the length in the transverse direction. The aspect ratio is varied from $\approx$1 (square platelets) to $\approx$20 (highly elongated platelets). The results of the effect of aspect ratio on flow stress, while keeping other four parameters fixed, are shown in Figure 3-5. For small aspect ratios, the change of platelet ratios results in an increase of the yield strength. A critical aspect ratio is observed beyond which the flow stress is almost constant, occurring at an aspect ratio of $\approx$4. An analysis of the tensile stress distribution (results not shown) reveal a significant change in load redistribution as the aspect ratio is increased, which suggests that elongated platelets are to be preferred for maximal tensile load to be

carried by the platelets.

3.4.1.4 Effect of axial platelet spacing w_x

As the next step we vary the spacing between platelets in the same row, while keeping the volume fraction, platelet offset, aspect ratio and transverse platelet spacing constant. The analysis of the flow stress as a function of spacing shows a relatively weak dependency. However, despite the limited effect on the flow stress, a change in deformation mechanism is identified. At small spacing, we observe platelet-matrix decohesion, and partial dislocation emission from interfacial cracks (Figure 3-6). At larger spacing, no decohesion is found, and dislocations are emitted from regions of stress concentration, such as the corners of platelets.

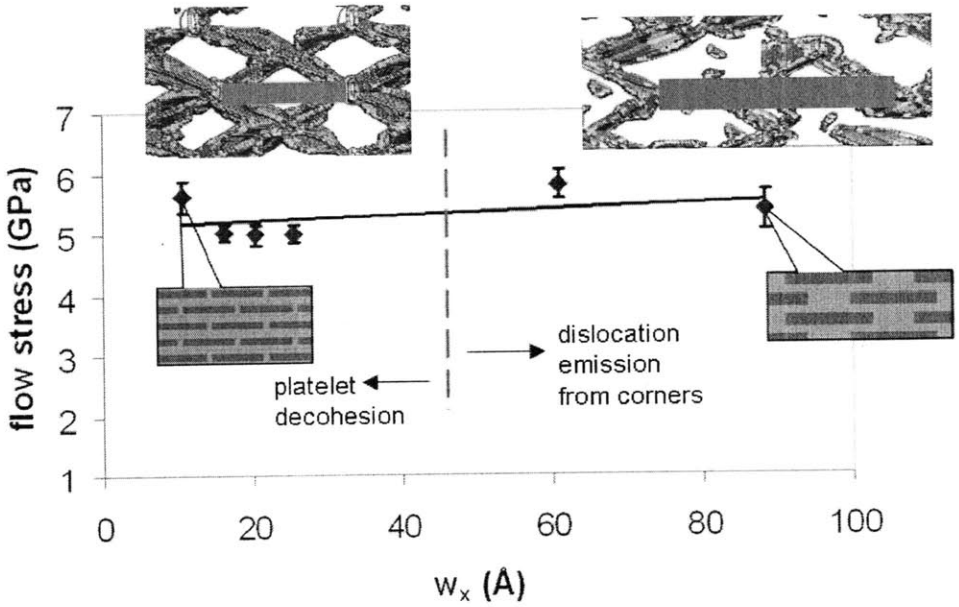

Figure 3-6: Effect of axial platelet spacing w_x on the flow stress. Axial spacing is the distance between platelets along the loading axis. Minimal effect on flow stress value is seen, though, change in mechanism is observed as the spacing is increased. The upper insets shows centrosymmetry plots of slipped regions during initial plasticity with colored bars indicating location of platelets, and the lower insets show corresponding nanostructure. At lower spacing, platelet-matrix decohesion occurs, shown by the red circles, followed by dislocation emission from the cracks. At higher spacing, dislocation emission is seen from areas of stress concentration such as platelet corners.

3.4.1.5 Effect of transverse platelet spacing w_y

The spacing transverse to the direction of loading is varied in the next step, while keeping the other four parameters fixed. These analyses show a gradual decrease in the flow stress as the transverse spacing is increased. A plot of the parameter $\sqrt{w_y}$ versus flow stress shows a linear trend, suggesting Hall-Petch like behavior where the flow stress increases by ≈50% [114, 115] (Figure 3-7). The analysis reveals that the effective length-scale parameter for the Hall-Petch like behavior is the transverse spacing, w_y. This is probably due to dislocation motion barrier established at the matrix-platelet interface, which effectively acts as a grain boundary-like structure.

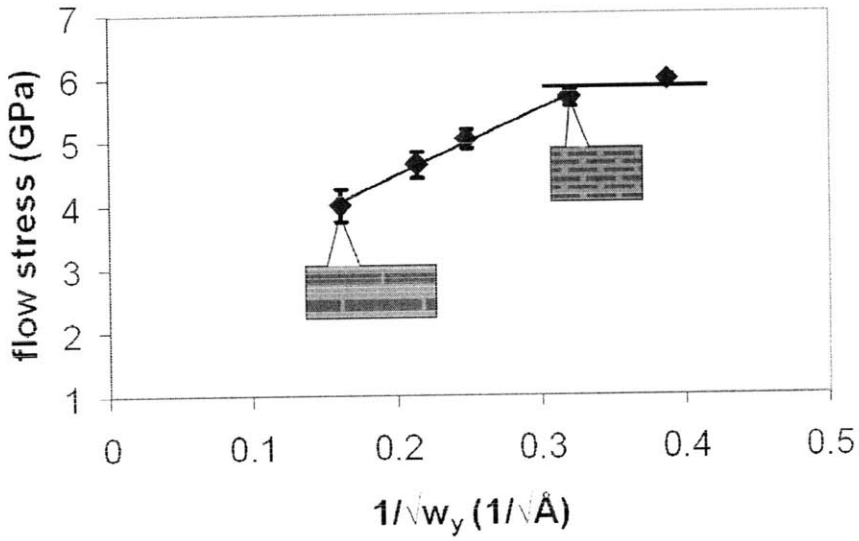

Figure 3-7: Effect of transverse spacing w_y between platelets on flow stress. The plot shows the flow stress as a function of $1/\sqrt{w_y}$, revealing a Hall-Petch like behavior up to the strength limit (insets show nanostructure at different spacings).

3.4.1.6 Effect of interfacial strength

The effect of matrix-platelet interfacial strength on deformation mechanisms and flow stress is studied by performing a self-similar size scale analysis for both the "weak" and "strong" interfaces (see Table 3.1). The non-dimensional parameters, that is, platelet offset, aspect ratio and volume fraction are kept constant, while the size of the platelets A_p is scaled up. Figure 3-8 shows how the flow stress varies with $1/\sqrt{w_y}$ for both the interface types.

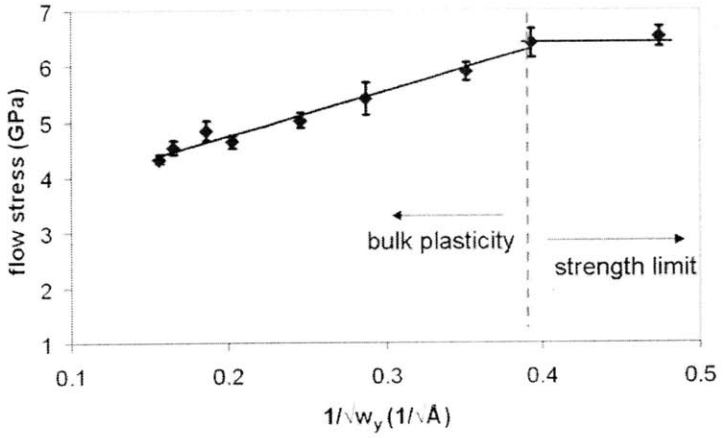

(a)

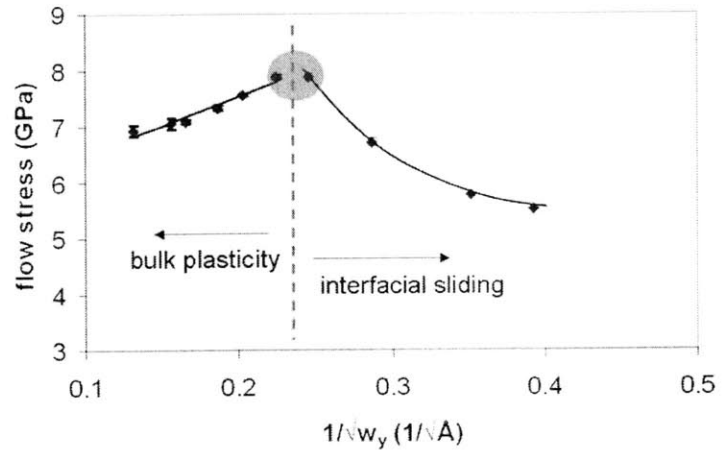

(b)

Figure 3-8: Effect of interfacial strength on flow stress by varying the composite size, by scaling dimensions in same ratio. Panel (a) displays effect of system size on flow stress for "strong" interface, showing a Hall-Petch like behavior up to a strength limit. Panel (b) shows the effect of system size on flow stress for "weak" interface showing transition from Hall-Petch like to inverse Hall-Petch like behavior at small scales. The circled region shows the length scale at which this transition occurs.

We observe a significant qualitative difference in behavior, depending on the type of interface between the platelet and matrix. The structure with "weak" interface has an optimal size at which the flow stress is maximal, whereas, the structure with "strong" interface reaches a strength limit at lower sizes. The structure with "weak" interfaces features dislocation sliding, and interfacial debonding mechanisms activated under plastic deformation. At small sizes, these become the dominant mechanisms due to the increase in interfacial area in the structure. This is reminiscent of the grain size dependence of yield stress in nanocrystalline metals, and hence the small size regime is referred to as *inverse* Hall-Petch behavior in Figure 3-8b. The "strong" interface structure, on the other hand, has only bulk dislocation mechanisms for plasticity.

The study of interfacial strength suggests that the optimal size of platelets for maximum flow stress strongly depends on the interfacial strength. For interfaces of high strength, which suppress interfacial sliding altogether, the results suggest that there exists a critical size below which the flow stress is size-independent.

3.4.2 Sensitivity analysis of design parameters

The sensitivity of changes in flow stress to changes in any of the five parameters is analyzed to determine the important ones which greatly influence the yielding behavior. The sensitivities are measured as rates of changes of flow stress with parameter change, and results are shown in Figure 3-9. The figure illustrates that platelet offset and transverse spacing are the most significant parameters that control the flow stress. The platelet offset affects the flow stress by changing the local load distribution, whereas transverse spacing has an affect through a Hall-Petch grain size-like effect.

3.5 Strength saturation with size

We observe that the interfacial strength between matrix and platelets is a key parameter that determines the importance of sliding and decohesion as deformation

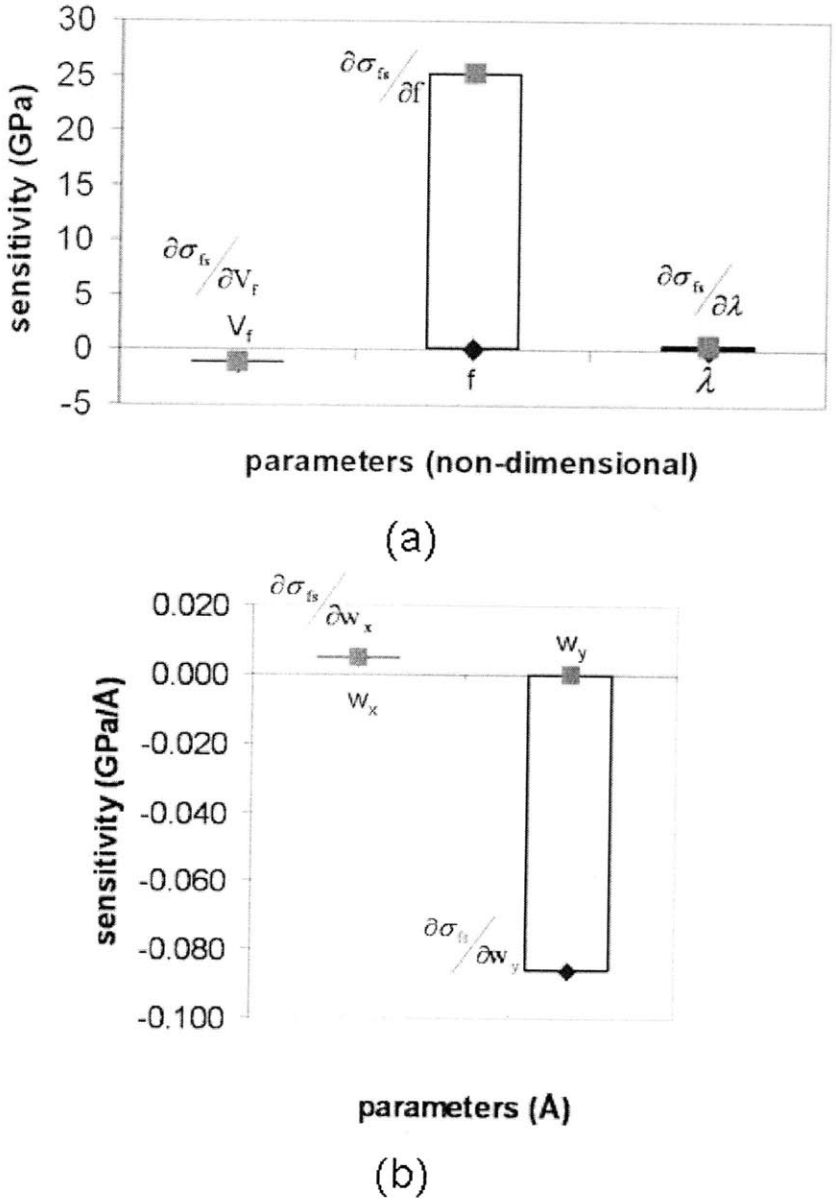

Figure 3-9: Sensitivity of flow stress to different design parameters as measured by rate of change of flow stress to parameter value change. Panel (a) shows sensitivity limits (minimum-to-maximum) to non-dimensional parameters, that is, volume fraction, platelet offset and aspect ratio. Panel (b) shows the sensitivity limits of dimensional parameters, *i.e.*, axial spacing and transverse spacing.

mechanisms at small spacing and platelet sizes. This leads to a peak flow strength for the nanocomposite as a function of platelet size (observed at a critical length scale of 17 Å for the "weak" interface considered here). However, when the interface is strong enough to prevent sliding and platelet pullout well after the matrix has started deforming plastically, we observe no such peak flow strength. Instead, we see a strength saturation for platelet spacing below a certain value. This raises interesting questions about what happens to plasticity mechanisms in the matrix under confined conditions (bound by interfaces with platelets on top and bottom). To understand this strength saturation more carefully, we devise experiments to study the effect of specimen size confinement on dislocation plasticity mechanisms in the following sections.

3.6 The size confinement effect on dislocation plasticity

Confinement effects have been previously suggested as an explanation for the high strength of nanostructured materials. It has been suggested that the underlying physical reason is that the nucleation and propagation of dislocations becomes increasingly difficult under reduction of the material size. For example, size effects in nanocrystalline materials [116, 117, 118, 119] and nanostructured ultra-thin films [120, 121] suggest fundamental changes in deformation mechanisms once the dimensions of the microstructure approach nanoscale, often characterized by the breakdown of complete dislocation mechanisms [122, 123, 124] and dominance of interfacial processes.

However, up until now a systematic, joint atomistic-nanomechanical analysis of size effects of ductile materials has not been reported. Earlier studies have been carried out by explicitly including the material nanostructure (e.g. polycrystalline metals [116, 117, 119]). However, due to the complexities of the nanostructures in these materials these studies have not yet enabled a systematic investigation of size effects limited purely to dislocation processes, since other competing phenomena (e.g. grain boundary mechanisms) have been present.

Here we investigate the atomistic mechanisms of plastic deformation of a ductile single crystal under size confinement effects via a combination of theoretical and molecular dynamics analyses. The goal of this analysis is to show that geometric confinement of materials can control the deformation mechanism, once the material dimensions reach a characteristic length scale. We design a simplistic thin strip single crystal model system that enables us to focus solely on size effect studies of mechanisms of full and partial dislocation plasticity. This is admittedly simple model system, however, enables us to investigate fundamental length scale limits associated with dislocation mechanisms.

3.7 Theoretical analysis of the size confinement effect

Our theoretical analysis is based on the Rice-Peierls model [111] that predicts a critical energy release rate for nucleation of leading and trailing partial dislocations from a crack tip as a function of the unstable stacking fault energy γ_{US} and the stacking fault energy γ_{SF}. We consider a thin strip geometry with width ξ and a semi-infinite crack of length $a >> \xi$ on a single $\{111\}$ slip plane, as shown in Figure 3-10. The choice of this model is motivated by the fact that this geometry is accessible to both theoretical and molecular dynamics studies. In this geometry, the semi-infinite crack plane and slip plane in an elastically isotropic material coincide, and a dissociated dislocation will move out from the crack tip in the slip plane under pure mode II loading. For this geometry, the critical energy release rates for nucleation of the leading and trailing partial dislocations from the crack tip are [111]:

$$G_{\mathrm{II},1}^{\mathrm{crit}} = \left(1 + (1-\nu)\tan^2\phi_A\right)\gamma_{\mathrm{US}}, \tag{3.3}$$

$$G_{\mathrm{II},2}^{\mathrm{crit}} = \frac{1-\nu}{2\mu}\left(\sqrt{\left(1+(1-\nu)\tan^2\phi_B\right)\left(\gamma_{\mathrm{US}}-\gamma_{\mathrm{SF}}\right)}+\frac{\mu\, b_A\left(\cos\phi_A+(1-\nu)\tan\phi_B\right)}{(1-\nu)\sqrt{2\pi\, r_A}}\right)^2 \quad (3.4)$$

with,

$$\frac{r_A}{b_A} = \frac{\left(G_{II,1}^{crit}/G_{II,2}^{crit}\right)^2\left[\cos^2\phi_A+(1-\nu)\sin^2\phi_A\right]\left(\mu b_A/\gamma_{US}\right)}{4\pi\,(1-\nu)\left[1-\sqrt{1-\left(\gamma_{SF}/\gamma_{US}\right)\left(G_{II,1}^{crit}/G_{II,2}^{crit}\right)^2}\right]^2}, \quad (3.5)$$

where ν is Poisson's ratio, μ is the shear modulus, b_A is the partial dislocation Burgers vector length, and r_A denotes the separation distance between the two partial dislocations, and ϕ_A, ϕ_B are the angles between the partials Burgers vectors and the X-axis in the slip plane [111].

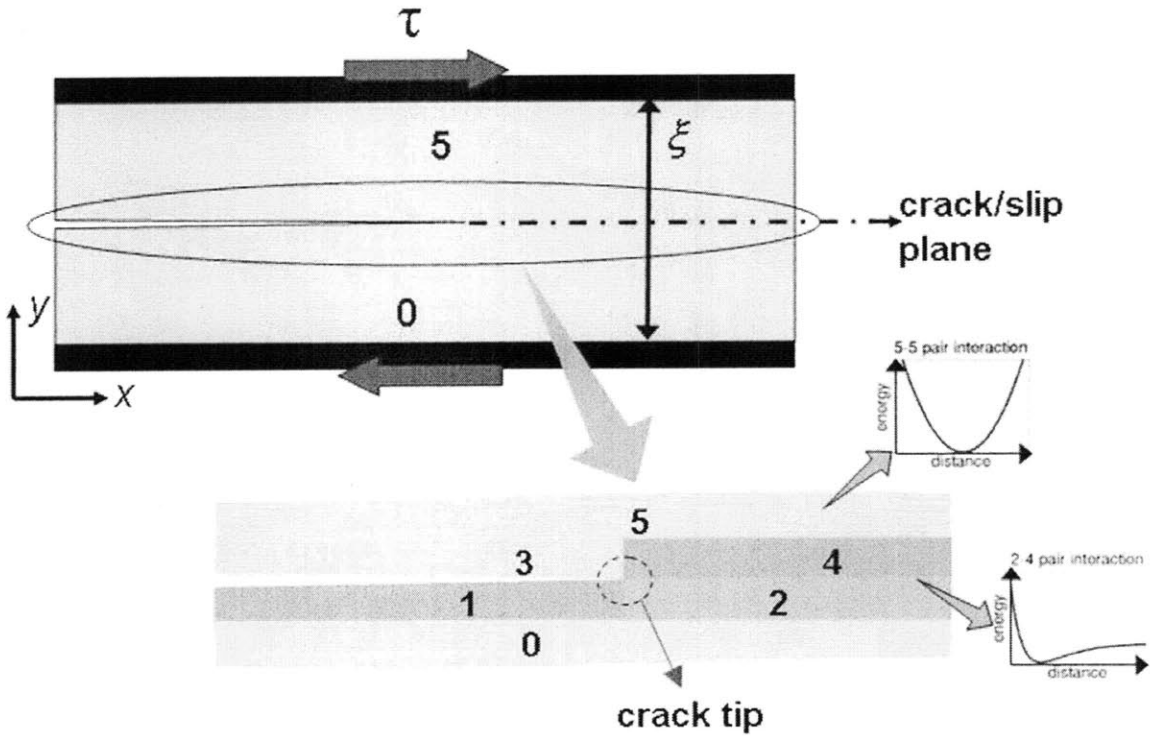

Figure 3-10: Configuration and atomistic interactions of the thin strip geometry. Crack length from left end of sample to crack tip is 300 Å. Morse interactions are defined across the slip plane/ crack plane, *i.e.*, for pairs of atoms in regions 1-4, 2-3 and 2-4; there are no interactions across the slip plane for regions 1-3 (signifying the crack region); and all other interatomic interactions are harmonic pair potentials.

We consider this model crack-slip plane system bounded within a slab of height ξ (see Figure 3-10). The energy release rate G for this thin slab geometry is [125]:

$$G = \frac{\tau^2}{2\mu}\xi. \tag{3.6}$$

Setting G equal to $G_{II,\,i}^{crit}$ (that is, we require that $G_{II,\,i}^{crit} = G$) leads to a critical load $\tau_i^{crit} = \sqrt{2\mu G_{II,i}^{crit}/\xi}$ $(i = 1, 2)$.

Since $\tau_i^{crit} \sim 1/\sqrt{\xi}$, the strength of the crystal increases as its size is reduced. However, the strength of the single crystal must be limited by the theoretical shear strength τ^{th}, the strength limit associated with homogeneously shearing the crystal. Thus at small dimensions, the crystal must fail by homogeneous shear across the crack plane, representing a breakdown of the ability to fail under dislocation nucleation.

We now consider an FCC crystal with a [110] x-direction and a (111) crack plane. This implies that the two partials to emerge in the (111) slip plane will be at ± 30 degrees orientation relative to the x-axis in the x-z plane. By setting $\tau = \tau^{\text{th}}$, we obtain two critical length scales,

$$\xi_1^{crit} = 2\mu G_{II,1}^{crit}/{\tau_{FCC}^{th}}^2 \text{ and } \xi_2^{\text{crit}} = 2\mu \text{G}_{\text{II,2}}^{\text{crit}}/{\tau_{\text{HCP}}^{\text{th}}}^2. \tag{3.7}$$

We note that after the first partial or uniform shear event, the slip plane contains an HCP stacking fault region, with $\tau_{HCP}^{\text{th}} \neq \tau_{FCC}^{\text{th}}$ (Figure 3-11(b)).

This model provides important predictions: At large crystal dimensions $\xi > \xi_2^{crit}$, shear deformation is mediated by nucleation of full dislocations, representing the conventional regime of plasticity. However, below $\xi \leq \xi_2^{crit}$, deformation proceeds under nucleation of only a leading partial dislocation. Nucleation of the trailing partial dislocation is then impossible since the theoretical shear strength τ_{HCP}^{th} is reached before the critical nucleation load. Moreover, below $\xi \leq \xi_1^{crit} < \xi_2^{crit}$, any dislocation mechanism disappears and failure occurs by homogeneous shear. The competing mechanisms are illustrated in Figure 3-12.

Numerical estimates of the length scales for some metals based on *ab-initio* data [126] are summarized in Table 3.2, illustrating that ξ_1^{crit} and ξ_2^{crit} are O (nm).

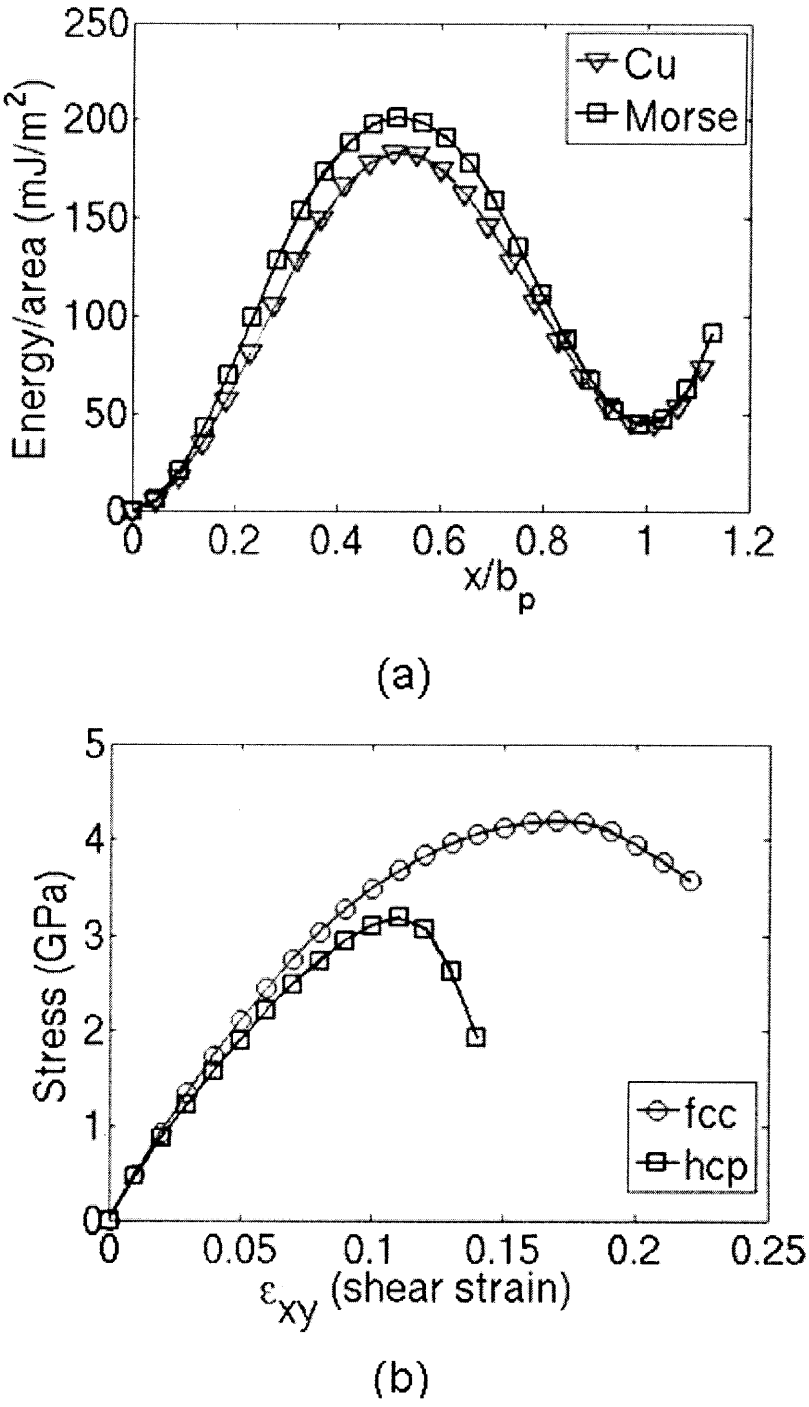

Figure 3-11: Subplot (a) shows generalized stacking fault curve (Morse potential, comparison with EAM copper). We consider 3 atomic (111) layers in the weak plane on either side of the crack plane. Subplot (b) depicts the theoretical shear strength against (111) plane shearing in the direction, for FCC and HCP stacking (Morse potential). The HCP stacking is treated as a completely faulted FCC structure, representing a close approximation to the local (111) planar arrangement after nucleation of the first partial dislocation.

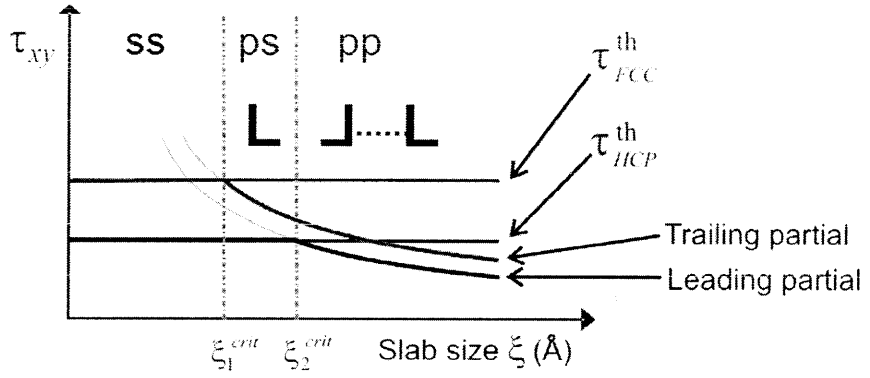

Figure 3-12: Illustration of the three regimes of pure homogeneous shear (ss), partial dislocation nucleation and shear (ps), and 1st partial and 2nd partial dislocation nucleation (pp) events on the slip plane. The two curves in the figure show nucleation stress as a function of ξ, for the 1st and 2nd partials. The horizontal lines show the theoretical shear strengths for FCC and HCP stacking. Intersection of the 1st partial nucleation curve and the theoretical shear strength for FCC crystal yields ξ_2^{crit}, and intersection of the 2nd partial nucleation curve and the theoretical shear strength for the HCP crystal yields ξ_2^{crit} .

Material	**(111)[11$\bar{2}$]**		**(111)[1$\bar{1}$0]**	
	ξ_1^{crit} (Å)	ξ_2^{crit} (Å)	ξ_1^{crit} (Å)	ξ_2^{crit} (Å)
Copper	25	21	23	51
Aluminum	13	11	12	13

Table 3.2: Summary of the two critical length scales, ξ_1^{crit} and ξ_2^{crit} for Cu and Al, considering two different crack/slip systems, both with coincident crack and slip planes. The estimates are based on *ab-initio* data for stacking fault energies and shear strengths [126], for which, τ_{HCP}^{th} is not available. Here, it has been assumed that, $\tau_{HCP}^{th} = \tau_{FCC}^{th}$

.

3.8 Atomistic simulations of the size confinement effect

The above derivation predicts a change in deformation mechanism at crack tips as the system size is reduced to the order of a few nanometers. Here we report a series of atomistic molecular dynamics simulations to directly show this effect. Simulating this behavior in a molecular dynamics simulation provides us with the atomistic details of change in mechanism as the system size is gradually changed.

We develop a simple atomistic system with coupled interatomic interactions defined by Morse [54] and harmonic potentials (Figure 3-10). We consider a two-dimensional system with a crack along a weak interface joining two harmonic crystals. All atomic interactions are harmonic except for a thin layer on both sides of the crack plane. Here, pairs of atoms which are separated by the plane of the crack, ahead of the crack tip, are allowed to interact through a simple Morse potential which allows bonds to break and shearing to take place. The crack region and crack faces are defined by zero interactions across the crack plane from the edge of the sample to the crack tip. Harmonic interactions define the interactions between pairs of atoms on the same side of the shear plane on both sides of the crystal. The choice of these simplistic potentials is dictated by our goal to focus on fundamental concepts of metallic systems, that is, their ability to undergo localized or homogeneous shear deformation along specific slip planes for different crystal sizes. The use of harmonic potential interactions between atoms on the same side of the crack plane, allows us to ensure existence of a single slip plane to ensure that twinning is impossible [127]. This atomistic model resembles the case considered in the theoretical calculations. Even though we have chosen a specific thin strip geometry, our model includes the key characteristics of the conditions that define the onset of plasticity, that is, the competition between release of elastic energy and the energy required to nucleate partial dislocations. Since plasticity can in general be described based on this framework, our model provides generally valid results, for cracks of any size under geometric confinement regardless of the details of boundary conditions.

We emphasize that this model system is deliberately designed to be such a simple representation, and that its simplicity is not a due to the lack of the ability to build a more complex representation of nanoscale plasticity. Further, our atomistic model is not designed to make quantitative predictions. Instead, our model is developed to capture the most significant physical quantities and processes involved in dislocation nucleation – elastic energy stored in the bulk (harmonic potential) released to induce localized shear in a slip plane (Morse potential). Thus, for the specific case considered here, our atomistic model does not have limitations compared with EAM potentials [56]. Similar concepts of mixed pair potentials (harmonic potentials of different types) have been used earlier to study hyperelasticity at crack tips in dynamical fracture [108].

The Morse and harmonic potentials used in the atomistic model are defined in section 2.1.2 and reproduced here:

$$V_{ab}^{Morse}(r) = \varepsilon_{ab}\left[\left\{1 - \exp\left(-\alpha_{ab}\left(r - \sigma_{ab}\right)\right)\right\}^2 - 1\right], \tag{3.8}$$

and,

$$V_{ab}^{harm}(r) = \frac{1}{2}k_{ab}\left(r - r0_{ab}\right)^2. \tag{3.9}$$

The variables $V_{ab}^{Morse}$and V_{ab}^{harm} are the potential energies for a and b atom type interactions of Morse and harmonic character respectively. ε_{ab}, α_{ab}, σ_{ab} are Morse parameters and k_{ab}, $r0_{ab}$ are harmonic potential parameters for a-b atom type interactions. We choose ε_{ab}= 0.2926 eV, α_{ab}= 1.7866 Å^{-1}, σ_{ab}=2.7110 Å with $r$cut=5.1 Å for the Morse potential; and k_{ab}= 20.0 eV/Å, $r0_{ab}$= 2.675 Å (only nearest neighbor harmonic interactions). The Morse potential parameters lead to γ_{US} = 200 mJ/m^2 and γ_{SF} = 40 mJ/m^2 (values for Cu), with τ^{th}=4.25 GPa (FCC) and 3.25 GPa (HCP) (Figure 3-11(a)). The spring constant k of the harmonic potential controls the elastic strain energy stored in the bulk crystal under shear strain and is set to a value such that the harmonic bulk modulus is ten times the size of the pure Morse-potential bulk modulus.

The system considered here has a length of 3.000 Å and a thickness of 30 Å,

whereas the height parameter ξ is varied between 30 Å and 60 Å to investigate size effects. The crack length a = 300 Å in all simulations. The system is loaded in shear by displacement boundary conditions at the top and bottom. A microcanonical ensemble with a time step of 2.5 fs and a low starting temperature at 0.1 K is used. The shear strain rate is 3.5E7 sec^{-1} (for all systems).

3.9 Results and Discussion

We carry out a systematic study of the deformation mechanisms while varying ξ. First, we study the shear activity at the slip plane under the lateral shear loading using an atomic slip vector analysis [91]. The change in the x-component of the slip vector (measured 500 Å ahead of the crack tip) versus the simulation time is shown in Figure 3-13, measuring the relative shear displacement of the upper and lower part. We observe two distinct shear events for each slab size. Notably, the character of the shear events changes from a smooth continuous profile at smaller slab sizes to a sudden jump at larger dimensions.

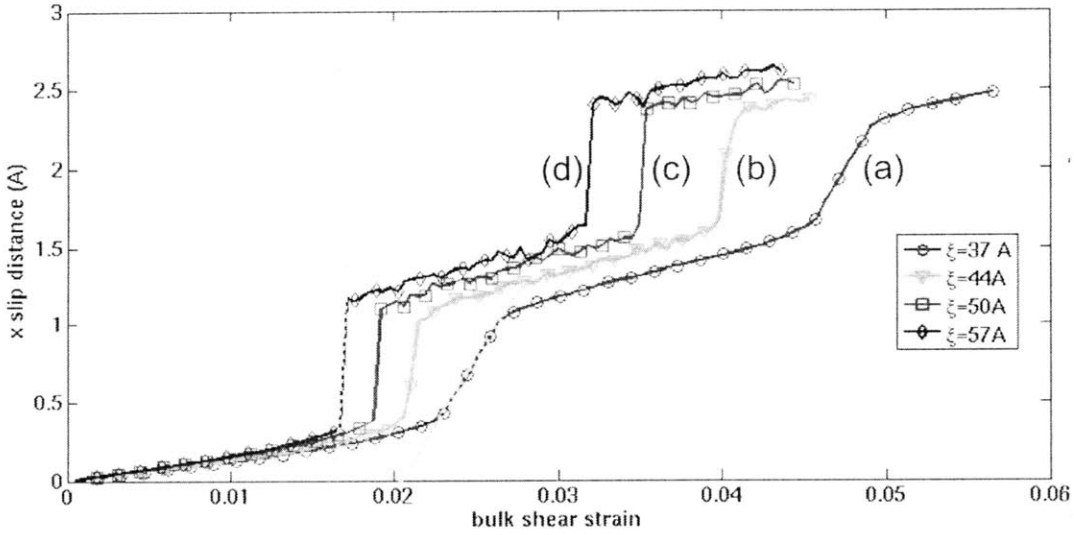

Figure 3-13: Variation of x-component of slip vector in the x-direction with bulk shear strain, at a distance of 500 Å ahead of the crack tip. The curves show slip vector plots for various slab heights.

To elucidate the atomistic details of the deformation mechanism, we plot the

variation of the x-component of the slip vector across the entire slip plane in the x-direction at times close to the particular shear events (Figure 3-14 for the first, Figure 3-15 for the second). Comparing these plots with the results shown in Figure 3-13 reveals that the jagged jumps indeed represent the emergence of partial dislocations from the crack tip, and the smooth transitions represent uniform, homogeneous shear across the whole slip plane.

This agrees with the notion that each shear event is a competition between nucleation of a dislocation at the crack tip and a homogeneous shear event that is not localized at the crack tip. After the first partial or uniform shear event, the slip plane has a stacking fault region and then the second partial/uniform shear event has modified energy barriers to overcome because of the change in stacking sequence ahead of the crack tip. If the second event is a non-local homogeneous shear event on the slip plane, the modified barrier is the energy to shear planes in a HCP configuration; whereas if it is nucleation of the second partial, the modified barrier can be treated as a combination of a reduced energy barrier due to presence of a higher energy stacking fault and also the stress shielding effect of the presence of the first partial in the vicinity of the crack tip.

The results shown in Figures 3-14 and 3-15 confirm the predictions of the theoretical analysis. For the smallest slab size (37 Å), the two shear events represent homogeneous shear along the $[11\bar{2}]$ directions on the slip plane, as is clearly visible in Figure 3-14(a) and 3-15(a). As the size is increased, the first slip event changes into nucleation of a partial dislocation at the tip, as is shown in Figure 3-14(b). However, the second shear event remains nonlocalized, revealing formation of a shear displacement far ahead of the tip (Figure 3-15(b)). At larger slab heights, both first and second shear events are identified as partial dislocations nucleating at the crack tip, forming a complete dislocation (Figure 3-14(c) and 3-15(c)).

We note that the critical length scales associated with the nucleation of the first and second partials are very similar for the $(111)[11\bar{2}]$ system (Table 3.2). Thus the regime of a single partial dislocation ('ps' in Figure 3-12) is extremely difficult to observe. This is reflected by the results shown in Figure 3-15(b) that, while providing

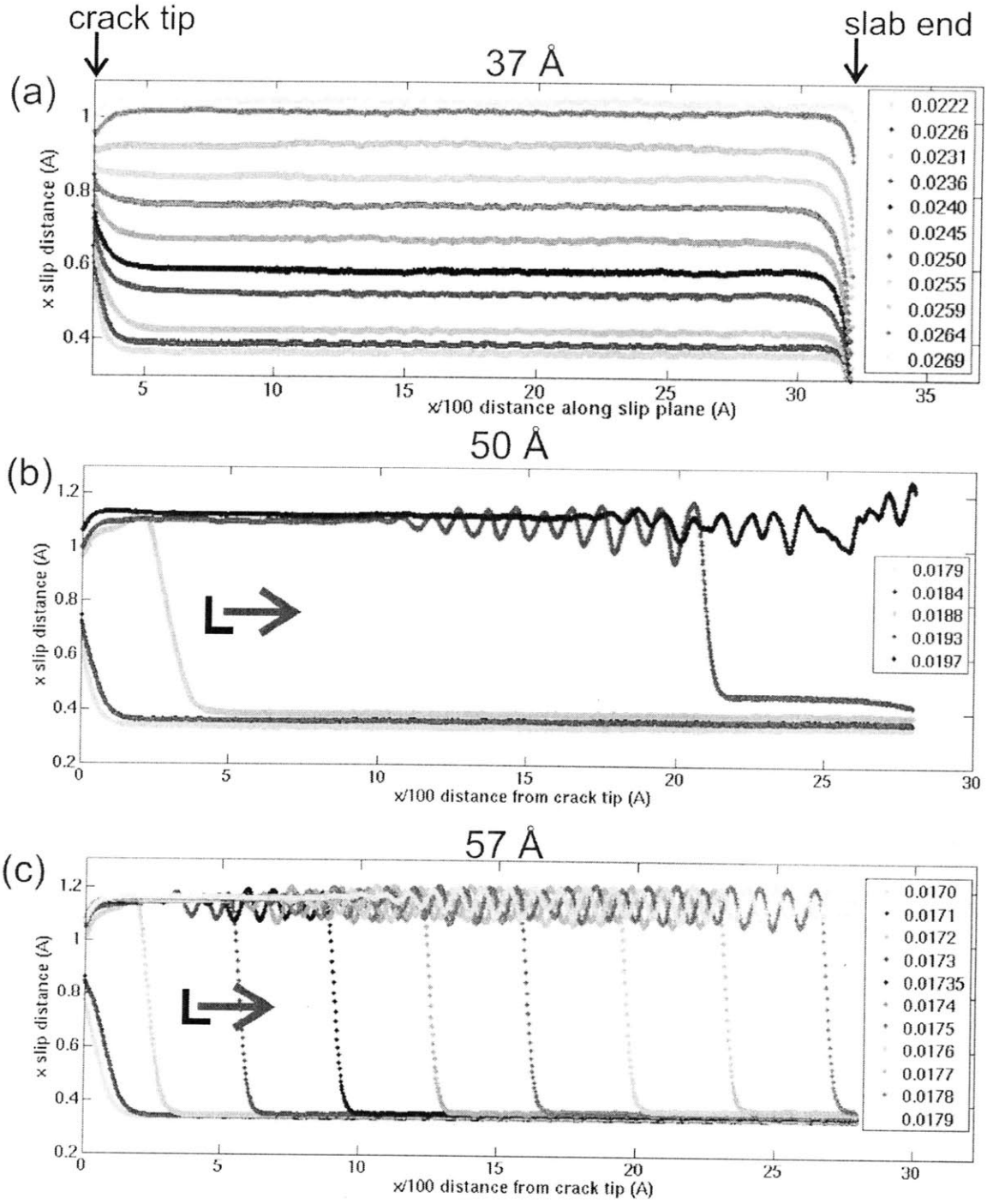

Figure 3-14: Variation of x-component of slip vector along the slip plane x-direction from the crack tip to the slab end (first shear event), for slab sizes (37 Å, 50 Å and 57 Å). The numbers in the legend show the corresponding applied strain values. The results show a transition from uniform shear across the slab length ((a)) to partial dislocation nucleation at crack tip ((b) and (c)).

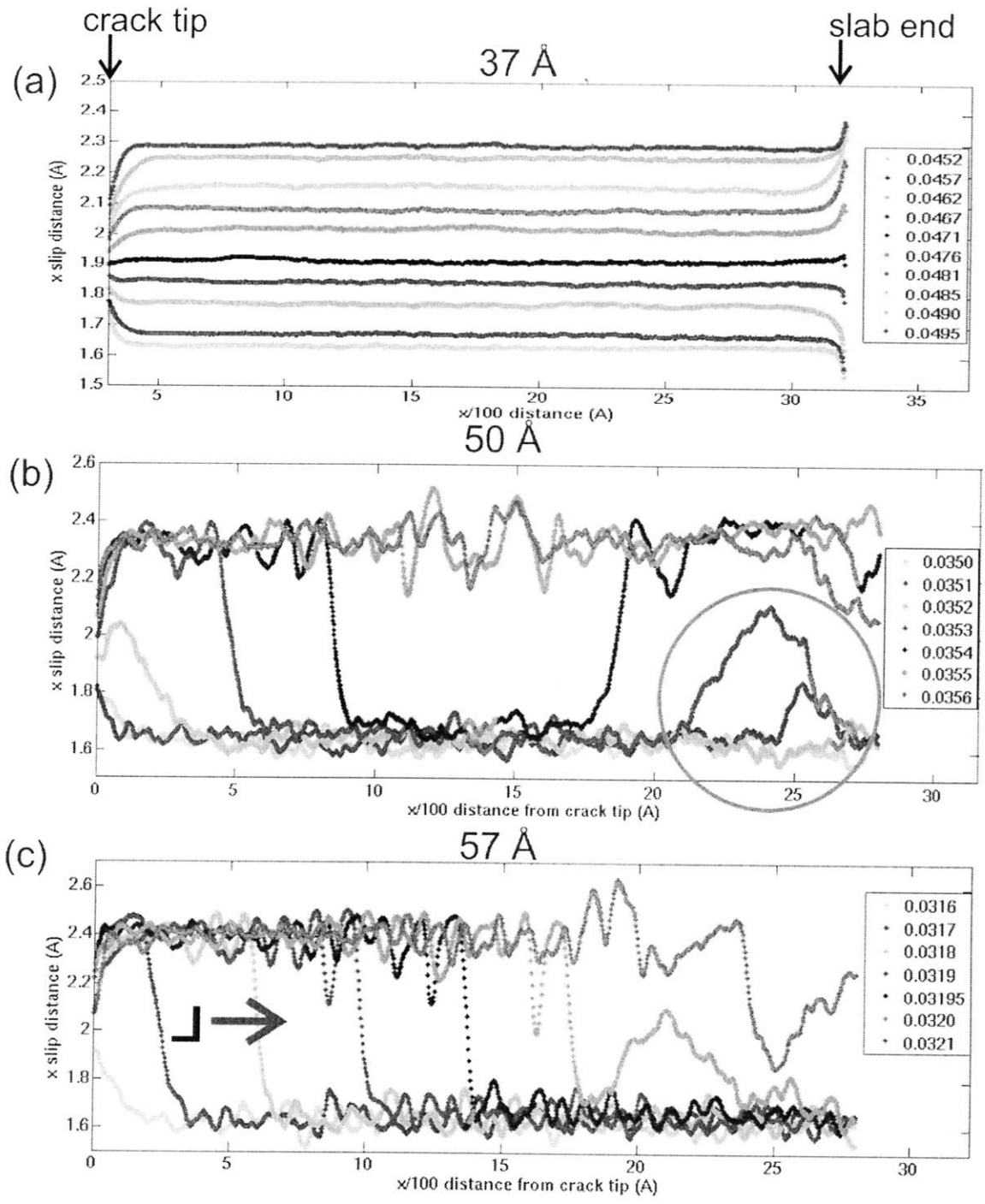

Figure 3-15: Variation of the x-component of the slip vector along the slip plane. (a) reveals uniform shearing across the slab length. (b) reveals that shear deformation occurs also ahead of the crack tip (marked by the circle), indicating that the deformation mechanism is not controlled by the crack tip stress field but occurs homogeneously along the weak plane. (c) shows nucleation of the trailing partial dislocation.

some evidence for nonlocal slip, do not clearly reveal homogeneous shear as observed in Figures 3-14(a) and 3-15(a).

In summary, our theoretical and numerical analysis revealed that there exist fundamental length scales that depend only on material parameters, controlling the deformation mechanism. The theoretical calculations show us that these characteristic length scales are on the order of a few nanometers for metals such as Cu and Al. Moreover, theoretical calculations for inclined slip planes at the crack tip, that is, not lying in the crack plane, show a characteristic length scale for dislocation nucleation that would be larger by a factor of $\approx$2 than this simple case [111], bringing the numerical estimates to the range of 5 to 10 nm (based on the estimates shown in Table 3.2). Considerations of crystal anisotropy change the characteristic length scale further by $\pm$ 50% [128]. These change the characteristic length scales while maintaining the same order of magnitude.

A crack tip stress field rises from a discontinuity in interactions along the crack tip line across a plane, giving rise to a stress field $\sigma_{ij} \sim 1/\sqrt{r}$ for a semi-infinite crack under far-field uniform K_{II} loading. Whereas our study has been limited to a cracked thin strip geometry, one can extend these models to other cases, e.g. to rigid-compliant interfaces in composites or grain boundaries in nanocrystalline materials.

Our analysis [129] is directly applicable in the design of bone-inspired metallic nanocomposites, covered earlier. Figure 3-16 illustrates the application of the size effect discussed in this section for the analysis of the flow stress of a bioinspired nanocomposite discussed earlier [106]. Figure 3-16(a) shows the geometry of a nanocomposite composed of a soft, ductile matrix and hard, brittle platelets. The application of uniaxial tensile load reveals that large shear stresses are transferred between the platelets as shown in Figure 3-16(b), leading to nucleation of dislocations in the matrix phase during plastic deformation. Therefore the characteristic dimension ξ (characterizing the thickness of the ductile matrix material) controls the flow stress level, and at small dimensions below the characteristic length scales it is expected that dislocation based deformation breaks down. Figure 3-16(c) depicts an analysis of the flow stress as a function of the building block size, for a different

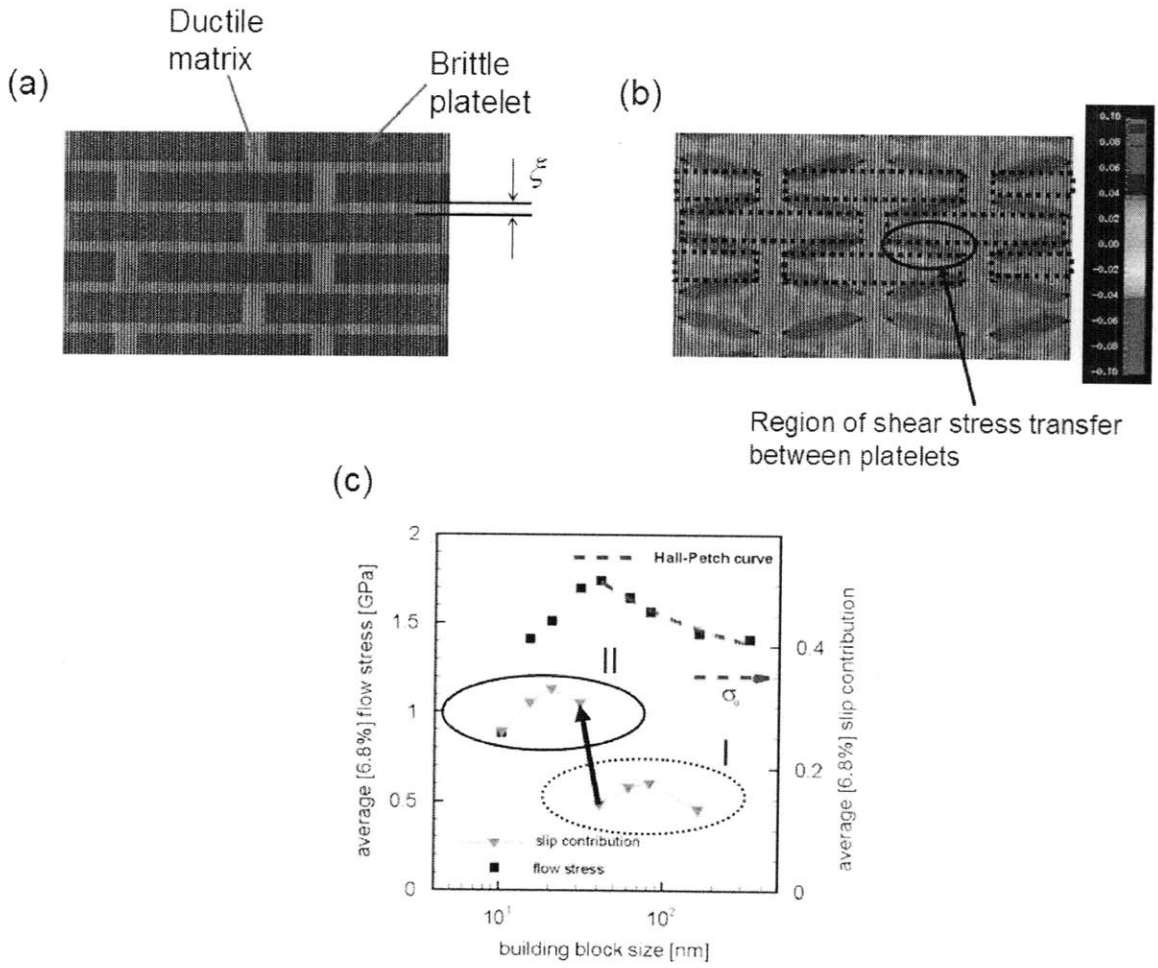

Figure 3-16: Illustration of the application of the size effect discussed here for the analysis of the flow stress of a bioinspired nanocomposite [106]. Subplot (a) shows the geometry of a nanocomposite, also shown in Figure 3-1. The application of uniaxial tensile load reveals that large shear stresses are transferred between the platelets (subplot (b)), leading to nucleation of dislocations in the matrix phase during plastic deformation. Therefore the characteristic dimension ξ controls the flow stress level, and at small dimensions below the characteristic length scales it is expected that dislocation based deformation breaks down. Subplot (c) depicts an analysis of the flow stress as a function of the building block size, for a Ni-Al nanocomposite [105] possessing the same design morphology, showing that the flow stress increases with a reduction of the building block size (notably, the strengthening behavior agrees well with the predicted scaling) then reaches a maximum at a critical building block size, followed by a decay. This transition corresponds to the breakdown of dislocation activity in favor of interfacial slip (between Ni and Al particles), as is revealed by the analysis of interfacial slip (green curve in subplot (c), transition from regime I to regime II).

Ni/Al nanocomposite with the same design morphology [105], showing that indeed the flow stress, increases with reduction of ξ, then reaches a maximum at a critical building block size, followed by decay. This transition corresponds to the breakdown of dislocation activity, as is revealed by the analysis of interfacial slip (green curve, transition from regime I to regime II). Notably, the strengthening behavior agrees well with the predicted scaling $\tau_i^{crit} \sim 1/\sqrt{\xi}$, providing further evidence that the simple model captures the essential features of the flow stress hardening process.

In nanocrystals, the grain boundaries are sites of weaker stress concentration than crack tips, and there exist several other accommodating mechanisms. Our system was deliberately designed so that it only contains two failure mechanisms; realistic systems contain other failure mechanisms (grain boundary sliding, twinning, diffusion). Thus, in nanocrystals, change in plasticity mechanism due to geometric confinement can be considered to be only one of several length scales of importance in the competition between different deformation mechanisms [123, 130, 131, 132].

Since these other geometries feature a weaker stress concentration, our analysis provides a *lower* bound for the critical length scales. This can be explained by considering the scaling relation of the change of the characteristic length scales. The condition for nucleation of a dislocation can be generally written as $G_{II,\,i}^{crit} = G$. Since $G \sim K_{II}^2 \sim \xi$, a change in K_{II} to αK_{II} leads to a change of $\xi \sim G_{II,i}^{crit}/\alpha^2$. Therefore for $\alpha < 1$ the characteristic length scales ξ_i^{crit} increase. Thus, while the basic physical mechanisms are captured appropriately in our simple model, for many applications the critical length scales may be several times larger than those reported here.

Our theoretical system was deliberately designed so that it only contains two failure mechanisms. Realistic systems contain other failure mechanisms (grain boundary sliding, twinning, diffusion). This may explain why transitions of mechanisms in experiments and simulations of nanocrystalline metals have been observed at larger scales than those listed in Table 3.2. MD simulations [105, 130, 131, 133] and experiments [123] of nanocrystalline metals have shown that that at grain sizes below $\approx$20 nm, all dislocation plasticity arises at grain boundaries. Further, this gives rise to twins and stacking faults across the grains, that is, complete dislocations are not

observed at these grain sizes [130, 131, 132, 133].

The partial dislocations that give rise to these features are emitted from grain boundary dislocation networks close to triple junctions [130]. These are possible locations where high energy and low energy grain boundaries meet, and stress relaxations along particular grain boundaries leads to stress concentration at the junctions. The atom packing and thus interatomic bonding is quite different between these sections of the grain boundaries which produce a stress concentration field at the intersection of these regions in the plane of the grain boundary when a shear stress is applied across the two grains sharing the boundary. The change in bonding arrangement is not as sharp as for a crack tip. Thus the stress field falls off much slower as a function of distance to the grain boundary than it is the case for a sharp crack. This implies that our calculations are a *lower* bound on the characteristic crystal sizes that have change in mechanism. In agreement with this notion, at sizes below $\approx$10 nm both experiments and simulations show breakdown of any dislocation activity either from grain boundaries or the bulk. All plastic deformation is accounted for by grain boundary sliding, atomic shuffling or grain boundary diffusion as accommodating mechanisms [130, 131]. This shows a fundamental application of our length scales which limit dislocation nucleation to the problem of change in plasticity mechanism as grain size is reduced in the nanometer scale. Even though the model reported here does not provide a quantitative link, it leads to an explanation of the underlying physical mechanisms.

Similar considerations apply for the mechanics of thin film systems. It has been reported that dislocation activity is absent in nanocrystalline thin films of average grain size of 10 20 nm grain size under tensile deformation [120, 133]. Earlier MD studies have also shown that plasticity from threading and parallel glide plane dislocations is seen to be absent at a length scale below 25 nm [133].

Our theoretical analysis has also used in the design of bone-inspired metallic nanocomposites. Figure 3-16 illustrates an application of the size effect discussed in this study for the analysis of the flow stress of a bioinspired nanocomposite. Figure 3-16(a) shows the geometry of a nanocomposite composed of a soft, ductile matrix

and hard, brittle platelets. The application of uniaxial tensile load reveals that large shear stresses are transferred between the platelets as shown in Figure 3-16(b), leading to nucleation of dislocations in the matrix phase during plastic deformation. Therefore the characteristic dimension ξ (characterizing the thickness of the ductile matrix material) controls the flow stress level, and at small dimensions below the characteristic length scales it is expected that dislocation based deformation breaks down. Figure 3-16(c) depicts an analysis of the flow stress as a function of the building block size, showing that indeed the flow stress, increases with reduction of ξ, then reaches a maximum at a critical building block size, followed by decay. This transition corresponds to the breakdown of dislocation activity, as is revealed by the analysis of interface slip (green curve, transition from regime I to regime II). Notably, the strengthening behavior agrees well with the predicted scaling $\tau_i^{crit} \sim 1/\sqrt{\xi}$, providing further evidence that the simple model captures the essential features of the flow stress hardening process.

To the best of our knowledge, this study is the first to systematically show intrinsic length scale limitations to plasticity, along with direct confirmation by atomistic simulation. A related behavior has been observed in simulations of failure of thin metal nanowires (diameter $\approx$15 Å) under tension, where a competition between homogeneous shear and dislocation nucleation is controlled by the energy of slip across cross-section of nanowire and the self-energy of the dislocation [134]. The analysis reported here is similar to earlier work in brittle materials [33], where a single critical length scale has been proposed below which no brittle fracture mechanism can occur (the 'flaw-tolerance' length scale). Interestingly, for plasticity, two critical length scales exist, provided that full dislocations are split up into two partial dislocations as it occurs in many FCC metals.

3.10 Conclusions

Our analysis reveals that there exist fundamental, intrinsic length scales that depend only on material parameters and the particular geometry that control the plastic de-

formation mechanism and strength properties in metallic nanocomposites. Our study may be vital in the analysis and design of new nanomaterials, for instance bioinspired nanocomposites, providing concrete design suggestions and associated mechanistic models. Specifically, in agreement with earlier findings [135, 33] we find that the use of elongated platelets of high aspect ratio and staggered arrangement of platelets for optimal load transfer, and control of spacing between layers of platelets are critical factors in strengthening the material. We also observe that the strength of the matrix-reinforcement interface determines the optimal size of the second phase platelets at which the maximal flow strength is observed.

To the best of our knowledge, unlike earlier studies of similar geometries, here we have for the first time explored a much larger parameter space and provided a detailed investigation of associated mechanical properties and their relationship to the underlying nanostructural design. This provides details insight into structure-property relationships in this class of materials from a bottom-up atomistic perspective that explicitly includes dislocation mechanics and interfacial phenomena.

We summarize the main results of the study of dependence of strength of bone-inspired metallic nanocomposites on their design:

1. Reinforcing phase platelets arranged in staggered rows with the stagger perpendicular to the direction of loading lead to optimal load transfer in the nanocomposite. A stagger of 0.25 to 0.75 leads to a characteristic tension-shear load transfer in platelets/matrix that maximizes the flow stress.

2. Reinforcing phase platelets with large aspect ratio with the long edge in the direction of loading lead to higher flow stress. Beyond a critical aspect ratio (larger than 4 for materials considered here), the flow stress saturates, and this parameter has no further effect.

3. The spacing between platelets perpendicular to the direction of loading (transverse spacing) has a Hall-Petch like effect on flow stress with the spacing mimicking the grain diameter.

4. The volume fraction of the second phase, while keeping the aspect ratio and platelet spacing constant, does not have a significant effect on flow stress. This result provides strong evidence for the significance of the specific geometry, and suggests that nanoscale control of structure and shape of platelets is crucial to maximize material performance.

5. A comparison of the effect of various geometrical effects on flow stress shows that a factor of 1.94 improvement over the unreinforced matrix flow strength is possible by systematically engineering the nanostructured design.

6. The interfacial strength between matrix and platelets is a key parameter that determines the importance of sliding and decohesion as deformation mechanisms at small spacing and platelet sizes. This leads to a peak flow strength for the nanocomposite as a function of platelet size and spacing.

Our analysis also reveals that there exist fundamental, intrinsic length scales that depend only on material parameters and the particular geometry that control the plastic deformation mechanism in small crystals under confined conditions. These characteristic length scales separate regimes of no dislocation activity, partial dislocation plasticity, and complete dislocation plasticity at a crack tip in ductile metals. We have confirmed this effect by direct atomistic simulation of a model system under shear mode II loading with coincident crack and slip planes. We have also shown the applicability of this concept to the interfacial effect on strength we observe in the metallic nanocomposites. Confined ductile phases, in such materials, will show a transition to homogeneous shear based plasticity below a critical length scale. This could provide important guidance for the optimal design of such nanocomposites, as the ductile phase will fail at their theoretical strength and any further reduction in the critical dimension will not increase the failure strength.

The study reported here illustrates that universally observed biological nanostructures might provide effective design solutions for structurally strong materials. Thereby, the design of a material's nanostructure is a crucial element in achieving

superior mechanical properties. By utilizing functional building blocks such as metals, ceramics or polymers it might be possible to add additional functionality to the materials, beyond structural mechanical properties. By the control of interfacial properties, e.g. by sensitive polymers that respond to external cues such as magnetic fields, light or chemical environment [136], it might be possible to engineer novel responsive, active and tunable materials with substantial variations in mechanical properties.

The use of metals in the design of bioinspired structures is, however, a costly proposition, due to the economic cost of the raw materials. The design of bioinspired structures would be economically much more feasible, if it could be undertaken with very cheap raw materials. Silica, found abundantly in sand, is one such cheap, however structurally 'poor' material. Is it possible to use silica as the building block of a bioinspired structure, which will provide excellent mechanical properties? In the next chapter, we turn for inspiration to the exoskeleton of diatoms, a silica-based biological material. We present the design and mechanical properties of diatom-inspired silica nanostructures.

Chapter 4

Ductility enhancement through diatom-inspired nanoporous silica design

Silica is one the most abundant minerals in the earth's crust, known for its hardness and brittle fracture behavior. Silica is its amorphous glassy form or crystalline quartz form is considered a prototype of a perfectly brittle ceramic material, with little to no plastic deformation prior to fracture, and thus following the Griffith's criterion of fracture [137, 138]. In biology, silica structures have been observed to be assembled up from the nanoscale in honeycomb and porous form [139]. For example, nature shows the use of porous silica structures in the exoskeleton of diatoms [140, 141, 142, 143]. In diatoms, a porous hierarchical structure dominates the landscape of the cell wall and encompasses intricate patterns that are highly varied and ordered, as shown in Figure 1-2, and reach all the way down to the nanoscale. A marine diatom species (*Concinodicus* sp.), seen in Figure 1-2, possesses a silica-based exoskeleton (called frustule-external surface of the diatom at a micron scale) made up of porous parts arranged in a hierarchical fashion, with areola pores, the internal surface of the diatom (at micron length scale); the 2nd central porous layer, the cribrum (with pores at a sub-micron length scale); and the cribellum, the external porous layer (with pores at a nanometer length scale). Beyond the key biological functions of the cell wall

lie important mechanical functions, such as preventing virus penetration, protecting diatoms from the jaws of predators, or even protection from digestion in some cases [144, 145]. It is intriguing that a material that is so brittle in its engineering form, is used by nature as the major constituent of the protective casing of these species.

The question of the mechanical properties of these silica structures is key to understanding their use in the exoskeletons [39]. Some recent experimental studies that revealed the mechanical properties of diatom shells were covered in Chapter 1, section sec:hierarchyeffectfailure. Briefly, they have been found to possess high strength, and carry large reversible elastic strains. Also large variations in mechanical properties have been observed to be influenced by pore size, pore distance, porosity and under different biomineralization processes [40, 41].

In accordance with our aim in Chapter 1, we thus want to study the effect of (a) nanostructuring, and, (b) the use of hierarchical assembly, on silica material design. We study in this chapter firstly, the effect of nanostructuring on silica, and the mechanical properties of nanoporous diatom-inspired silica structures.

4.1 Background on nanoscale silica structures

Nanoporous silica structures have been also designed in the lab [146, 147], and have great utility as catalysts and adsorption media. They could also be used as templates for assembling other materials into nanostructures. However, their mechanical properties have not been investigated, and it remains unknown how they perform mechanically, in particular under extreme loading or deformation. This is important for the reliability of the application devices, where issues such as fracture properties are essential. A detailed analysis of the mechanics of nanoporous silica structures can also be used to discover design criteria to maximize their load-carrying and fracture-resistant capacity, and open up new applications for these structures in novel materials.

One-dimensional (1D) structures of silica, silica nanowires, have also been under investigation experimentally and theoretically for possessing potential applications

as structural building blocks in nanoelectronics and optics. Precise measurement of their mechanical properties is important, as mechanical failure of these blocks may lead to failure of the entire devices. Several experiments show that there exists a size-dependent brittle-to-ductile transition in these nanowires. Amorphous silica nanowires of 50-100 nm diameters, obtained using chemical vapor deposition techniques, have been shown to exhibit brittle fracture under bending loads [148]. However silica nanowires of diameters down to 20 nm, created using physical taper-drawing, show pristine smooth surfaces and great deformability, with the ability to be assembled into spiral coils, nanorings and nanoloops [149]. Also, crystalline SiC, another brittle ceramic, has been shown to exhibit plastic deformation for nanowires with diameters below 100 nm, under bending loads through lattice disordering and amorphization. Silicon nanowires with diameters below 60 nm show large plastic deformation before fracture, through emission of dislocations, amorphization and necking [150].

An understanding of silica behavior at the nanoscale is thus critical to understanding the mechanics of nanoporous silica structures and their role in the structure of diatom exoskeletons, and also the mechanics of silica nanowires. Though there exists an abundance of literature on their optical properties, the mechanical properties of silica structures at the nanoscale, whether they are nanowires or nanoporous, have been difficult to measure experimentally due to problems in fabricating structures with no surface defects (smooth surfaces) and problems in loading setup, with some exceptions [149, 150]. Atomistic simulations with accurate descriptions of silica behavior are a critical way to obtain insight. Previous work by the authors on the modeling of the behavior of nanoporous silica structures using atomistic modeling has shown increased ductility with a reduction in the constituent silica strut size, and a change of fracture behavior from brittle crack propagation to ductile failure with size scaling [151]. In this work, we use atomistic simulations and theoretical nano-mechanical analysis to understand the enhanced ductility and toughness seen in these nanoporous structures.

4.2 Design parameters of the nanoporous silica structures

Here we follow the structural framework of diatoms closely, such that it resembles their porous structure at the smallest hierarchy level of the cribellum, with pores at a nanometer size scale, resulting in a similar model system of silica as shown in Figure 4-1. The nanoporous structures thus designed will also subsequently be referred to as nano-honeycomb structures due to their 2-dimensional periodic symmetry and similarity with macroscopic honeycombs. The widths w of the nano-honeycomb structures are controlled in our analysis, and range from 5 Å to 72 Å (the upper size is limited by computational resources). The approach pursued here is guided by our desire to develop a general model system in which we can test the effect of the size (geometric confinement) of the nanostructure on the bulk material behavior. By systematically varying the size and hierarchy of the constituting silica nanostructure, we examine associated mechanical properties, as well as fracture and toughening mechanisms, facilitated through a series of molecular dynamics simulations.

4.3 Materials and methods

At the nanoscale we use molecular dynamics simulations to study the mechanics of the nanoporous silica structures. To describe the inter-atomic interactions, we use the first-principles derived ReaxFF force field [62] (see Chapter 1, section 2.1.2). The ReaxFF description for Si-O systems, is based on a bond-length bond-order description and fitted to density-functional calculations of energy landscapes of bond-distortion, breaking and forming events of various Si-O reactions. A variety of Si-O clusters are used for fitting parameters, as also energetics of bulk crystalline phases of silicon and silica under tension and compression. The ReaxFF potential has been used successfully in predicting fracture phenomena in silicon and silica [86, 104, 70, 152], and interfacial structure at silicon/silica interfaces [71, 153].

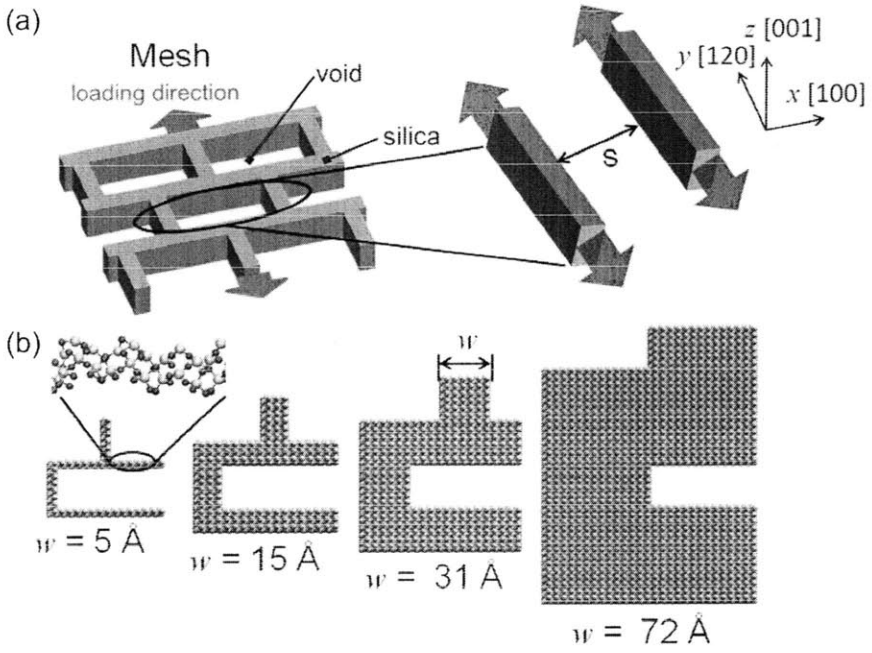

Figure 4-1: Geometry of the bioinspired silica structure, and setup used in our simulations. Panel (a): Three-dimensional schematic of the silica nano-honeycomb structure (shown on left), with periodic boundaries along the X, Y, and Z directions. On the right, the geometry and loading of the individual silica struts are shown. The crystallographic orientation is the same for all silica structures considered. The arrows indicate tensile load applied uniformly along the structure. Panel (b): Initial geometry of nano-honeycomb structures considered here, illustrating the wall width (w, definition indicated in one of the structures) variation in the geometry. The inset shows a detailed view of the relaxed surface structure.

4.4 Deformation of nano-honeycomb silica structures

Here we present our analysis on the effect of changing the wall width on the mechanical properties of the silica nano-honeycomb(see Figure 4-1(a) for the geometry considered). As shown in Figure 4-1, the honeycomb wall widths are varied between $w = 5$ Å to 72 Å for the structures.

Figure 4-2 shows the stress-strain response of the nano-honeycomb structure for varying widths w. The structures show an increase of deformation in the plastic regime, a lower modulus, and lower maximum stress with decreasing wall width. Even though silica is considered a brittle material, the results show that it is possible to transform it into a ductile system for small nanoscale wall widths which reach a maximum failure strain of ≈120%.

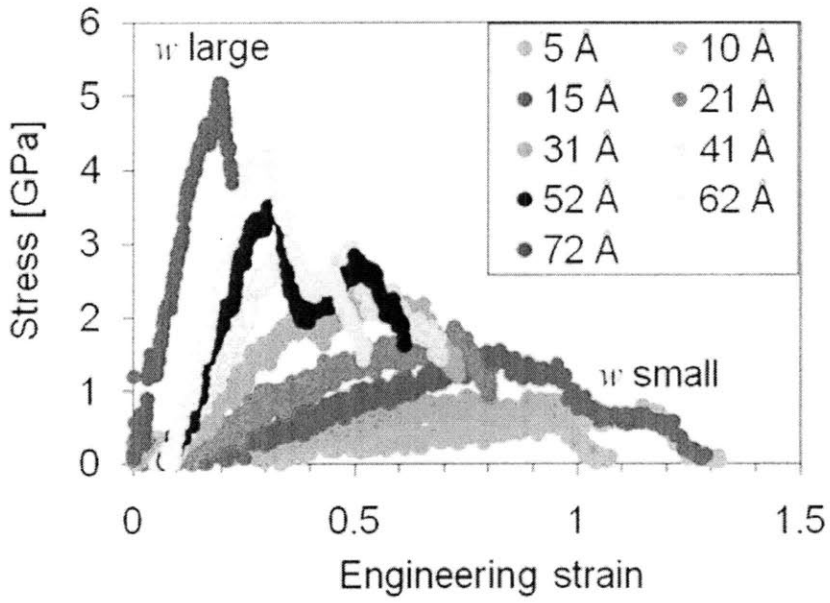

Figure 4-2: Stress-strain graphs for silica nano-honeycomb structure for all sizes (wall widths range from $w = 5$ Å to 72 Å). For wall widths below ≈60 Å, we observe the existence of a plastic deformation regime. The greatest deformation is obtained for the smallest wall width of 5 Å. Failure mechanisms are characterized by crack initiation and propagation, or, shearing followed by nanoscale void formation and coalescence.

We proceed with analysis of the silica meshes as shown in Figure 4-3, which shows

the equivalent von Mises stress field at the maximum stress. For larger wall widths, high stress is mostly concentrated on the surface and specifically near the edges, thus suggesting possible locations for crack or shear nucleation. However, with lower wall widths, the stresses become relatively homogeneous throughout the structure. For large deformation, the void shapes gradually change from a rectangular to a hexagonal one for decreasing wall widths, and can be clearly seen for $w \leq 31$ Å.

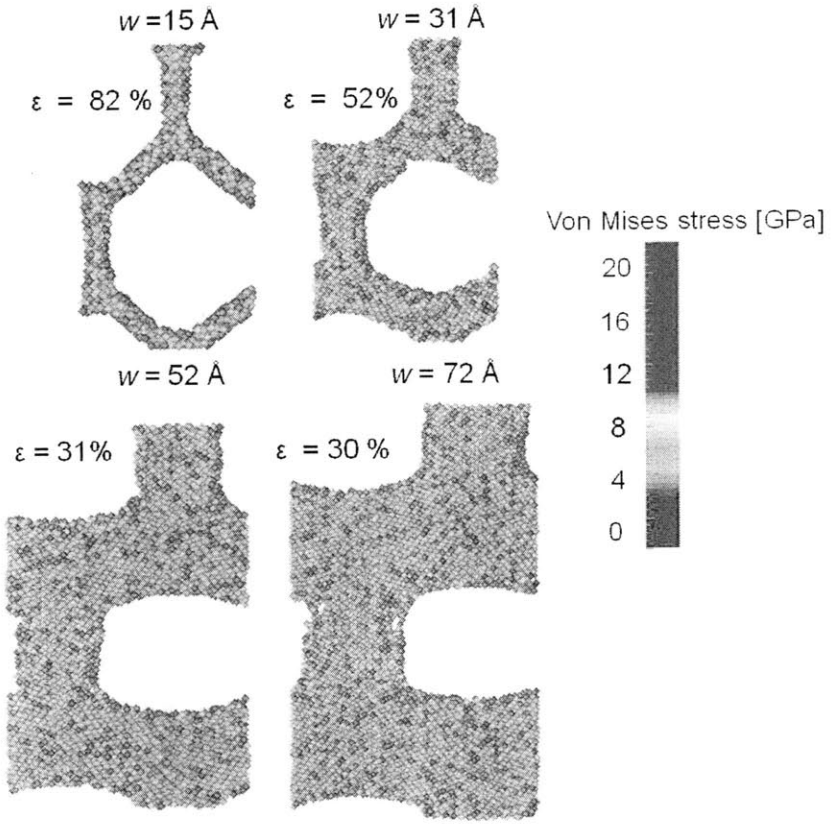

Figure 4-3: Von Mises stress field at the maximum load, for different nano-honeycomb wall widths (the strain value at which the snapshot was taken is indicated in the plot). For widths smaller than ≈31 Å, the structure at the maximum load becomes hexagonal, and the stress is distributed homogeneously throughout the structure. For larger wall widths, high stresses are concentrated around the corners. Moreover, the initial, rectangular shape of the structure is maintained. In order to improve image clarity, we only show the stress values associated with silicon atoms within the silica system.

The analysis sheds some light on the remarkable stress-strain response of nano-honeycomb structures with thin wall widths, as shown in Figure 4-2. A key feature is the geometric pattern that allows large deformations to be accommodated by the mesh by changing from a rectangular pattern to a hexagonal one at large strains (see,

e.g. in Figure 4-3), specifically for wall widths below 31 Å. The reason for these very large strains without failure seems to be due to the more homogeneous distribution of stresses and the geometry transformation from rectangular to a hexagonal shape for smaller wall widths. In the next few sections, we develop detailed theoretical models to explain and predict this increase in ductility with decreasing wall size precisely.

4.5 Analysis of deformation using theoretical models

The atomistic studies show the effect of pore size, distribution and porosity on elastic modulus, plasticity, ductility and toughness of the structures. In the next section, the underlying mechanisms are discovered through a systematic analysis of the earlier simulation results. Also, continuum elasticity theory and fracture mechanics, using atomistic simulation data, are used to make theoretical predictions of structural stiffness and strength for varying geometry. The theoretical predictions provide design guidelines for how to make nanoporous materials that show enhanced ductility, plastic flow, and toughness.

4.6 Results and discussion

We study the mechanics of silica nanoporous structures whose morphology is shown in Figure 4-4a. The structures consist of rows of rectangular pores arranged in a staggered fashion, as seen in several natural and man-made nanoporous structures. The structures can be uniquely identified by the inter-pore distance and the size of the pores, and will hereafter be referred to by three numbers, (pore distance t, pore length p_l, pore width p_w) (see Figure 4-4a). The material considered is silica in its α-quartz polymorph, which is the stable crystalline form at room temperature and pressure. The structure is free of any grain boundaries or initial defects. All structures are periodic in all 3 directions, and loading is achieved by deformation of the system in the Y direction. System evolution is studied through molecular dynamics simulations

using the canonical ensemble with the Berendsen thermostat [47]. A time step of 0.2 fs is used to advance the dynamics and a deformation strain rate of $1 \times 10^{10} s^{-1}$ is applied. All simulations are carried out in GRASP [154], a parallelized code for large scale ReaxFF simulations. Figure 4-4(b) shows the stress-strain curves for some of the different nano-honeycomb structures of silica that were analyzed. There is a marked difference from a typical macroscopic brittle ceramic honeycomb stress-strain curve, which shows brittle fracture at a few percent strain [139].

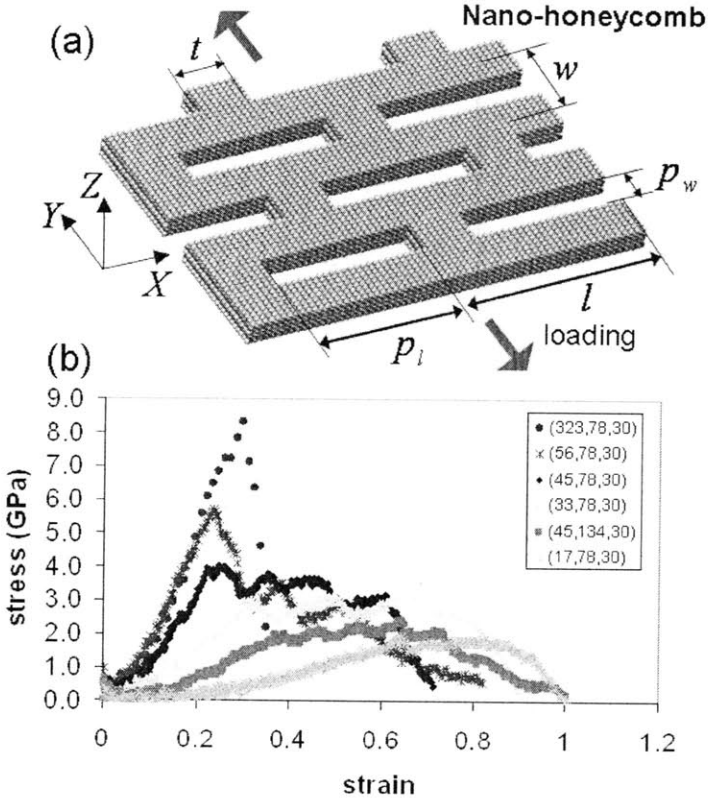

Figure 4-4: Geometric shape classification and stress-strain behavior for the nano-honeycomb silica structures; several more structures showing ductile response are analyzed here, apart from Figure 4-2. (a) shows the geometry of the nano-honeycomb structures under consideration with 3 independent parameters required for the geometric shape classification (e.g. t, p_l and p_w), (b) show stress (σ_{YY})-strain curves obtained from atomistic simulations of different nano-honeycomb structures. The legend shows the classification of the structures, which is shown as (t, p_l, p_w) parameters for each structure, values given in Å. The (323 Å, 78 Å, 30 Å) structure shows purely brittle fracture, the (56 Å, 78 Å, 30 Å) structure shows simultaneous plasticity and crack propagation in different struts, the rest of the structures show ductile fracture.

4.6.1 Elasticity

The nanostructure can be considered to consist of a collection of interlocking struts, some of which are initial horizontally oriented (length in the X direction) and the others vertical (length in the Y direction) and are referred to as such in the rest of this study. Our simulations show that the elastic response of the structure depends on the ratio of the strut length to its thickness (l/t in Figure 4-4(a)), or its slenderness ratio.

For short struts with small l/t ratio ($l/t < 1.67$), the load transfer is as follows. Figures 4-5(a) and (b) show the atomic-level tensile and shear strain distribution for the (45 Å, 78 Å, 30 Å) nanoporous structure. Also, Figures 4-5(c) and 4-5(d) shows a Z-section slice of the structure while undergoing elastic deformation. Both the load distribution and the deformation profile of the Z-plane cross-section, show that the vertical struts are mainly under pure tensile load, whereas the horizontal struts are under pure shear load. The total tensile deformation in the structure can thus be written as,

$$w\varepsilon_{22}^{T} = (l-t)\sin\phi + w\varepsilon_{22}^{w}; \tag{4.1}$$

where t is the thickness of the struts, w is the height of the vertical strut and l is the length of the horizontal strut, ϕ is the angle the length of horizontal strut makes with the X axis, as shown in Figure 4-6a, and ε_{22}^{T} and ε_{22}^{w} are the tensile strains in the overall structure and the vertical struts respectively.

For small deformations, $\sin\phi \approx \tan\phi \approx \varepsilon_{12}^{l}$, where$\varepsilon_{12}^{l}$ is the shear strain in the horizontal strut. Thus Equation 4.1 can be written as:

$$\begin{aligned} \varepsilon_{22}^{T} &= \tfrac{l-t}{w}\varepsilon_{12}^{l} + \varepsilon_{22}^{w} = \tfrac{l-t}{w}\tfrac{\tau}{\mu_{12}} + \tfrac{\sigma}{E_{22}}; \\ \tfrac{\sigma_T}{E_{22}^{T}} &= \tfrac{l-t}{w}\tfrac{\tau}{\mu_{12}} + \tfrac{\sigma}{E_{22}}. \end{aligned} \tag{4.2}$$

where τ and μ_{12} are the shear stress and shear modulus for the horizontal strut, σ and E_{22} are the tensile stress and elastic modulus in the Y direction for the vertical strut, and σ_T and E_{22}^{T} are the tensile stress and elastic modulus in the Y direction for

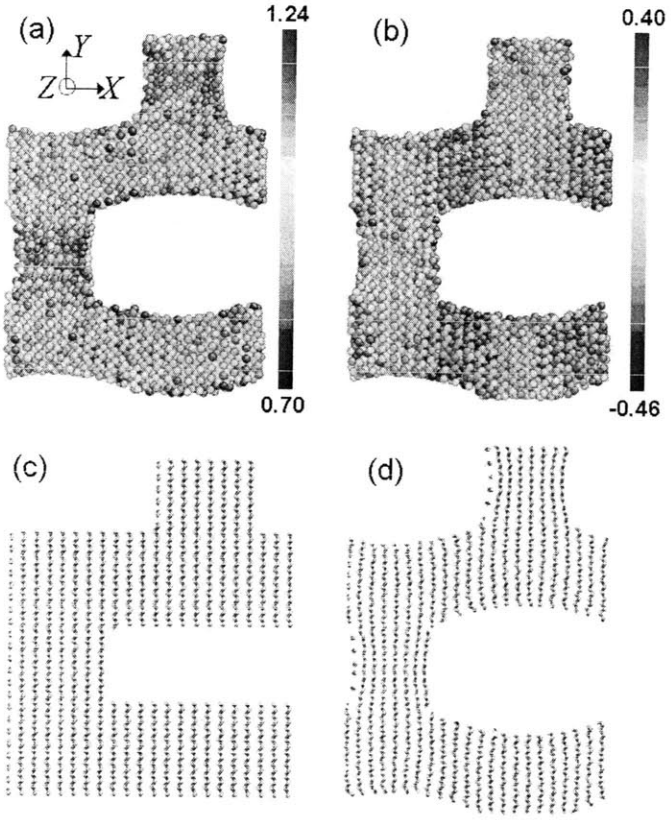

Figure 4-5: Strain plots and deformation shape analysis for a nano-honeycomb structure with thick struts. For the (45 Å, 78 Å, 30 Å) structure at an overall tensile strain of 0.105, (a) and (b) show a measure of the per-atom tensile strain and shear strain through the components of the Jacobian of the local deformation matrix, *i.e.*, J_{YY} and J_{XY} respectively. Note that only Si atoms are visualized. The strain distributions clearly show the presence of simple shear loading in the horizontal struts, and tensile loading in the vertical struts. For the (45 Å, 78 Å, 30 Å) structure, (c) shows a Z cross-section of the undeformed structure; (d) shows the same cross-section at a overall strain of 0.105. The atomic bonds clearly show the simple shear loading in the horizontal struts.

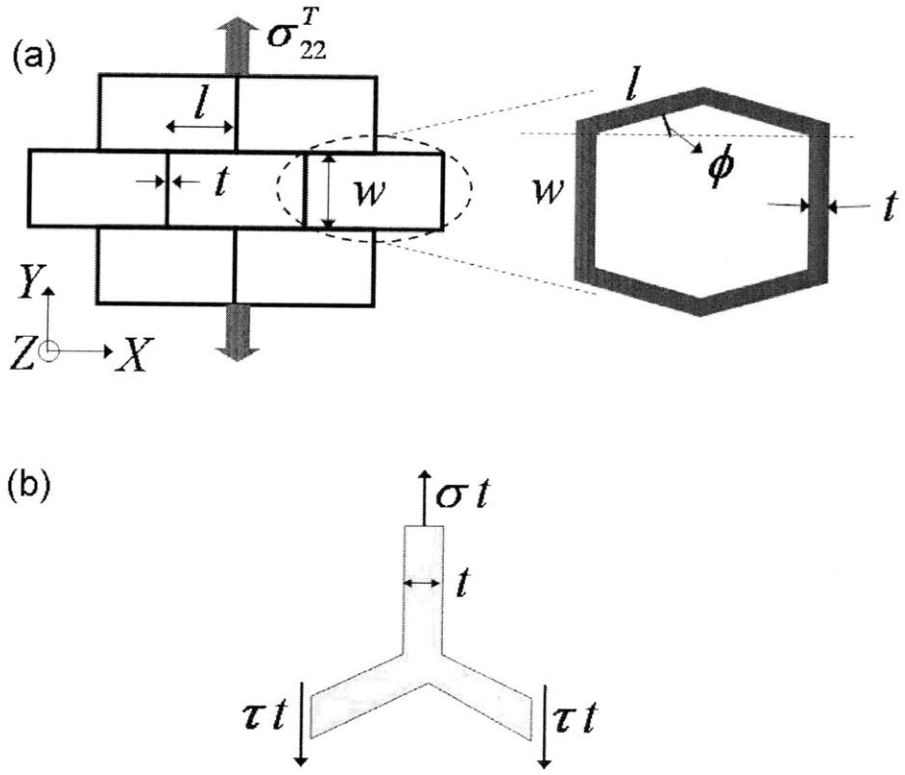

Figure 4-6: Load distribution and stress transfer for the nano-honeycombs with thick struts; (a) shows the various geometry parameters used to calculate elastic strains in the honeycomb structure, and the deformed shape for structures with thick struts, and (b) shows the load balance between the vertical and the horizontal struts.

the overall structure. Doing a force balance on the members, as shown in Figure 4-6(b), gives us, $\sigma\, t = 2\tau\, t \Rightarrow \sigma = 2\tau$. And, a force balance overall gives us, $\sigma\, t = 2\sigma_T l$. Combining these with Equation 4.2 gives us the elastic modulus of the nanoporous material,

$$\frac{1}{E_{22}^T} = \frac{2l}{t}\left(\frac{l-t}{w}\frac{1}{2\mu_{12}} + \frac{1}{E_{22}}\right) = \left(\frac{l\,(l-t)}{wt}\right)\frac{1}{\mu_{12}} + \left(\frac{2l}{t}\right)\frac{1}{E_{22}}. \tag{4.3}$$

To check the validity of Equation (4.3), by treating the geometry parameters, $l\,(l-t)\,/wt$, and $2l/t$ as variables we perform a least square curve fit over four different nano-honeycomb geometries for the overall structure elastic modulus obtained from molecular dynamics simulations (Table 4.1). These give us a shear modulus of the struts as 13.3 GPa and elastic modulus as 109.1 GPa. These can be compared to bulk α-quartz ReaxFF values of shear modulus of 14.1 GPa, Young's modulus (E_{22}) of 67.4 GPa and elastic constant C_{22} of 130.3 GPa. The calculated E_{22} lies between the Young's modulus (Poisson effect in the transverse directions) and the elastic constant C_{22} (no Poisson contraction) showing that the vertical struts have boundary conditions between these two extremes.

honeycomb	**slenderness ratio** (l/t)	$l(l-t)/(tw)$	$2\,l/t$	E(GPa)
(45 Å, 78 Å, 30 Å)	1.38	0.29	2.75	20.06
(67 Å, 112 Å, 30 Å)	1.33	0.30	2.67	22.5
(56 Å, 78 Å, 30 Å)	1.20	0.15	2.40	30.38
(67 Å, 89 Å, 30 Å)	1.17	0.13	2.33	31.98

Table 4.1: Geometric parameters and elastic moduli for nano-honeycomb structures with thick struts ($l/t < 1.67$). For the nomenclature for referring to the structure specifications, refer to Figure 4-4(a).

The pores change shape as the structure is deformed. The change in shape can be followed by the changing angle between a vertical strut and an adjacent horizontal strut, with strain. The elastic modulus equation (Equation (4.3)) can also be checked by measuring the angle of deviation of the horizontal struts from their original horizontal position as a function of strain. Equation 4.3 predicts the following relation

between the sine of the angle and applied strain,

$$\varepsilon_{22}^{T} = \left(\frac{l-t}{w} + \frac{2}{(E_{22}/\mu_{12})} \right) \sin\phi. \tag{4.4}$$

This plot is shown in Figure 4-7, for a particular nano-honeycomb structure, the (45 Å, 78 Å, 30 Å). Interestingly the sine of the angle variation remains linear with applied strain, as predicted from Equation 4.4 during elastic deformation, but the angle becomes constant on the onset of plasticity in the form of shearing in the struts.

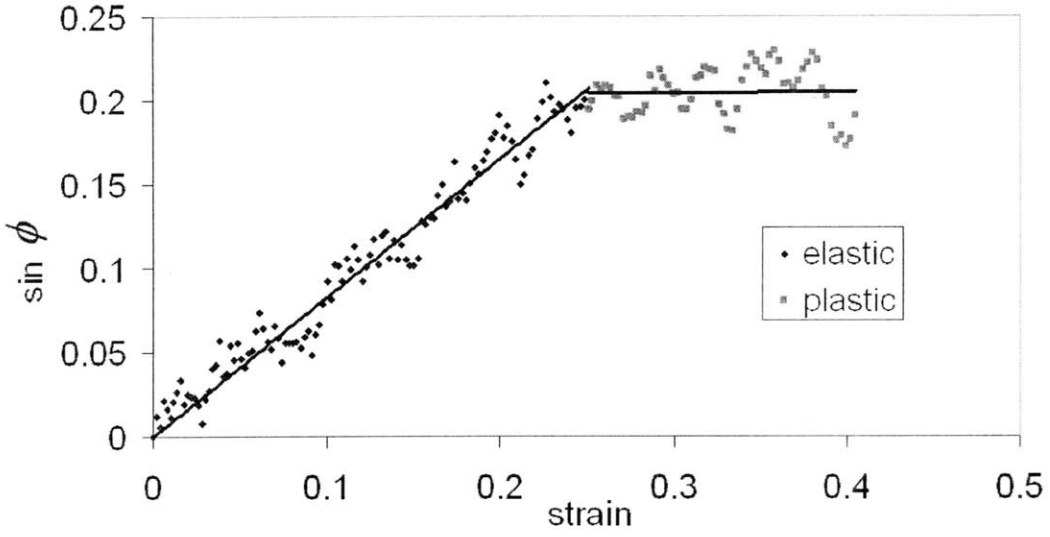

Figure 4-7: The variation in pore shape, measured through sine of the angle between the length of the horizontal strut and the X axis (see Figure 4-6), as a function of applied strain. The relation is linear on the regime of elastic deformation (part of the curve in diamond-shaped data points colored blue), as predicted by the theory. There is no change in the angle during plastic deformation (part of the curve in square data points colored pink). This shows that the pore shapes remain about the same during plastic deformation.

For structures with more slender struts, with larger l/t ratio ($l/t > 1.67$), the response of the horizontal struts are seen to be governed by bending deformation. Figure 4-8(a) and (b) show Z-section slice of the structure while undergoing elastic deformation for the (45 Å, 133 Å, 30 Å) nanoporous structure. The deformation profile of the Z-cross-section show that the vertical struts are mainly under pure tensile load, whereas the horizontal struts are under beam bending load.

In this case, the horizontal struts can be approximated as beams fixed at both

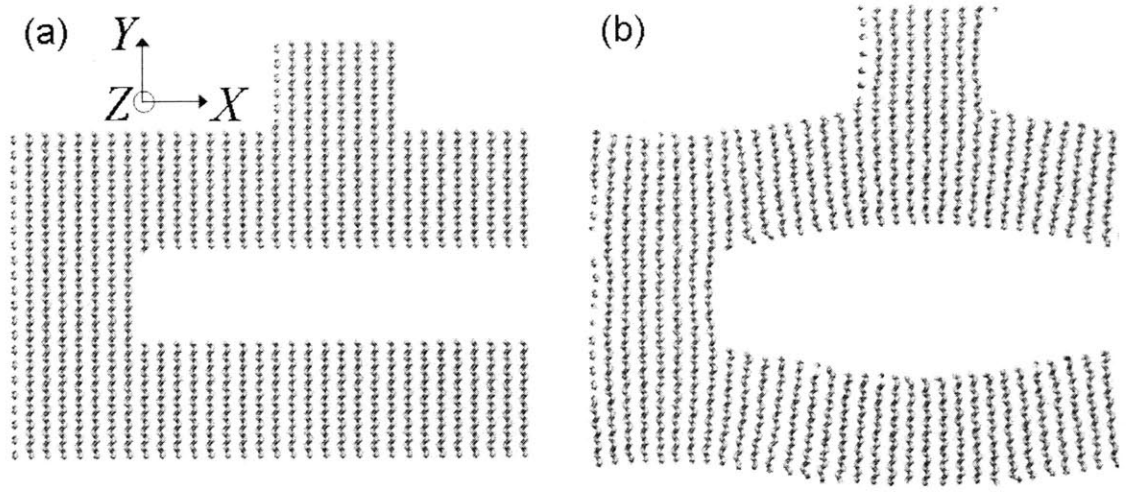

Figure 4-8: Deformation shape analysis for a nano-honeycomb structure with slender struts. For the (45 Å, 133 Å, 30 Å) structure, (a) shows a Z cross-section of the undeformed structure; (b) shows the same cross-section at an overall tensile strain of 0.133. The atomic bonds clearly show the bending loading in the horizontal struts.

ends, with a point load in the middle. The horizontal displacement can, in this case be written as:

$$\begin{aligned} &\Delta = \tfrac{P(2l)^3}{192E_{11}I}, \\ &\text{where P} = \sigma\,\text{t}\,;\ \text{I} = \tfrac{\text{t}^3}{12}. \end{aligned} \tag{4.5}$$

In this equation, Δ is the vertical displacement at the end of a horizontal strut (see Figure 4-9), P is the load on the beam, I is the moment of inertia of the strut (assuming its width in the Z direction =1), and $E11$ is the elastic modulus of the horizontal strut in the X direction. This simplifies to:

$$\Delta = \frac{\sigma\, l^3}{2E_{11}t^2}. \tag{4.6}$$

The total tensile deformation in the structure can thus be written as,

$$w\varepsilon_{22}^{T} = \frac{\sigma\, l^3}{2Et^2} + w\varepsilon_{22}^{w}. \tag{4.7}$$

Or, the total strain in the structure,

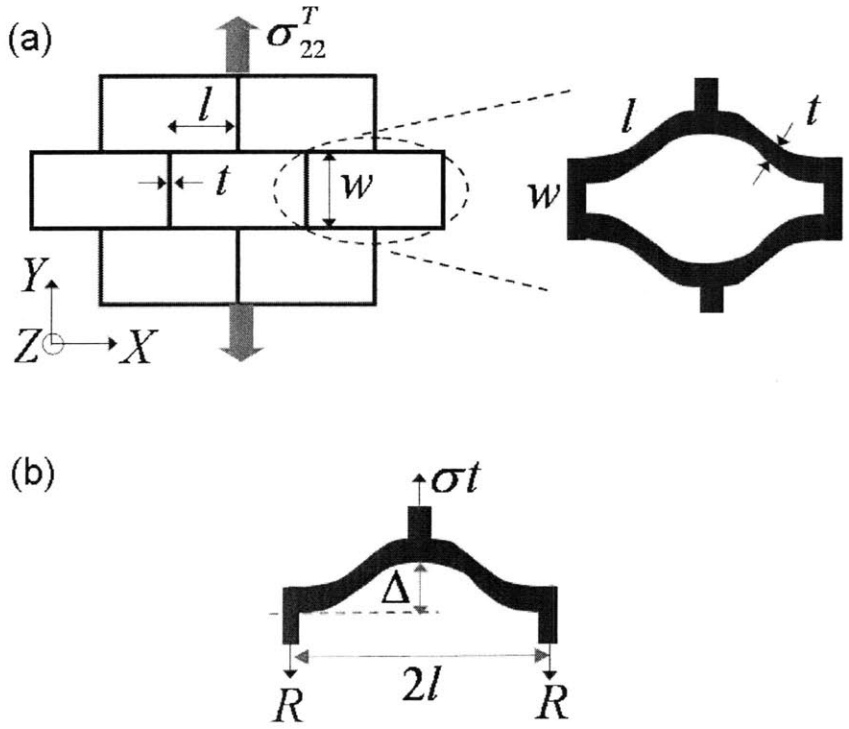

Figure 4-9: Load distribution and stress transfer for the nano-honeycombs with slender struts; (a) shows the various geometry parameters used to calculate elastic strains in the honeycomb structure, and the deformed shape for slender struts, and (b) shows the load balance and deflection relation between the vertical and the horizontal struts.

$$\varepsilon_{22}^{T} = \frac{\sigma\, l^3}{2E_{11}wt^2} + \frac{\sigma}{E_{22}}. \tag{4.8}$$

Thus the elastic modulus can be calculated as,

$$\frac{1}{E_{22}^{T}} = \left(\frac{l^4}{wt^3}\right)\frac{1}{E_{11}} + \left(\frac{2l}{t}\right)\frac{1}{E_{22}}. \tag{4.9}$$

To check the validity of Equation (4.9), treating the geometry parameters, l^4/wt^3, and $2l/t$, as variables, we perform a least square curve fit over three different nano-honeycomb geometries with slender struts for the overall structure elastic modulus obtained from molecular dynamics simulations (Table 4.2). These give us an E_{11} of the struts as 76.2 GPa and E_{22} as 104.3 GPa. These can be compared against ReaxFF values of bulk α-quartz Young's modulus in the X direction (E_{11}) of 65.8 GPa and Young's modulus in Y direction (E_{22}) of 67.4 GPa and elastic constant C_{22} of 130.3 GPa. The calculated E_{22} here too lies between the Young's modulus (Poisson effect in the transverse directions) and the elastic constant C_{22} (no Poisson contraction) showing that the vertical struts have boundary conditions between these two extremes. The calculated E_{11} lies close to the Young's modulus in the X direction, showing that the horizontal struts under bending load are almost completely under free surface boundary conditions.

honeycomb	**slenderness ratio (l/t)**	$l^4/(wt^3)$	$2\,l/t$	E(GPa)
(17 Å, 78 Å, 30 Å)	2.83	21.48	5.67	2.97
(45 Å, 134 Å, 30 Å)	2.00	9.14	4.00	6.41
(33 Å, 78 Å, 30 Å)	1.67	3.86	3.33	11.89

Table 4.2: Geometric parameters and elastic moduli for nano-honeycomb structures with slender struts ($l/t > 1.67$). For the nomenclature for referring to the structure specifications, refer to Figure 4-4(a).

4.6.2 Plasticity and failure

All nano-honeycomb structures fail either by brittle crack propagation or plastic deformation followed by necking in the struts. Here, we find the critical size parameters at which we observe this brittle-to-ductile transition. We observe that as the width of the constituent strut elements (parameter t in Figure 4-4a) is reduced, the large strain deformation behavior changes from crack initiation and propagation to plastic deformation in some of the struts. This change is seen for strut sizes of $\approx$ 60 Å, and the change is gradual, with some intermediate nano-honeycomb structures showing presence of both plasticity and crack propagation in different areas. The structures exhibiting plastic deformation show crystalline shearing of thin struts. We also observe that once plasticity starts the flow stress does not change until one of the deforming struts starts to form a neck region. Once a strut ruptures, whether through brittle or ductile fracture, other struts still carry load and thus the overall structure shows stress softening and graceful failure (as seen in the last part of the stress-strain curves in Figure 4-2).

The plastic deformation of the struts is seen to occur due to crystal slip, which will happen at the theoretical shear strength. This is in conformity with the idea of a flaw-tolerant size in brittle materials, where below a certain crystal size the presence of cracks does not affect the fracture stress and the material always fails at the theoretical strength [33]. Using this and the stress-transfer path in the structure, we can predict the yield strength,

$$\sigma^{T}_{yield} = \tau_{th}\frac{t}{l}, \tag{4.10}$$

where σ^{T}_{yield} is the yield stress of the structure and $\tau_{th}$is the theoretical shear strength in silica. Figure 4-10 shows a fit of the yield stress versus the structure geometry (t/l), which allows a prediction of the theoretical shear strength, which for silica turns out be $\approx$ 5.46 GPa. To calculate a length scale order-of-magnitude at which the flaw-tolerant behavior steps in, we have to find a strut size below which plastic deformation sets in. Assuming a maximum stress concentration at a crack

tip of a semi-infinite crack in an infinite solid of height t, and since the plastically deforming strut is under shear loading, using mode II loading equations on the crack, we get through application of the Griffith criterion,

$$G = \frac{\tau^2 t}{2\mu} = 2\gamma_S, \tag{4.11}$$

where G is the energy release rate at the crack tip, and γ_S is the fracture surface energy. So to induce plasticity, the system stress should reach the theoretical shear strength, or,

$$t \leq \frac{4\mu\gamma_S}{\tau_{\text{th}}^2}. \tag{4.12}$$

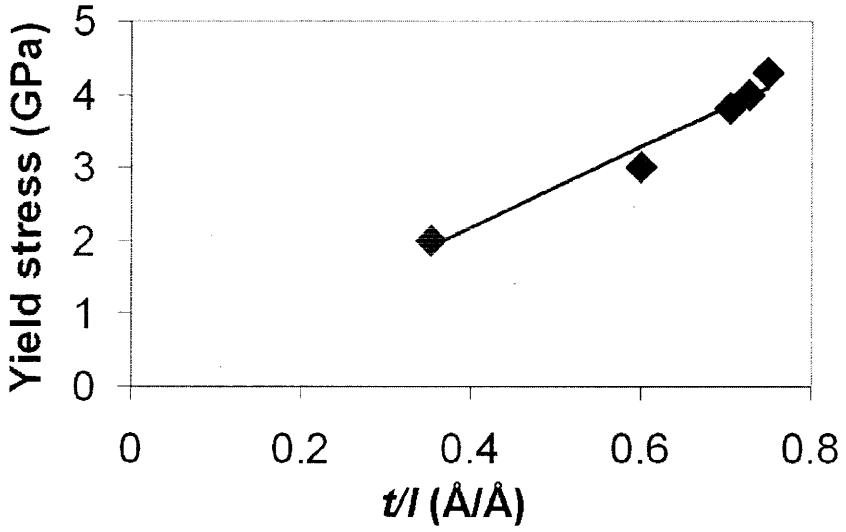

Figure 4-10: Plot of yield stress versus a geometry parameter for nano-honeycomb structures showing plastic flow. Equation (4.10) in the main text shows that the slope of the linear fit, here 5.46 GPa, corresponds to the theoretical shear strength of the struts.

Substituting values for the (0001) cleaved surface energy in silica (0.17eV/Å^2) [155], and the shear modulus and the theoretical shear strength (from Equation 4.10), we get an estimate of $\approx$ 80 Å. This is close to the strut size of 60 Å below which we see evidence of plasticity in our molecular dynamics simulations. Thus for t strut thickness values less than this value, the nano-honeycomb structures will exhibit plasticity.

4.7 Conclusions

The mechanics of diatom-inspired nanoporous silica structures under tensile loading has been investigated using molecular dynamics simulation and theoretical analysis. We find that the elastic modulus of the nanoporous structures is geometry dependent, and can be modified for a given porosity by changing the microstructure. Under elastic deformation, the load distribution in the structure is dependent on the slenderness ratio of the constituent struts. For thick struts ($l/t < 1.67$), the structure carries stress through a tension-shear-tension loading chain where the horizontal struts are under pure shear loading and the vertical struts under tensile load. For slender struts ($l/t > 1.67$), the structure passes load through a tension-bending-tension loading chain; the vertical struts are again under tensile load while the horizontal struts behave like beams with fixed ends under bending load.

The structure changes shape as it is loaded, with the pore shapes deforming. The pore shape change can be tracked by an angle change between adjoining struts, and it is shown that there exists a linear relation between the sine of this angle ϕ (Figure 4-7(a)), and the applied strain in the regime of elastic deformation.

On further loading, the structures either undergo plastic deformation followed by necking or brittle fracture starting by crack propagation from corners of the pores. There exists a minimum strut width size below which plasticity can be seen ($\approx 60-80$ Å), and this size is justified based on the flaw-tolerance concept for brittle materials failure. For structures with strut widths larger than this, fracture always proceeds by brittle crack initiation and propagation. For strut widths below this size, plasticity is seen in the form of shear deformation in the horizontal struts under shear loading. The yield strength of these plastically deforming structures has been calculated to depend on the structure geometry.

An important consideration for the mechanical response of nanoporous silica structures is the effect of presence of water, in particular for a more in-depth consideration of the properties of diatoms as they live in aqueous environments. Preliminary investigations by Garcia *et al.* [156] suggest that nanoporous silica structures (similar

to those found in this study) have reduced ductility and yield stress once the surface is hydrated. Similar results have been obtained in a previous study of silica nanorod deformation in the presence of water using semi-empirical quantum mechanics methods [157]. The authors concluded that strained siloxane (Si–O–Si) bonds are attacked by water which results in lower stress and lower failure strain of the silica nanorod, compared to a dry silica nanorod.

Our results establish a size-dependent brittle-to-ductile transition in nanoporous silica structures. Similar behavior has been observed experimentally in silica nanowires, where the size range for the transition is 20 nm. The aspect ratio and shape of pores can be modified to change the yield strength of these structures. The high values of stress for yielding or fracture lead to large enhanced ductility in these materials over bulk silica. The structures that show plastic yielding also show large toughness improvement over bulk silica. These results reveal that nano-scaling with control of porous geometry can lead to application of silica in carrying loads in small devices. The increased toughness, elastic ductility and plastic ductility arising from nano-scaling may also be fundamental in understanding the use of similar structures by nature in creating porous exoskeletons in diatoms.

Apart from the improved ductility, one property that is affected to a large extent is the material stiffness. Nanostructuring, as outlined in this chapter, can reduce the stiffness of the silica structures by up to 90% of its original value. Is it possible to design structures which recover the stiffness value of bulk silica while retaining the toughness improvement of the nanoporous silica? In the next chapter, we design hierarchical silica nanocomposites with 2 levels of hierarchy. We proceed by developing an mesoscale method for studying the mechanics of silica structures at the micron length scale. We then use the method in the analysis of the mechanics of hierarchical silica structures.

Chapter 5

Mesoscale Model of Deformation and Failure of Hierarchical Silica Nanocomposites

This chapter is focused on the development of a mesoscale model for studying the mechanics of hierarchical silica nanocomposite structures. Biomineralized silica-based materials, such as sea sponge exoskeletons, and diatoms, showcase the use of inferior constituent materials such as brittle ceramics like silica and soft protein to create materials that have surprisingly high toughness and resistance to crack propagation, and retain stiffness values close to the ceramic constituent (see Chapter 1). A common design paradigm seen in these materials is the existence of multiple levels of structural hierarchy [22, 29, 23, 28, 31]. Various studies have pointed at how the existence of these structural design levels and their functional adaptation helps the material in retaining the best possible combination of properties of the constituent materials [2, 158].

5.1 Review of structural bio-silica materials

A fascinating example of biomineralized structures are those of diatoms [140, 159, 160], a microscopic algae that feature cell walls, or frustules, mainly composed of

amorphous silica. A porous hierarchical structure dominates the landscape of the cell wall and encompasses intricate patterns that are highly varied and ordered, as shown in Figure 1-2, and reach all the way down to the nanoscale. Please see Chapter 1, section 1.2 and 1.3 for more details on the diatom structure and mechanical properties. Another silica-based design is found in the deep sea sponge (*Euplectella* sp.) skeleton (Figure 5-1). The structure shows structural design at several length scales, ranging from a composite consisting of consolidated nanometer sized silica spheres embedded in an organic matrix at the sub-micron scale (Figure 5-1(d)), through cylindrical lamellar silica-organic material composite at a micron length scale (called spicules-Figure 5-1(c)) to a square-lattice cage-like structure consisting of cylindrical rods (Figure 5-1(a-b)) at the macroscale.

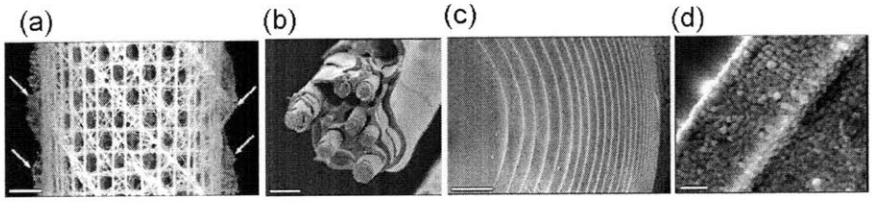

Figure 5-1: Structural hierarchies in a silica-based skeletal structures in a sea sponge. (a) shows the external cage structure of the silica-based skeletal system of *Euplectella* sp., scale bar 5 mm (b-d) show some of the underlying hierarchical structures with (b) showing fiber-composite structure in a constituent beam consisting of many spicules, scale bar 20 microns, (c) single spicule showing laminated silica-protein structure, scale bar 5 microns and (d) biosilica constituent of the silica layers revealing its consolidated nanoparticle nature, scale bar 500 nm. Figure reproduced from [28].

We summarize some key mechanical properties of diatoms and sea sponge ex-oskeletons here. Several studies reported in the recent literature have revealed the mechanical properties of diatom shells. Hamm *et al.* [39] used a glass needle to load and break diatom frustules in order to probe their mechanical response at failure, and found high strength and reversible elastic strains (e.g. 2.5% reversible strain in a frustule section). Other researchers [40] have used AFM nanoindentation to study the nanoscale material properties of the porous frustule layers of diatoms, identifying pore sizes on the order of several tens of nanometers at the smallest levels in the hierarchy, with ultra-thin silica walls on the order of several nanometers. They observed that the variation of mechanical properties between the hierarchical frustule layers could

be influenced by the pore size, pore distance, porosity, and under different biomineralization processes. Experimental tests to identify the mechanical properties of sea sponge spicules have also been reported. The spicules consisting of 97-98% volume fraction of silica and 2-3% of organic material, are seen to be tougher in both tension and bending than silica glass, by a factor of 6-7 times [161]. The thin organic layers present between silica layers in these spicules show delamination, crack-bridging, and provide elastic, viscoelastic and viscoplastic means for energy absorption under loading, leading to the high toughness [28, 161]. The fracture strength was also improved 3-5 times [162, 163], with large improvement in ductility over silica glass [163, 30].

We hypothesize that the nanoporous geometry and hierarchical arrangement of the frustules in diatoms, and the hierarchical structure of the spicules and their arrangement in sea sponge skeletons are crucial to providing enhanced toughness at high strength and stiffness even though the constituting material itself (that is, silica) is inherently brittle and mechanically inferior for structural applications. Previous work by the authors has focused on nanoporous structures of silica and shown that this geometry leads to high ductility and toughness [151, 164], although at the cost of structural stiffness. We thus explore here the creation of a multi-level hierarchical composite structures made of nanoporous silica and much stiffer bulk silica, and investigate their mechanical properties through an *in silico* approach.

The focus of the study reported in this article is first the development of an atomistically-informed mesoscale particle-spring model, which is then used for modeling these composite structures at the micro-scale [165]. The method is tested on the mechanics of randomly-dispersed fiber-reinforced composite structures made from bulk silica and nanoporous silica phases, to enable fracture studies at micrometer length-scales. An important question our model is expected to answer is whether or not it is possible to create a highly functional material with great strength and toughness out of a single material constituent, silica, by solely engineering its structural design at multiple levels without adding any additional material component.

5.2 Materials and Methods

A multiscale bottom-up computational methodology is used here to study the effect of hierarchical design on material properties and the mechanics of deformation. At the nanoscale we use molecular dynamics simulations to study the mechanics of the nanoporous silica structures. Molecular dynamics with the first principles based reactive ReaxFF atomistic force field is a powerful tool to capture fundamental nanoscale phenomena and the mechanisms behind them. At the micron length scale, we develop a mesoscale spring-lattice network model. The model is derived from as well as validated against the atomistic results. Spring-lattice network models at the micron length scales are able to capture elasticity, plasticity and fracture phenomena at these length scales. We describe the details of the methods in the following sections.

At the nanoscale, the first-principles derived ReaxFF force field [62] is used to characterize the mechanical behavior of nanoporous silica structures, as discussed in Chapter 4. Fully-atomistic simulations have been carried out for the mechanics of nanoporous silica structures [151, 164] (see Chapter 4). These studies show the effect of pore size, distribution and porosity on elastic modulus, plasticity, ductility and toughness of the structures. Figure 5-2(a) shows one of these characteristic nano-honeycomb silica structures. The availability of these studies allows us to extract constitutive laws of nanoporous silica behavior that can be used to build mesoscale models of silica structures with hierarchies.

5.2.1 Mesoscale method development and validation

Figure 5-2(b) shows the model setup consisting of a network of material particles connected in a lattice arrangement through springs. Such two-dimensional spring-lattice networks have been used previously to model deformation and fracture in brittle and quasi-brittle materials [166, 167, 168, 169], and are particularly suitable for studying fracture phenomena in heterogeneous materials [170, 171, 172]. The two-dimensional nature of the model resembles plane strain loading conditions. The constitutive stress-strain law under tensile load is obtained for a particular nano-

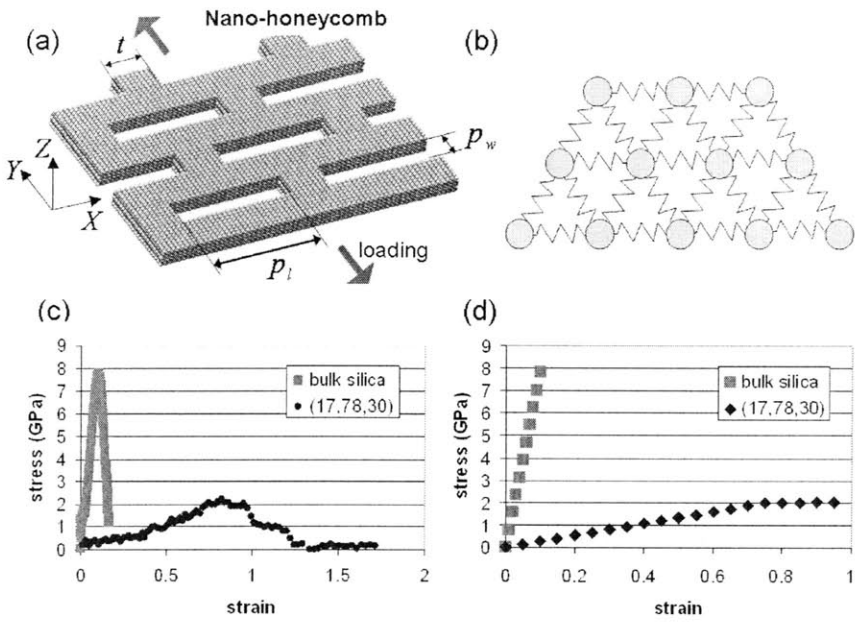

Figure 5-2: Atomistic and mesoscale modeling approaches are combined here to describe the material from the nano- to the micro-scale. Parameters for the mesoscale model are derived from constitutive behavior at the nanoscale obtained using atomistic simulations. Panel (a) shows the geometry of the nano-honeycomb used as building blocks for the composite structures, panel (b) shows a section of the triangular mesh mesoscale particle-spring model setup, panel (c) show stress-strain curves obtained from atomistic simulations of a nano-honeycomb structure, and for bulk silica with a crack of the same size as the pores in the nano-honeycomb. The legend defines the nano-honeycomb structure, which is shown as (t, p_l, p_w) parameters for the structure (numerical values given in Å). The bulk silica structure shows purely brittle fracture, the nano-honeycomb structure show ductile fracture. Panel (d) shows the behavior of the mesoscale triangular mesh lattice fitted to this constitutive behavior (the agreement with the full atomistic result depicted in panel (c) is evident and provides direct validation of the mesoscale model).

honeycomb silica and bulk silica using atomistic simulations, shown in Figure 5-2(c). In this figure, the bulk silica structure has a pre-crack with dimensions of the pore size in the nano-honeycomb structure, to compare structures with similar defect sizes.

As seen in Figure 5-2(c), the bulk structure is stiff and brittle, while the nanoporous structure is soft and ductile. The force-extension law for the mesoscale inter-particle potential is hyperelastic and is fit to the constitutive law behavior of nano-silica and bulk silica under tensile load (Figure 5-2(d)). The hyperelastic spring potential models the atomistic results for the nano-honeycomb as elastic-perfectly plastic behavior, and the bulk silica as elastic-brittle behavior. For the nano-honeycomb, the flow stress

is obtained from atomistic simulations, and is calculated as the mean stress during plastic deformation. Since the aim of this study is to obtain mechanics of different composite structures, the properties of the local springs in the lattice in a certain material model are changed according to whether they lie geometrically inside the matrix or reinforcing phase.

The brittle bulk silica phase inter-particle potential is modeled as follows:

$$F_A\left(\Delta L_A\right) = \begin{cases} k_A \Delta L_A & \text{if } \Delta L_A < \Delta L_{A,c}, \\ 0 & \text{if } \Delta L_A > \Delta L_{A,c}, \end{cases} \tag{5.1}$$

where F_A is the force on a spring between two material particles of the brittle phase, k_A is the force constant for the spring, ΔL_A is the extension in the spring, and $\Delta L_{A,c}$ is the critical cutoff distance for the spring. The cutoff distance $\Delta L_{A,c}$, beyond which the mesoscale spring carries zero load, is fixed based on the failure strain, and the force constant k_A is fit to the elastic modulus of the material obtained from atomistic simulations.

The ductile nano-porous phase inter-particle potential is modeled as:

$$F_B\left(\Delta L\right) = \begin{cases} k_B \Delta L_B & \text{if } \Delta L_B < \Delta L_{B,1}\ , \\ k_B \Delta L_{B,1} + k_C\left(\Delta L_B - \Delta L_{B,1}\right) & \text{if } \Delta L_{B,1} < \Delta L_B < \Delta L_{B,c}\ , \\ 0 & \text{if } \Delta L_B > \Delta L_{B,c}\ , \end{cases} \tag{5.2}$$

where F_B is the force on a spring between two material particles of the ductile phase, ΔL_B is the extension in the spring, and $\Delta L_{B,1}$ is the extension for the spring for the onset of the plastic regime, and $\Delta L_{B,c}$ is the critical cutoff extension when the spring breaks and stops carrying load, k_B is the force constant for the elastic response, and $k_C = k_B/100$ is a small force constant to model plastic deformation at constant flow stress. $\Delta L_{B,1}$ is fit to the yield strain, and $\Delta L_{B,c}$ is fit to the failure strain, and k_B is fit to the elastic modulus for the nano-honeycomb structure obtained from the atomistic simulations (Figure 5-2(c)).

The mesoscale model uses a triangular lattice regular mesh for the arrangement

of the springs. This results in isotropic elasticity behavior which can be assumed if the underlying structure is polycrystalline with regular arrangement of grains. Anisotropic behavior could also be introduced in the mesoscale model in principle, but for the proof-of-concept study targeted in this study (in the spirit of simple computational experiments), we assume isotropic behavior in the underlying atomistic structure. The implications of this assumption are that crystal-orientation dependent anisotropic elastic and fracture behavior phenomena will not be captured through this model. The interfaces between the two phases in the composite, if the crystal structure is not continuous across the interface, would also possibly contribute to plasticity in the material through slip and friction, however the interfaces have been just assigned the low strength and stiffness values of the nanoporous phase in the model. This doesn't allow the model to capture any toughness enhancement by interfacial plasticity mechanisms.

Bulk two-dimensional mesoscale models are constructed of bulk silica and nanoporous silica and subject to tensile testing. Comparison of the elastic moduli and fracture toughness between the atomistic simulations and mesoscale simulations are used to fix spring constants and inter-particle distance in the mesoscale model.

The elastic modulus and fracture toughness for the atomistic model are calculated for a bulk silica sample with a center-crack. The fracture toughness using the ReaxFF force field for silica is calculated to be 0.79 MPa$\sqrt{\text{m}}$. This is rather close to experimental values in the literature for fused quartz, 0.6-0.75 MPa$\sqrt{\text{m}}$ [173, 174]. The elastic modulus for the spring-lattice model is fit to 102.3 GPa and the mode I fracture toughness to be 0.79 MPa$\sqrt{\text{m}}$.

To match the atomistic simulation values (see brief review above), an inter-particle distance of 78 nm and spring constants of 3,932 N/m and 134.4 N/m for the brittle and ductile phases, respectively, are chosen for a through thickness of 100 nm. This ensures for a separation of scales between the scales described by the atomistic model and the characteristic length-scale associated with the mesoscale model (the typical scales of the atomistic-level models is up to ten nanometers). All mesoscale models are implemented within the LAMMPS software package [175].

It is noted here that the model parameters can easily be adapted to describe other nanostructures, and can even be extended to describe multiple nanostructures in the study of hierarchical systems. The specific model considered here represents one specific case study explored here.

5.2.2 Fracture property characterization

For materials that show failure by growth of a single dominant crack, we characterize them by calculating their fracture toughness. The toughness is calculated by calculating the energy release rate by invoking the J-integral [176, 177] in its domain form [178] around the crack tip, given by:

$$J = \int_{S_0} \sum_{i,j}^{2} \left[\left(W \delta_{2j} - P_{ij} \frac{\partial u_i}{\partial X_2} \right) \frac{\partial q}{\partial X_j} \right] dS, \tag{5.3}$$

where W is the strain energy density, P_{ij} is the first Piola-Kirchoff stress tensor, u_i represents the displacement field, X are the material coordinates, S_0 represents the undeformed area of the domain, δ is the Kronecker delta, and

$$q = \begin{cases} 0: & r = r_1, \\ 1: & r = r_2, \\ (r - r_1)/(r_2 - r_1): & r_1 < r < r_2, \end{cases} \tag{5.4}$$

where the parameters r_1 and r_2 are shown in Figure 5-9(a). The discrete form of this equation, for small displacements, is given by (see, e.g. [179, 180]):

$$J = \sum_{\alpha \in S_0} \sum_{i,j}^{2} \left[\left(W^{\alpha} \delta_{2j} - P_{ij}^{\alpha} \frac{\partial u_i}{\partial X_2} \right) \frac{\partial q(X_\alpha)}{\partial X_j} \right] S_0^{\alpha}, \tag{5.5}$$

where S_0^{α} is the initial undeformed area occupied by the material particle α, X_α is the initial position of material particle α, W^{α} is the local strain energy density at any material particle α which is calculated as follows,

$$W^{\alpha} = \frac{1}{S^{\alpha}} \left(\phi^{\alpha}(\varepsilon_{ij}) - \phi^{\alpha}(0) \right), \tag{5.6}$$

where ϕ^α is the potential strain energy of the material particle α, obtained from simulation by splitting the spring potential energy between material particles sharing the spring bond, and the stress at the atom α, $\left(P_{ij}^\alpha\right)$ is calculated from the virial theorem [181]:

$$\mathrm{P}^\alpha = \frac{1}{2\Omega_\alpha} \sum_{\beta \neq \alpha} \mathrm{r}^{\alpha\beta} \otimes \mathrm{f}^{\alpha\beta}, \tag{5.7}$$

where $\mathrm{r}^{\alpha\beta}$ is a vector joining material particles α and β, $\mathrm{f}^{\alpha\beta}$ is the force applied on material particle α by material particle β, and $\Omega_\alpha = S^\alpha t$ is the volume occupied by material particle α, where S^α is the area occupied by the material particle α in the deformed configuration. This formulation of the J-integral is used to avoid involving high stress values at the crack tip region in the calculation, and the convergence of the J-integral is checked by measuring its value against different integration domain regions. The strain ε_{ij}^α, and $\partial u_i / \partial X_1$ are obtained by a local least square fit to the neighbor displacement field at each material particle location.

5.2.3 R-curve calculation

Stable crack advance for every load configuration is noted by finding the crack tip location. A particular spring bond is regarded as broken when its deformation exceeds the cutoff for the interaction. Crack surfaces are visualized by finding all spring bonds which have snapped for a given load. The J-integral is used to find the energy release rate for a given amount of stable crack advance. Plot of the J-integral from the start of crack initiation through crack propagation provides the R-curve [182] for the material, *i.e.* how its fracture toughness changes as a function of stable crack advance.

5.3 Results and discussion

We consider models of randomly-distributed fiber-reinforced composites of bulk silica with small volume fractions of nanoporous silica. Figure 5-3 shows the different geometries considered here. In all cases, the fibers are circular in cross-section and

randomly distributed through the matrix, oriented parallel out-of-plane (in the Z direction in Figure 5-3) and loaded in the cross-section (X-Y plane). Fiber diameters are 1.3 µm in a model size of 27 µm by 23.3 µm and 100 nm out-of-plane. Two kinds of composites are designed– a), hard-fibers of bulk silica (of volume fraction 76%) embedded in a soft nanoporous matrix, and b), soft fibers of nanoporous silica dispersed in a hard silica matrix (of volume fraction 86%). The two designs are shown in Figure 5-3. We select five different random structures for both morphologies as representative bulk-silica rich composites to obtain statistically relevant data, and will refer to them henceforth as the brittle-fiber and brittle-matrix structures, respectively.

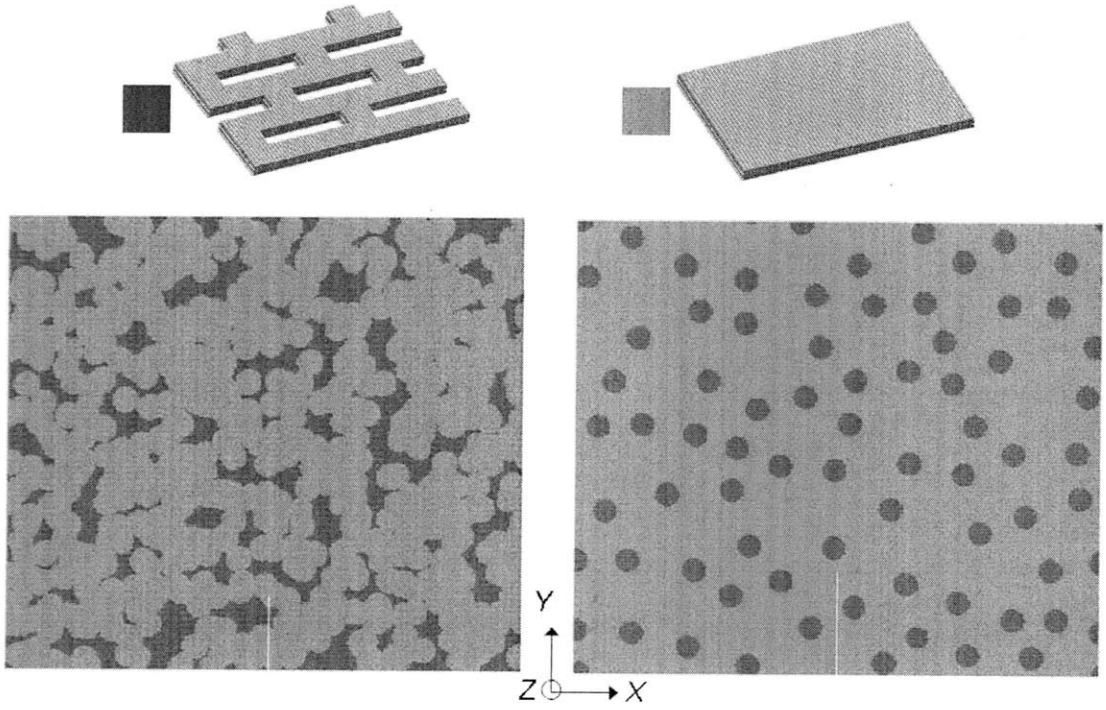

Figure 5-3: Geometry of randomly distributed fiber-composite structures at the mesoscale. Constituents are, bulk silica (in grey/light, with a high volume fraction) and nano-honeycomb structures (in blue/dark, small volume fraction). Design conditions that enhance toughness of bulk silica by distribution of small amount of nano-honeycomb silica are being investigated here. The structure on the left shows bulk silica fibers as reinforcement, whereas the right structure shows nano-honeycomb silica fibers as the reinforcing phase. The structure sizes are 27 µm by 23.3 µm and 100 nm out-of-plane. Reinforcing phase is always in fiber form of diameter 1.3 µm, aligned parallel out-of-plane but randomly distributed in-plane. Structures of both types are studied for crack propagation response under mode I loading with plane strain conditions. Initial pre-crack sizes range from 3.9 to 5.4 µm.).

We now present a systematic study of the effect of composition and material distribution on the elasticity, plasticity and fracture of these composites. Figure 5-4 shows the elastic modulus measurements for both the brittle-fiber and brittle-matrix materials. We observe that for a random dispersion of the second phase in the first, the elastic modulus lies between the Reuss and Voigt bounds. However, the brittle-matrix composite is seen to have a modulus closer to the upper bound (Voigt) than the brittle-fiber composite. Thus brittle-matrix morphologies are more suitable for obtaining a higher stiffness for random fiber distributions.

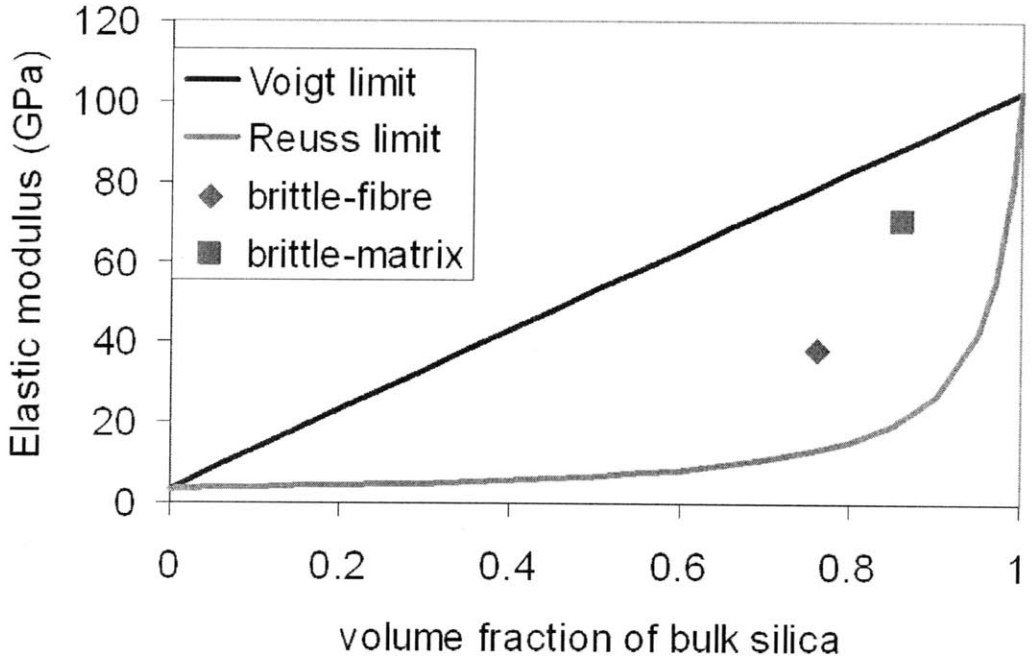

Figure 5-4: Elastic modulus for the brittle-fiber and brittle-matrix composites plotted as a function of volume fraction of the brittle phase. The limits at 0 and 1 volume fraction correspond to nano-honeycomb silica (soft) and bulk silica (stiff) respectively. The composite moduli are seen to lie within the Reuss and Voigt bounds of load sharing between the phases, the brittle-matrix morphology providing stiffness closer to the upper limit (of Voigt modulus).

Next we create sharp edge cracks in all materials and load them under quasi-static mode I loading. Loading is carried out by stepped edge displacement boundary conditions and relaxing the global positions of all material particles using a conjugate gradient energy minimization scheme [183]. Initial crack size is 3.9-5.4 μm. Crack initiation is identified by the advance of the crack front at a particular loading strain

value. Plastic deformation is visualized by calculating local strains in springs and comparing to yield strain values. We notice the absence of any plasticity prior to crack propagation initiation in all the composite designs. Figure 5-5 shows representative overall stress-strain response for composite structures with brittle-fiber and brittle-matrix morphologies, with and without the presence of the edge crack.

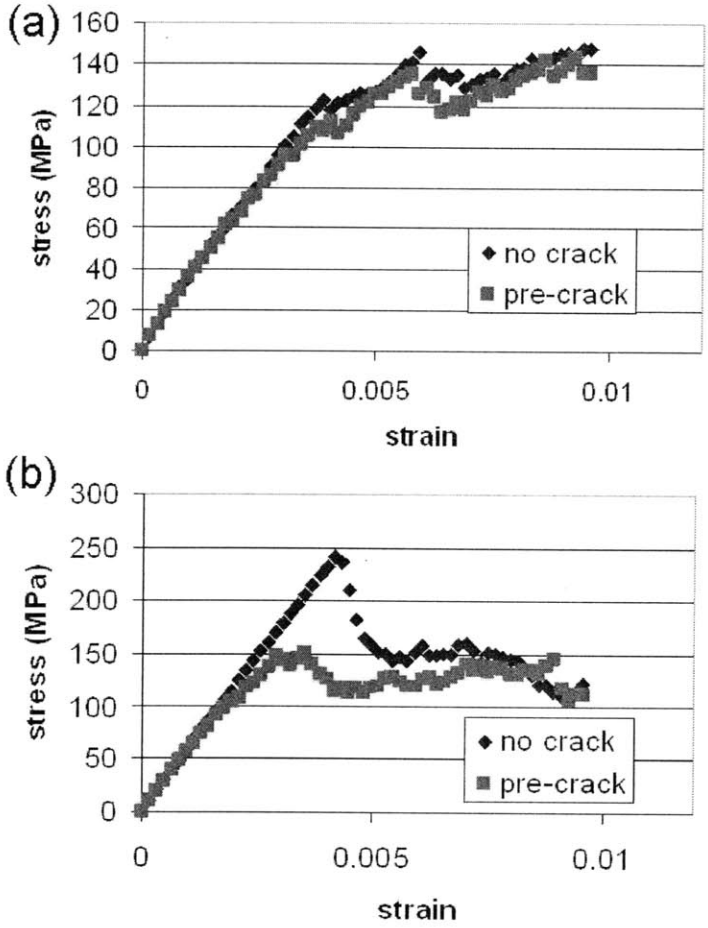

Figure 5-5: Stress-strain curves for (a) composite structures with bulk-silica as the reinforcement, with and without presence of a pre-crack. The near-identical response shows the flaw-tolerance behavior for these structures to pre-cracks of the given size. The structures show multiple cracking throughout the material, and this is reflected in the stress-strain curve as a gradual loss of stiffness of the material as the number and size of the multiple cracks grow. (b) Stress-strain curves for composite structures with nano-honeycomb silica as the reinforcement, with and without presence of a pre-crack. The varying fracture strengths clearly show an effect of the crack size. All structures fail by the growth of a single dominant crack.

The brittle-fiber structures show multiple micro-cracking sites (throughout the

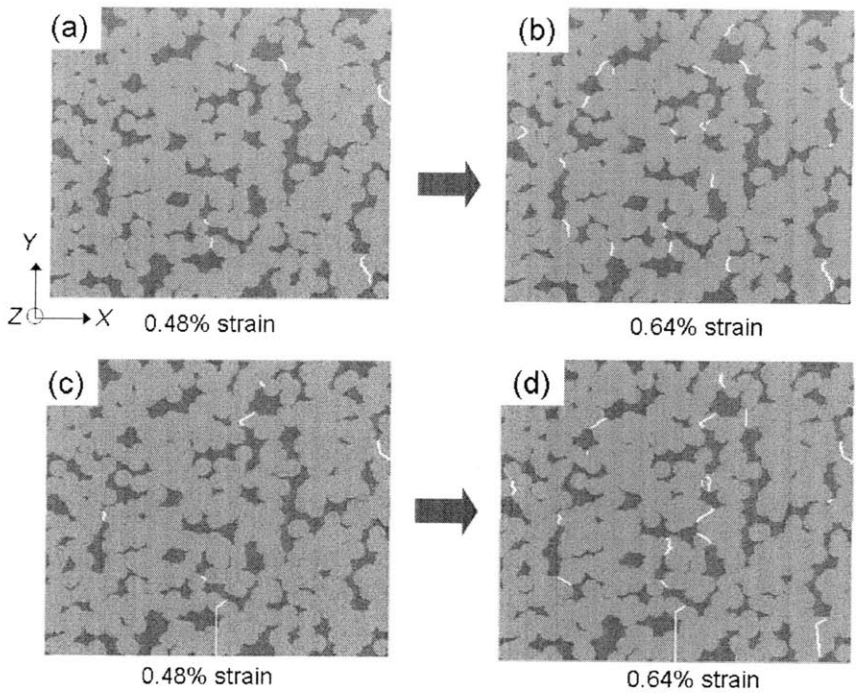

Figure 5-6: Crack pathways for composite structures with nano-honeycomb structure as the matrix and brittle silica as the reinforcing fiber phase. The volume fraction of silica phase is 76%. (a) and (b) show fracture progress starting from a material with no pre-crack; (c) and (d) show fracture progress in the same material with a pre-crack present. In these cases we observe that the pre-crack propagates for a small distance but does not propagate through the sample, and other smaller cracks are initiated throughout the sample. These multiple small cracks determine the stress-strain response of the structure. The structure is thus flaw-tolerant to pre-cracks of these sizes, and the fracture stress and behavior are almost independent of the size of the pre-crack. This is reflected also in the stress-strain curve for the stress-strain response of the undefected, and cracked structures (shown in Figure 5-5a). The fracture toughness cannot be measured for these structures and crack sizes.

sample) under tensile load. The presence of pre-cracks is not seen to affect this phenomenon, and the material fails by the growth and coalescence of several micro-cracks (Figure 5-6). This phenomenon is also captured by the absence of any effect on the stress-strain curve to the presence of pre-cracks of a certain size and below (Figure 5-6(a)), and can be classified as a defect-tolerant state. Fracture mechanics formulations cannot be used for such material microstructures and crack sizes, and damage mechanics which deals with evolution of damage with applied load—for example in the form of diffuse micro-cracking—would have to be used to characterize the failure response. The diffuse cracking also leads to an effect on the elastic modulus (slope

of the stress-strain curve) of the material, as seen in Figure 5-6(a), the modulus is lowered at higher strain values when the microcracks start to increase in size and number.

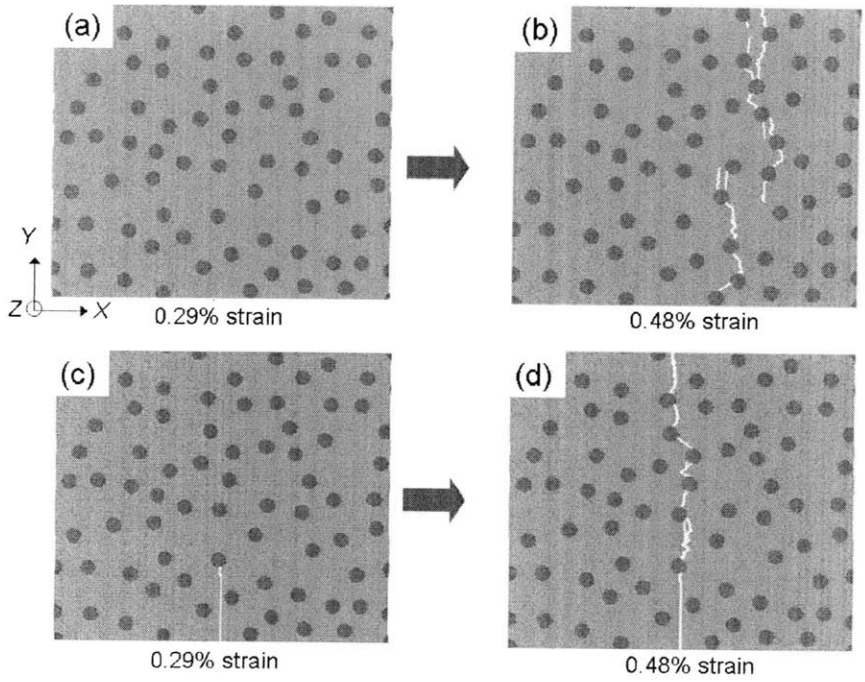

Figure 5-7: Crack pathways for composite structures with brittle silica as the matrix and nano-honeycomb structure as the reinforcing fiber phase. The volume fraction of bulk silica phase is 86%. (a) and (b) show fracture progress starting from a no pre-crack material; (c) and (d) show fracture progress from the same material with a pre-crack. In both cases we observe that fracture occurs through the propagation of a dominant crack. (a) and (c) show the un-cracked and pre-cracked specimens at the same load, the un-cracked specimen is intact, whereas the pre-crack has started propagating in the other specimen. Since the fracture strength of a structure with a dominant propagating crack is pre-crack-size dependent (according to fracture mechanics), the stress-strain curve for the stress-strain response of the undefected, and cracked structures are markedly different (shown in Figure 5-5b). Fracture toughness can be measured for these structures, as the energy required for the growth of the pre-crack per unit crack advance

The brittle-matrix structures, on the other hand, show failure by growth of a single dominant crack (Figure 5-7). This phenomenon is captured in the stress-strain curve by the decrease in fracture stress with increase in pre-crack size (Figure 5-5(b)), as expected from fracture mechanics. Snapshots of the pre-crack growth are shown in Figure 5-8 for all the brittle-matrix composite structures considered. The crack path shows several phenomena, such as linking fibers lying in its path, and

following a tortuous pathway. In some cases, we see crack branching at a fiber-matrix interface and in one case (Figure 5-8(b)) the crack is not continuous but is bridged by a ligament of the matrix. These highlight all the different mechanisms at this length scale that can affect the fracture behavior of the material.

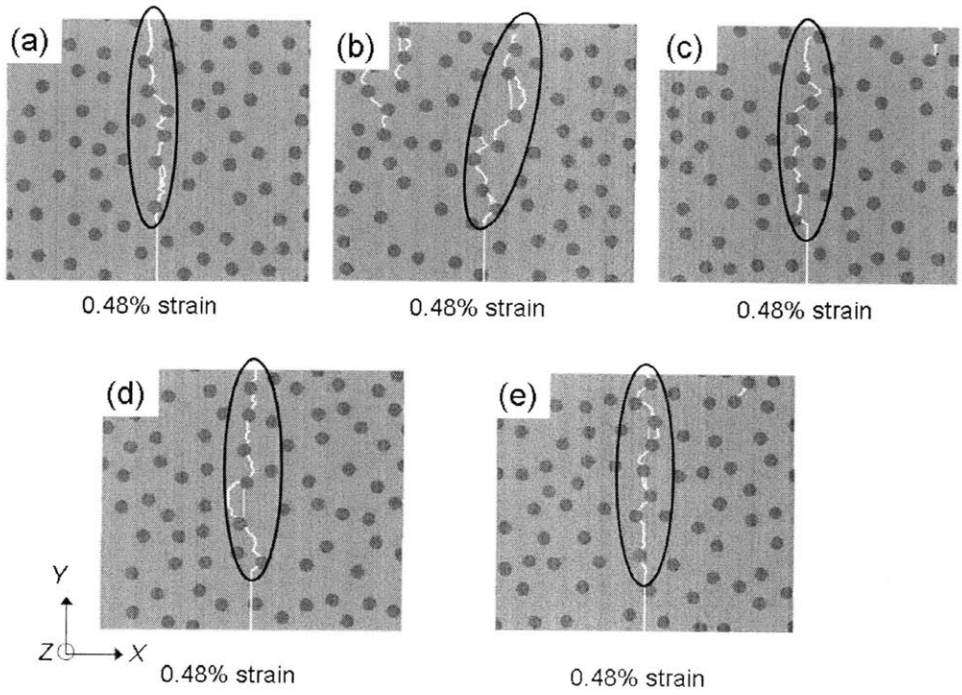

Figure 5-8: Different composite structures with brittle bulk-silica as the matrix (volume fraction 86%) and ductile nano-honeycomb structures as the reinforcing fiber phase showing fracture toughness improvement mechanisms. The fibers have circular cross-section and are randomly distributed and five different random structures are shown here. A single pre-crack is introduced and then subjected to mode I loading. Propagation of the single dominant crack is seen on loading, and the propagation path is marked in white. All structures show that the crack path is not straight, but connects reinforcing fibers lying close to the original crack plane. Crack deflection and bridging by reinforcing fibers behind the crack tip are the mechanisms seen to increase toughness here.

The fracture toughness is calculated for the brittle-matrix composite structures using the J-integral formulation (Figure 5-9(a)). Crack initiation toughness is measured by a J-integral calculation of the strain energy release rate just prior to crack propagation. R-curve measurements (crack advance resistance as a function of stable crack growth) are then undertaken by obtaining stable crack propagation distances for different load strains and repeating the J-integral calculations. We thus obtain the fracture toughness as a function of crack advance distance. We notice all struc-

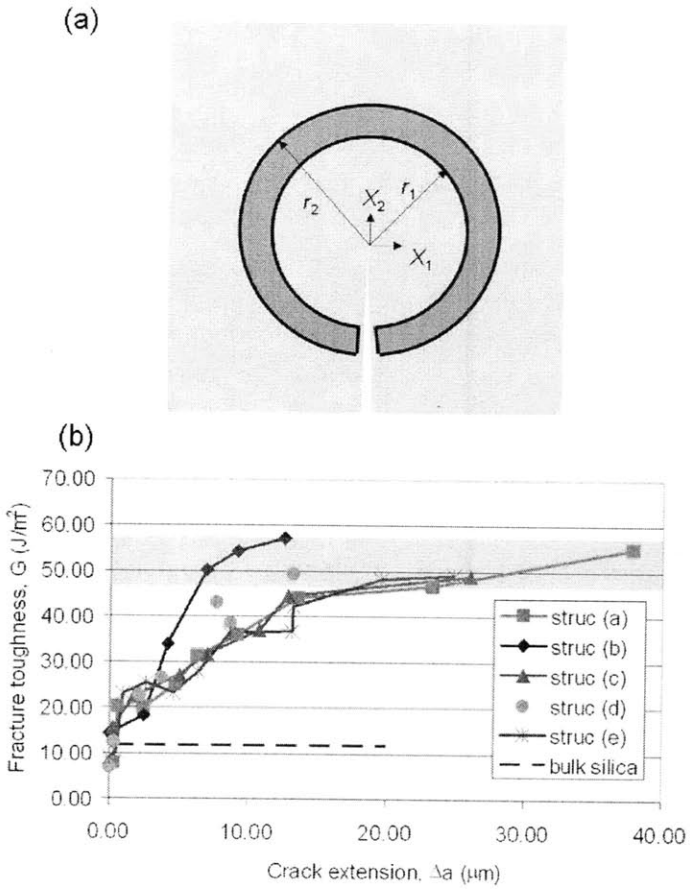

Figure 5-9: Calculation of the J-integral and R-curves. (a) shows the J-integral calculation for a stationary crack by the use of a domain-integral around the crack. The J-integral provides the value of the energy release rate per unit advance of the crack into the crack tip, or the resistance to crack propagation. The red/dark region shown is the domain of integration and the convergence of the J-integral is tested by taking different and regions for the same crack and specimen configuration.(b) shows fracture toughness measures as a function of crack advance (R-curve behavior) for all the structures in Figure 5-8. The toughness of bulk silica is also shown as a dotted curve.

tures show an initiation toughness close to bulk silica and significant improvement in toughness ($\approx$ 4.4 times) as the crack proceeds (Figure 5-9(b)). The improvement in toughness arises from crack-deflection and crack-bridging by the reinforcing phase, and also ligament-bridging by the matrix. Simultaneously, the stiffness is not compromised due to the large volume fraction of the bulk silica phase (Figure 5-4). Steady-state fracture propagation toughness values can be obtained from the R-curve for the composite for large crack growths in the range of several microns.

5.4 Summary and Conclusions

We established here a hierarchical mesoscale modeling scheme that represents the mechanics of silica-nanoporous silica composites at the micron length scale, bridging scales from a few nanometer (accessible to full-atomistic modeling) to scales of tens of micrometers. The particle-spring mesoscale model has parameters fitted to atomistic simulations using the ReaxFF force field. The ReaxFF force field itself has parameters fitted to first-principles quantum simulations of energetics of silicon-oxygen clusters. We establish the validity of the mesoscale model by capturing the stress-strain relation of the bulk silica and nanoporous silica, and the fracture toughness and fracture mechanisms (e.g. crack bridging, spreading, etc.) of silica in different hierarchical designs.

Enabled by the mesoscale model, we studied the fracture mechanics of randomly-dispersed fiber composite structures using this coarse-grained model. ReaxFF simulations have shown us previously that the design of nanoporous silica leads to enhanced ductility and toughness at the cost of compromising stiffness. We demonstrated that through using composites with a large volume fraction of the bulk silica, it is possible to obtain structures with stiffness almost as large as the silica phase, but significant toughness improvement due to the use of nanoporous materials as the other phase. To this end, we completed a case study of fracture of two kinds of composites, one characterized by hard fibers of bulk silica embedded in a soft nanoporous matrix (brittle-fiber), and another one that consists of soft fibers of nanoporous silica dispersed in a hard silica matrix (brittle-matrix).

The brittle-fiber structures showed multiple micro-cracking initiation under tensile load, and the material fails by their growth and coalescence, independent of presence of pre-cracks in the material (Figure 5-6). Fracture mechanics formulations cannot be used for such material microstructures and crack sizes, and damage mechanics which deals with evolution of damage with applied load e.g. in the form of diffuse micro-cracking, have to be used to characterize the failure response in this flaw-tolerant regime of cracking.

The brittle-matrix structures, on the other hand, showed failure by growth of a single dominant crack (Figure 5-7). The fracture toughness was calculated for several randomly dispersed fiber-composite structures using the J-integral formulation. The crack toughness is tracked as a function of crack advance, using an R-curve (Figure 5-9(b)), and we observed that all structures show an initiation toughness close to bulk silica and significant improvement in toughness as the crack proceeds, similar to findings reported earlier for bone [184]. The improvement in toughness arises from crack-deflection and crack-bridging by the reinforcing phase, and ligament bridging by unbroken matrix. At the same time, the stiffness of the composite structure lies close to its Voigt upper limit (Figure 5-4). To the best of our knowledge, this type of R-curve analysis is reported in this article for the first time for hierarchical silica structures, and implemented in a multiscale simulation scheme of these structures. We note that our model is simple and has several limitations, such as the lack of describing anisotropies, and its two-dimensional nature. Nevertheless, it provides a useful tool for computational experiments geared to elucidate fundamental design principles of biological materials at multiple length-scales, and the formulation presented here can be easily adapted to other cases.

The improvement in toughness and retaining of stiffness of bulk silica by designing small regions of nanoporous geometry in the bulk phase point to a design methodology for obtaining stiff and tough materials out of an inherently brittle material (silica) to begin with (Figure 5-10). The design philosophy can be summed up as the use of a single material – silica – which is traditionally considered an undesirable (mechanically inferior) structural material due to its brittleness, arranged in a hierarchical pattern with substructures that go down to the nanoscale dimensions. A future refinement in this model would be modeling mechanical response of interfaces between the phases in the composite using atomistic simulations and incorporating interfacial parameters in the mesoscale model. Further work, shown in Chapter 6, aims at studying effect of additional levels of hierarchies on these properties. The present design scheme suggested enables us to obtain highly functional materials that feature enhanced toughness and stiffness. The utilization of the design paradigm

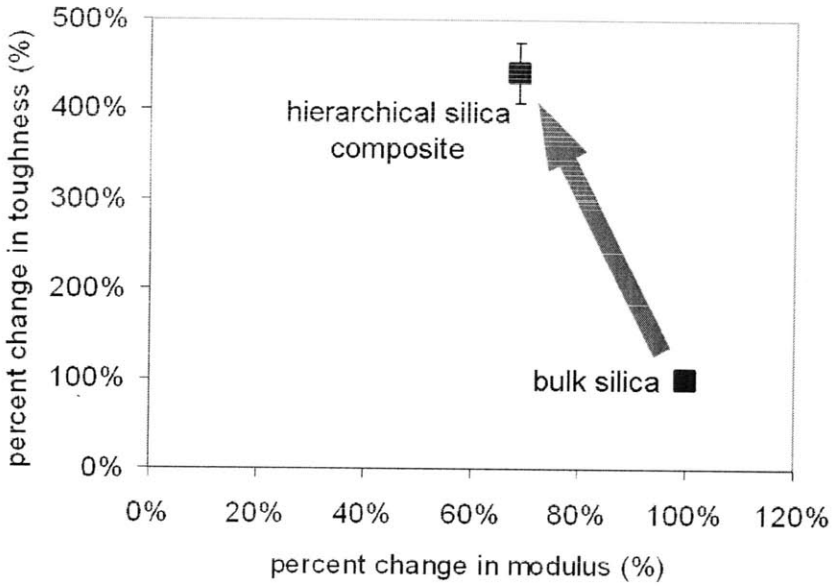

Figure 5-10: The design of the hierarchical silica composite improves the toughness of bulk silica significantly ($\approx$ 4.4 times) while compromising on the stiffness only slightly ($\approx$ 70 % of bulk). This points towards the use of hierarchies along with a single design material to improve undesirable mechanical properties significantly (here low toughness) while not compromising on the desirable ones (here high stiffness).

outlined here leads to a substantial increase the design space for brittle materials, without the need to add additional materials, and solely by geometrical design.

Likely driven by evolutionary pressures, materials in living systems already use this design philosophy in a variety of protective armor and internal load-carrying structures in many different species through the use of hierarchies (as it was shown for soft protein materials in earlier studies [185]), and our simulations point to the strength of using this philosophy for designing engineering structures made out of hard materials as well. The exploitation of this method for *de novo* material design could be substantial, as it provides a pathway to utilize nanoscale material elements with superior properties for macroscale highly functional materials—with superior properties, despite the utilization of simple and abundant building blocks such as silica. In the next Chapter, we extend the use of the mesoscale model developed here, to the study of fracture properties and toughness of hierarchical materials with multiple levels of hierarchy. Our attempt is to observe numerically, how the addition

of more levels of hierarchy improves toughness properties.

Chapter 6

The role of multiple structural hierarchy levels in defect tolerance and toughness

This chapter extends the use of the mesoscale model developed in Chapter 5 to the direct simulation of the fracture properties of structures with several levels of hierarchy. This is motivated by the observation that many biological structural materials show not just 2 or 3, but several levels of structural hierarchies from the nanoscale up to the macroscale. Cortical bone, for example has 7 distinct structural hierarchy levels [1, 186], using two basic constituents of collagen protein and hydroxyapatite mineral. Sea sponge exoskeletons, made of silica and protein, show 6 levels of structural hierarchy [28]. A question that arises is how does the increase in number of hierarchy levels impact mechanical properties? Does it give rise to properties that are not apparent from 1 or 2 levels of hierarchy? Here, we will specifically focus on the affect of adding more hierarchical levels on crack advance and toughness.

6.1 Background on structures with multiple levels of structural hierarchy and study of their mechanics

In biological structural materials possessing multiple levels of structural hierarchies, many phenomena and properties are linked across structural scales (see Chapter 1, section 1.3). Experimentally, fracture behavior of these materials, such as bone and nacre have been shown to be heavily linked across scales [35, 30], with mechanisms at several different hierarchy levels participating in the overall behavior. This has also led to some contention as to which mechanisms are the important ones [184, 33].

The field of computational and theoretical studies of mechanics of materials with a large number of hierarchical levels is in its infancy. A major problem in the field is the issue of studying deformation mechanisms and their interactions across a huge range of length scales, which are often beyond the computational capabilities of a single computational technique such as atomistic simulation or finite-element methods. Another challenge is that a representative volume element cannot be found at any length-scale without accounting for its entire sub-structure down to the nanoscale, because of the heterogeneity of the design at any length-scale. This heterogeneity can potentially lead to very large models in terms of computational cost, beyond the reach of today's computational resources. Multi-scale methods (as described in Chapter 2) have to be applied in these cases. Nonetheless, concurrent multi-scale methods cannot be applied easily due to the non-applicability of localized deformation; and hierarchical multi-scale methods, tend to develop into too coarse a description at very large length scales, due to the loss of detailed information about mechanisms with every additional level of coarse-graining.

One recent approach has been the study of self-similar hierarchical assemblies with some assumptions about similarity in failure mechanisms at each hierarchy level [22, 36, 187, 188]. These continuum models predict strength, stiffness and toughness scaling with number of hierarchy levels for a number of simple, self-similar assemblies

e.g. for self-similar hierarchical assembly of bone nanostructure [36] or gecko adhesion [189, 190]. A key drawback of these models is the use of a self-similar geometry assumption, and also the assumption of correspondence of energy dissipation mechanisms and failure mechanisms across hierarchies. Self-similarity in geometric design is not seen in many biological materials, such as bone, nacre, sea sponge exoskeleton, diatoms etc. [186, 158, 28, 27], where the structural arrangement at each hierarchy level is very different. Another approach has been of taking into account explicit probabilistic modes of failure pathways down several levels of hierarchy, assuming certain possible unit failure events (e.g. failure of unit hydrogen bonds in hierarchical alpha-helix structures, and their combinatorial arrangements) [191, 192]. Some qualitative models have also been derived to identify design similarities in the hierarchies of various biological materials that may offer the key to improvements of properties [13, 31, 193].

In this work, our aim is to study the effects of hierarchical arrangements on toughness. Toughness in materials is often measured through fracture toughness, which focuses on energy dissipated in the structure per unit length advance of a major crack that eventually leads to complete failure of the structure. However, as demonstrated in the last chapter, complex microstructures can have very different failure mechanisms than the propagation of a single large crack, e.g. through diffuse damage in the form of several cracks interacting throughout the structure. We aim to study how toughness is enhanced through hierarchies, specifically given that, through the fracture mechanics viewpoint, the crack will have to interact with all different levels of hierarchy. Specifically, our goal is to observe whether each additional level of structural hierarchy effect has a substantial effect on toughness.

We will also study a related property, the defect-tolerance length scale. Defect tolerance measures the sensitivity of fracture strength to the presence and size of a crack. A higher defect-tolerance implies a lower sensitivity to crack size, *i.e.*, a large change in the size of a crack present in the material/structure is required, for a small change in the fracture strength. One of the aims of robust design is the increase of the defect-tolerance length scale, so that the material/structure strength does not vary

for a range of flaw size distribution. This can be related to the parameter insensitivity definition of robustness in biological systems theory [25] (see Chapter 1, section 1.2). Through the use of flaw-tolerant design at the nanoscale in brittle materials [33], and suppressing dislocation-mediated plasticity in ductile materials [129], it is possible to eliminate any dependence of fracture strength on crack size for very small nanometer-sized crystals. Here, however, we also want to study the effect of hierarchies on this sensitivity of fracture strength on crack size.

With this aim, we use the bulk-silica/nanoporous silica model developed in Chapters 4 and 5. We focus on the use of silica as a 'poor' structural material, and attempt to engineer it to possess better properties, through nanostructuring (Chapter 4) and use of hierarchies (Chapter 5 and here). In this chapter, the atomistically-informed mesoscale method developed in Chapter 5, is thus extended to several levels of hierarchy.

6.2 Mesoscale simulation results

In many biological materials possessing several hierarchy levels, the design substructure at each level is periodic and built from an repeating template. Examples include cortical bone, nacre at all their hierarchy levels (see Chapter 1, section 1.2); diatoms and sea-sponge skeletons at all hierarchy levels except the nanoscale biosilica, which is a randomly-dispersed composite (see Figures 1-2 and 5-1).

6.2.1 Two-hierarchy level structures with periodic geometry

We extend the mesoscale designs of Chapter 5, to regularly distributed (periodic) composite structures. The protein constituent found in biological structures, which is soft and tough is replaced by nanoporous silica in our structures; the mineral constituent, which is hard and brittle is replaced by bulk silica. For a particle-reinforced composite, there are two distinct design schemes possible, one in which the soft material is the matrix, the other where it is the reinforcement particles. We thus choose two representative systems, one in which the soft/tough material is the

continuous phase, with the hard/brittle material dispersed in platelet form within the matrix, mimicking the periodic arrangement observed in several hierarchy levels in bone and nacre [1]. The second representative system is where the hard/brittle constituent is the continuous phase, with regions of soft/tough material embedded within the hard matrix. These structures are found in biocrystals, where protein material is encapsulated in a hard crystal, such as biological calcite single crystals [194, 195]. The use of a periodic distribution of one material in another not only allows us to capture actual design morphologies observed in biological structures, but also removes the stochastic element of the dependence of mechanical properties on random morphologies.

These regularly distributed composite structures are shown in Figure 6-1. The volume fraction of the stiff silica phase is kept at a high value and constant at 80%. For the bone-like arrangement, the platelets of bulk silica have a rectangular shaped cross-section and 8.4 μm by 2.4 μm in size in the X-Y plane, and 100 nm in the out-of-plane direction. They are arranged in a staggered fashion, with an overlap equal to half their length across subsequent layers. The overall structure size is 27 μm by 70 μm and 100 nm out-of-plane. For the biocalcite-like arrangement, the soft nanoporous silica is embedded as rectangular inclusions with a cross-section size of 8.7 μm by 0.7 μm in size in the X-Y plane, and 100 nm in the out-of-plane Z-direction.

Next we create sharp edge cracks in all structures and load them under quasi-static mode I loading. Loading is carried out by stepped edge displacement boundary conditions and relaxing the global positions of all material particles using a conjugate gradient energy minimization scheme [183]. Initial crack sizes range from 5–20 μm. Crack initiation is identified by the advance of the crack front at a particular applied strain. Figure 6-2 shows representative overall stress-strain response for composite structures with bone-like and biocalcite-like morphologies, with and without the presence of the edge crack. The data shows that both structures have a drop in fracture stress in the presence of a crack. The bone-like structure has a higher fracture stress but shows a larger drop in strength when a crack is introduced, whereas the biocalcite-like structure has smaller fracture strength, but also a lower sensitivity to the presence

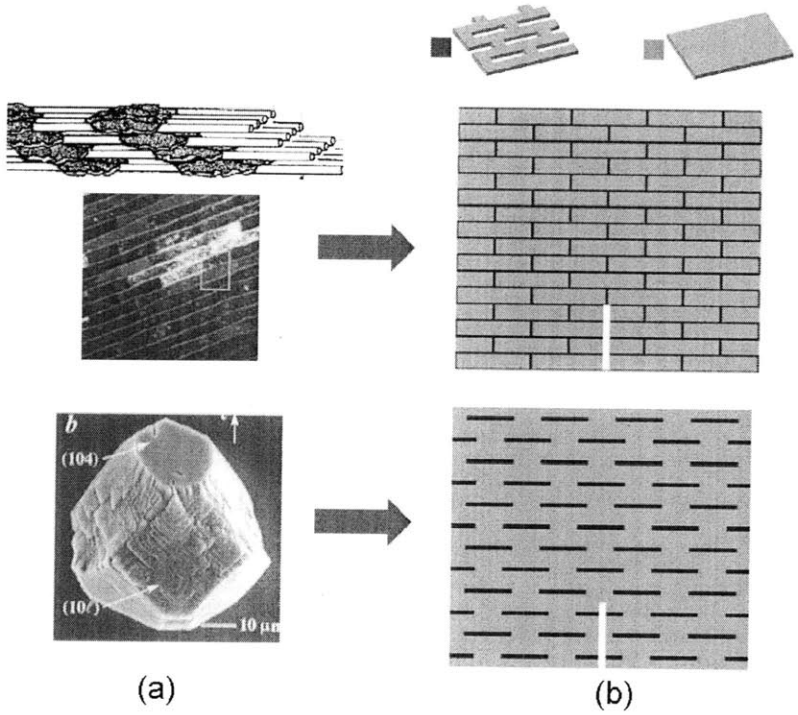

Figure 6-1: Periodic repeating design morphologies are chosen for the composite structure at the 2nd level of hierarchy. (a) shows the two representative systems chosen, one in which the soft/tough material is the continuous phase, with the hard/brittle material dispersed in platelet form within the matrix, mimicking several hierarchy levels in bone and nacre; the second representative system, in the lower part of (a) panel, is where the hard/brittle constituent is the continuous phase, with regions of soft/tough material embedded within the hard matrix. These structures are found in biocrystals, where protein material is encapsulated in a hard crystal, such as biological calcite single crystals [194, 195]. These geometric arrangements are reproduced using bulk silica/nanoporous silica materials using the two-dimensional mesoscale model (see Chapter 5), as shown in (b), which we will refer to as bone-like and biocalcite-like in the subsequent text.

of a crack. Thus the biocalcite-like structure shows higher defect-tolerance at the cost of lower fracture strength.

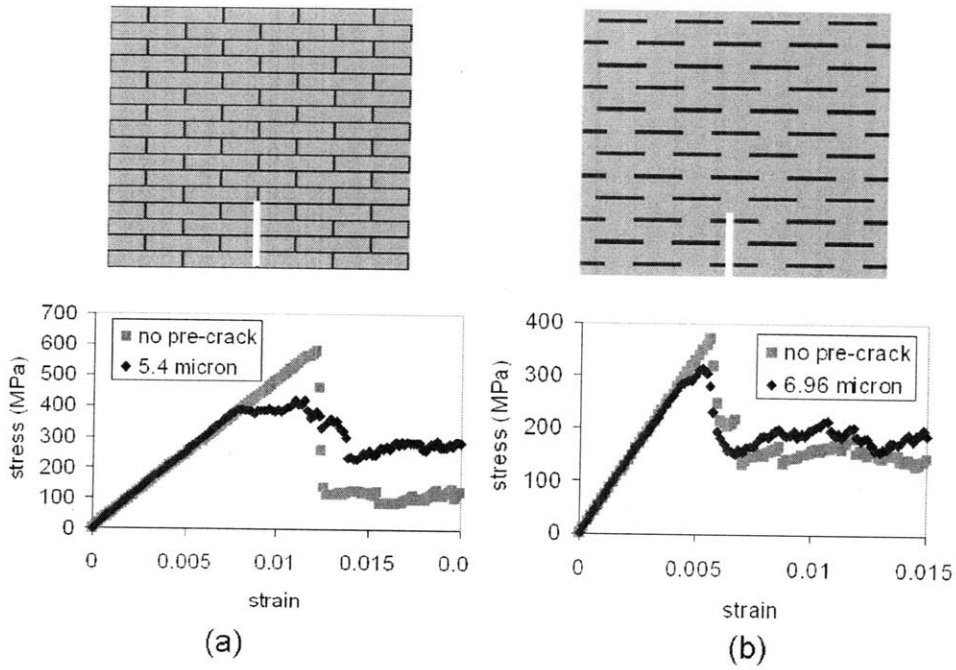

Figure 6-2: Stress-strain curves for (a) bone-like composite structures, with and without presence of a pre-crack. Fracture strength changes drastically on the introduction of a crack. (b) Stress-strain curves for a biocalcite-like composite structure, with and without presence of a pre-crack. The sensitivity to fracture strength is much smaller than for the bone-like composite, though the magnitude of the fracture strength is lower.

Taking a closer look at the fracture mechanics and crack propagation in both structures, Figure 6-3 gives us a clue as to why the biocalcite-like structure possesses higher defect tolerance. For small crack sizes, failure in these materials propagates through the nucleation of several micro-cracks at nano-porous silica/bulk-silica interfaces located from the original crack tip. This makes the failure morphology appear quite similar in the presence of smaller cracks and the absence of any, and provides comparable fracture strength values. On the other hand, for the bone-like structures, the pre-crack always propagates and is toughened by platelets bridging the wake of the crack as it propagates.

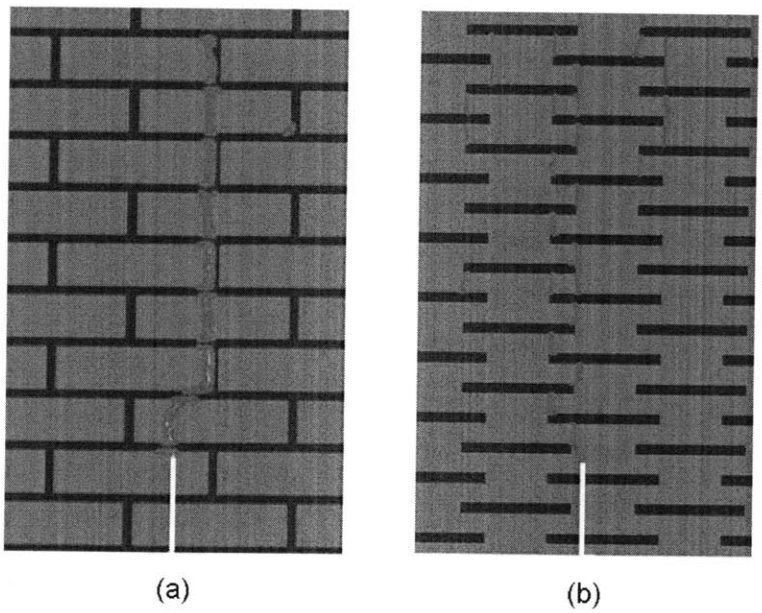

Figure 6-3: Crack pathways (marked in red) for bone-like and biocalcite-lie hierarchical structures in the presence of a pre-crack. (a) shows that for the bone-like structures, the pre-crack propagates through the sample, but the structure is toughened by platelets bridging the wake of the crack as it propagates. (b) shows that for small crack sizes, failure in the biocalcite-like structure propagates through the nucleation of several micro-cracks at nano-porous silica/bulk-silica interfaces located far from the original crack tip. The fracture strength is reached when several of these micro-cracks link up along with the pre-crack to create a failure pathway through the sample. These results show that the different crack propagation pathways in the two structures lead to different defect-tolerance response.

6.2.2 Extension to 3- and 4-hierarchy level structures

The 2-hierarchy structures in the last section are now extended to an additional level of hierarchy. Both self-similar geometries, in the vein of earlier studies [36], and dissimilar geometries are considered (see Figure 6-4). Self-similar (fractal) geometries are not found in biological materials, but have been used in previous literature to build simple models of hierarchical structures; dissimilar geometries are chosen as more representative of how the actual hierarchy levels in bone, diatoms etc. are very different from each other in geometry. The self-similar geometry uses a replica of the bone-like arrangement at two different scales (Figure 6-4(a)). The platelets size at the 2nd level of hierarchy is 5.95 µm by 1.16 µm in cross-section, while at the third level is 12.7 µm by 5.4 µm. The overall sample size is 54 µm by 70 µm in the X-Y plane, and 100 nm in the out-of-plane Z-direction. The dissimilar geometry is using the bio-calcite template for the 2nd level, and bone-like arrangement for the 3rd level of hierarchy (Figure 6-4(b)). Here, the platelets size at the 2nd level of hierarchy is 2.02 µm by 0.47 µm in cross-section, while at the third level is 12.6 µm by 5.5 µm. Initial crack sizes in these models range from ≈5–35 µm.

Figure 6-5 shows the stress-strain plot going from a 2-hierarchy bone-like structure to a 3-hierarchy self-similar assembly. The volume fraction of the two constituents, bulk silica and nanoporous silica, are kept constant at 80% and 20% respectively. The move from 2-hierarchy to 3-hierarchy system shows, (a) a decrease in fracture strength, and (b) an increase in defect-tolerance. Figure 6-6 shows the stress-strain plot going from a 2-hierarchy biocalcite-like structure to a 3-hierarchy dissimilar assembly. The volume fraction of the two constituents, bulk silica and nanoporous silica, are again, kept constant at 80% and 20% respectively. In this case, the move from 2-hierarchy to 3-hierarchy system shows a small change in fracture strength decrease in fracture strength, and again an increase in defect-tolerance.

We thus observe a pattern of increase in defect-tolerance size scale with the increase in number of hierarchy levels. In figure 6-7, we take a closer look at the source of this defect-tolerance. Here, we have taken several samples of the dissimi-

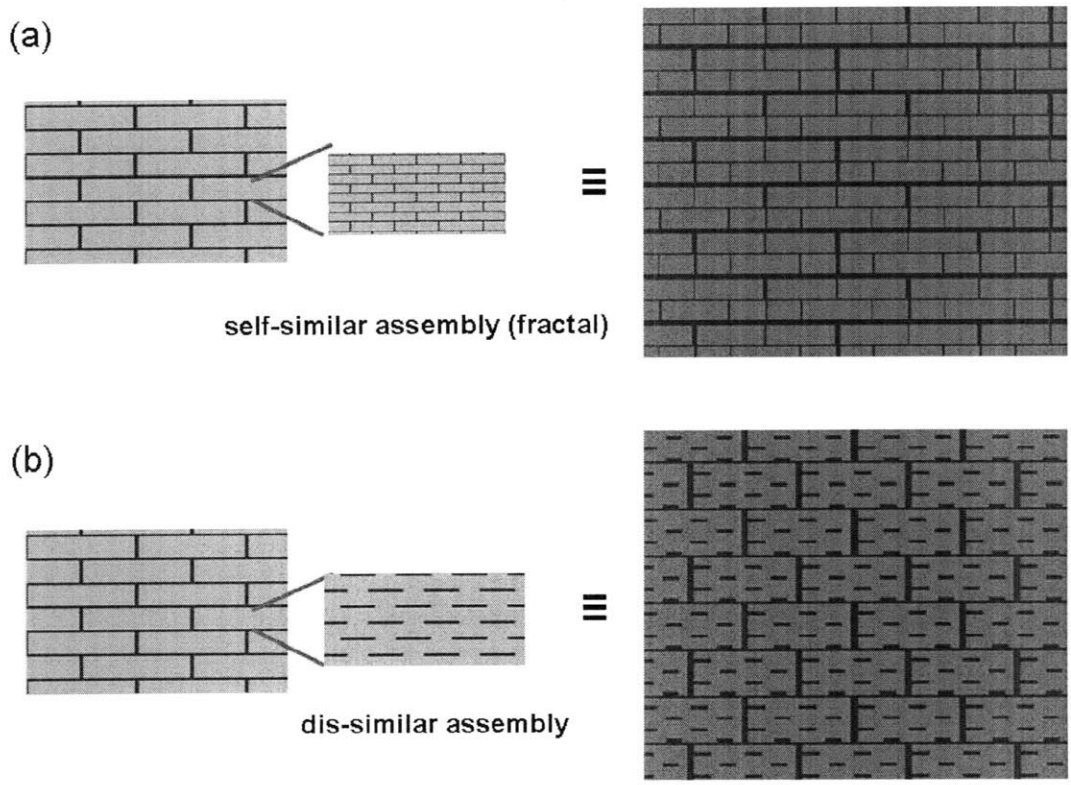

Figure 6-4: Geometry of 3-hierarchy composite structures, both self-similar and dissimilar in design between the 2nd and 3rd levels of hierarchy. The models are used to study how the assumption of self-similarity across hierarchies affects stress-strain response and toughness values. (a) shows the self-similar geometry using a replica of the bone-like arrangement at two different scales. The platelets size at the 2nd level of hierarchy is 5.95 μm by 1.16 μm in cross-section, while at the 3rd level is 12.7 μm by 5.4 μm. (b) shows the dissimilar 3-hierarchy geometry using the bio-calcite template for the 2nd level, and bone-like arrangement for the 3rd level of hierarchy. The platelets size at the 2nd level of hierarchy is 2.02 μm by 0.47 μm in cross-section, while at the 3rd level is 12.6 μm by 5.5 μm. The overall sample size is 54 μm by 70 μm by 100 nm in the out-of-plane direction (both cases).

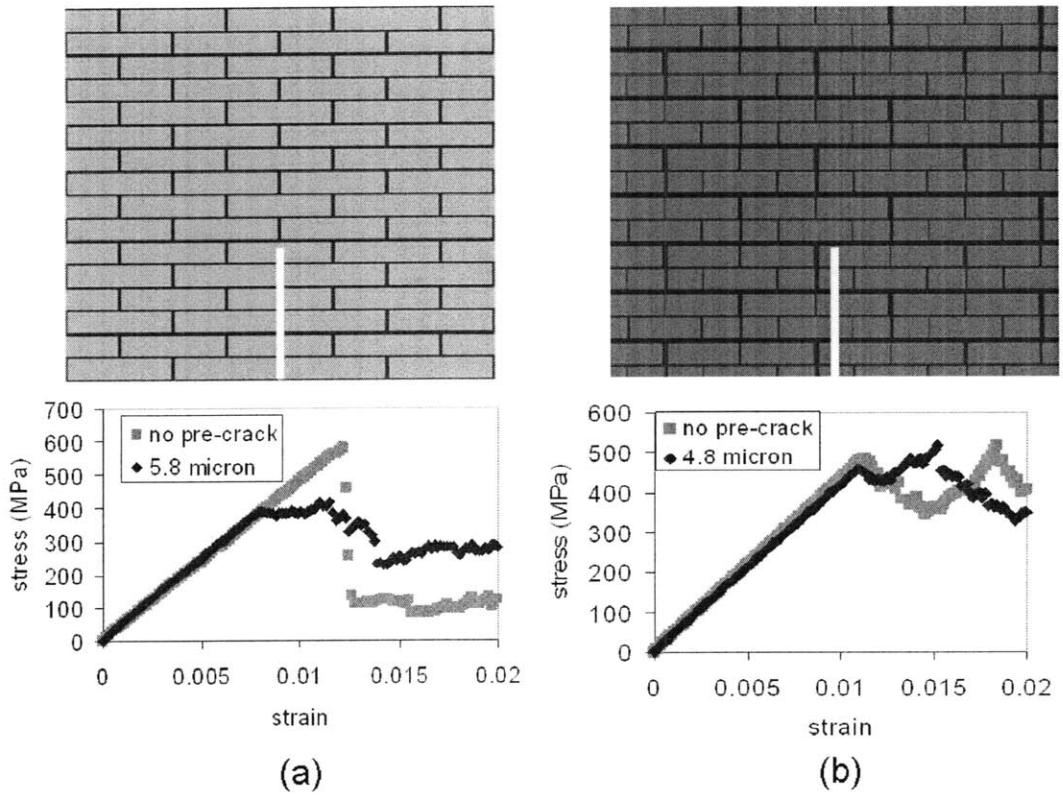

Figure 6-5: Stress-strain curves for (a) 2-hierarchy bone-like composite structures, with and without presence of a pre-crack; (b) 3-hierarchy self-similar structure made of bone-like composite structure at both the 2^{nd} and 3^{rd} levels, with and without presence of a pre-crack. The sizes of the pre-cracks are given in the figure legends. The sensitivity of fracture strength vs. crack size is much smaller for the 3-hierarchy material.

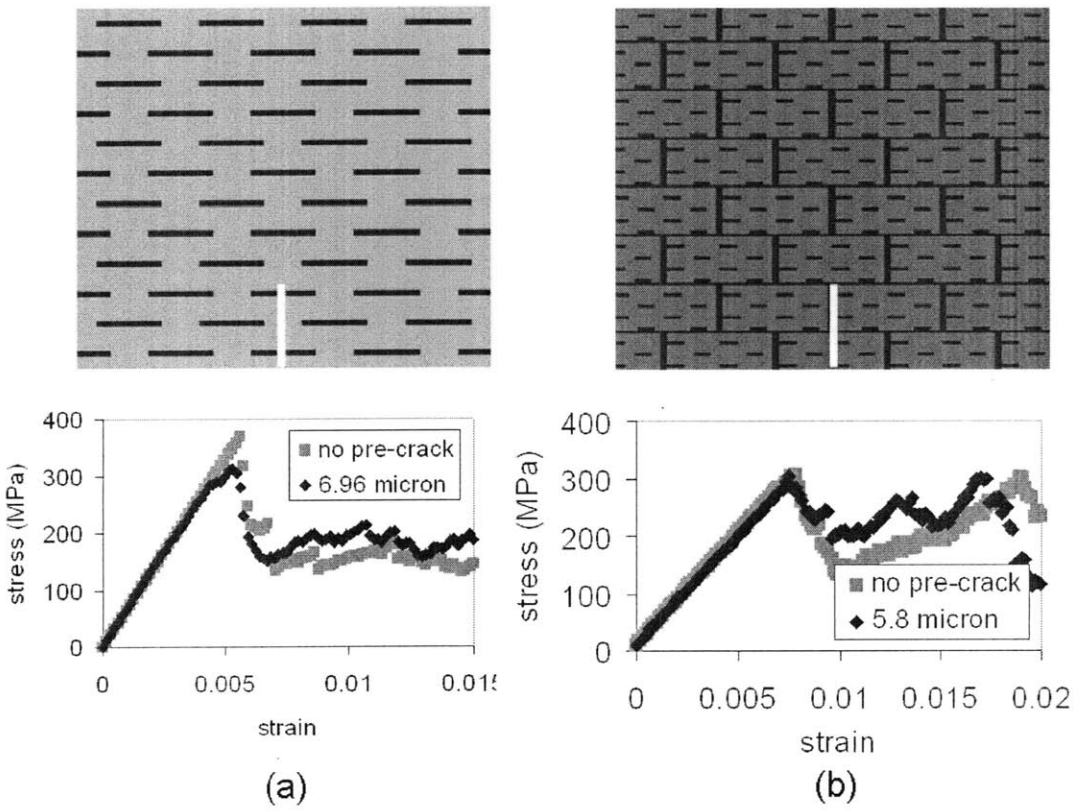

Figure 6-6: Stress-strain curves for (a) 2-hierarchy biocalcite-like composite structures, with and without presence of a pre-crack; (b) 3-hierarchy dissimilar structure made of biocalcite-like composite structure at the 2nd level and bone-like at the 3rd level, with and without presence of a pre-crack. The sizes of the pre-cracks are given in the figure legends. The sensitivity of fracture strength vs. crack size is smaller for the 3-hierarchy material.

lar 3-hierarchy structure with different crack sizes, and found the fracture strengths (Figure 6-7(a)). We find that with a 3-fold increase in crack size from 6 μm to 18 μm, there is only a 24% drop in fracture strength. A closer look at the mechanics of the stress-strain curves is taken in Figure 6-7(b) and (c). Here, we observe that the latter part of the rising stress region before fracture consists of the opening up of micro-cracks throughout the sample. Once these microcracks start moving, and link up to the pre-crack, there is unstable crack-propagation leading to a peak in stress and the fracture strength. This effect can also be measured through the total new surface area created during the diffuse micro-cracking regime, and while the main crack doesn't move (Figure 6-7(c)).

To observe whether this pattern of increase in defect-tolerance proceeds with the number of structural hierarchies, we create a model with 4 levels of hierarchy (Figure 6-8). Here the 2^{nd} structural level is biocalcite-like, while the 3^{rd} and 4^{th} levels are bone-like in design. The overall volume fraction of the bulk-silica constituent is still maintained at 80%. The overall sample size is 108 μm by 140 μm in the X-Y plane, and 100 nm in the Z-direction. The system consists of ≈3 million particles and ≈9 million bonds. The same mesoscale potentials used for the 2-hierarchy level structures is still used, and no further coarse-graining in the potential is carried out. Figure 6-8(b) shows the stress-strain curves for the 4-hierarchy structure with various crack sizes from ≈6 μm to ≈64 μm. Almost no change in fracture strength is seen over this very large change in the size of a crack present in the structure. The defect-tolerance, thus has improved substantially over that of the 2-hierarchy and 3-hierarchy structures. Figure 6-8(c) shows the R-curve behavior over 1, 2, 3, and 4 levels of hierarchy structures. The R-curve measures changes in fracture toughness as a crack proceeds through the change in energy released per unit length stable crack advance.

We observe a distinct effect of the addition of hierarchies on the R-curve behavior of the material. Both the absolute value of G_{Ic} versus crack advance, and the slope of the R-curve, $\partial G_{Ic}/\partial \Delta a$ increase with the number of hierarchies. The slope of the R-curve has a close relation to the concept of flaw-tolerance. As seen in Figure 6-9,

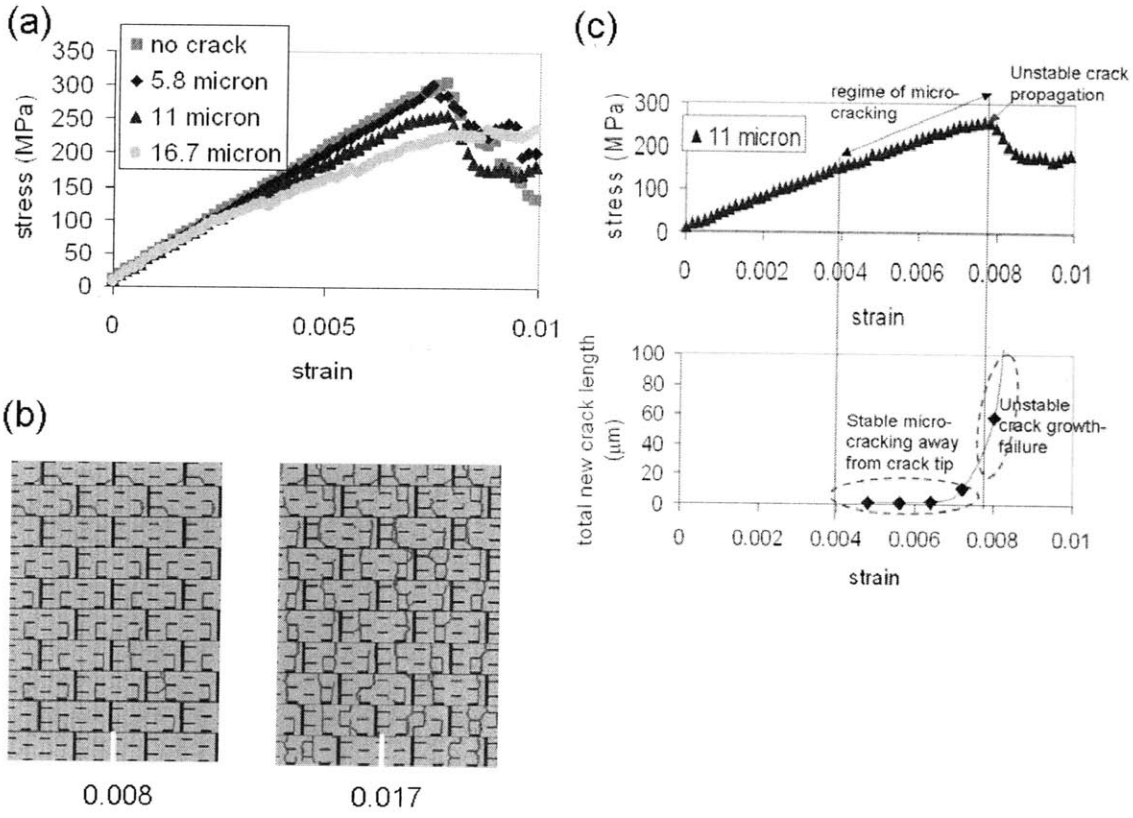

Figure 6-7: A closer look at the source of defect tolerance in 3-hierarchy structures. (a) shows the stress-strain behavior and fracture strengths for several samples of the dissimilar 3-hierarchy structure with different crack sizes. We find that with a 300% increase in crack size from 6 μm to 18 μm, there is only a 24% drop in fracture strength. (b) and (c) show that the latter part of the rising stress region before fracture consists of the opening up of micro-cracks throughout the sample. These micro-cracks are shown in red in part (b), with the numbers indicating overall strain values. Once these microcracks start moving, and link up to the pre-crack, there is unstable crack-propagation leading to a drop in stress and thus, the fracture strength. The lower part of (c) graph also shows that this effect can also be measured through the total new surface area created during the diffuse micro-cracking regime, at which time the main crack remains stationary.

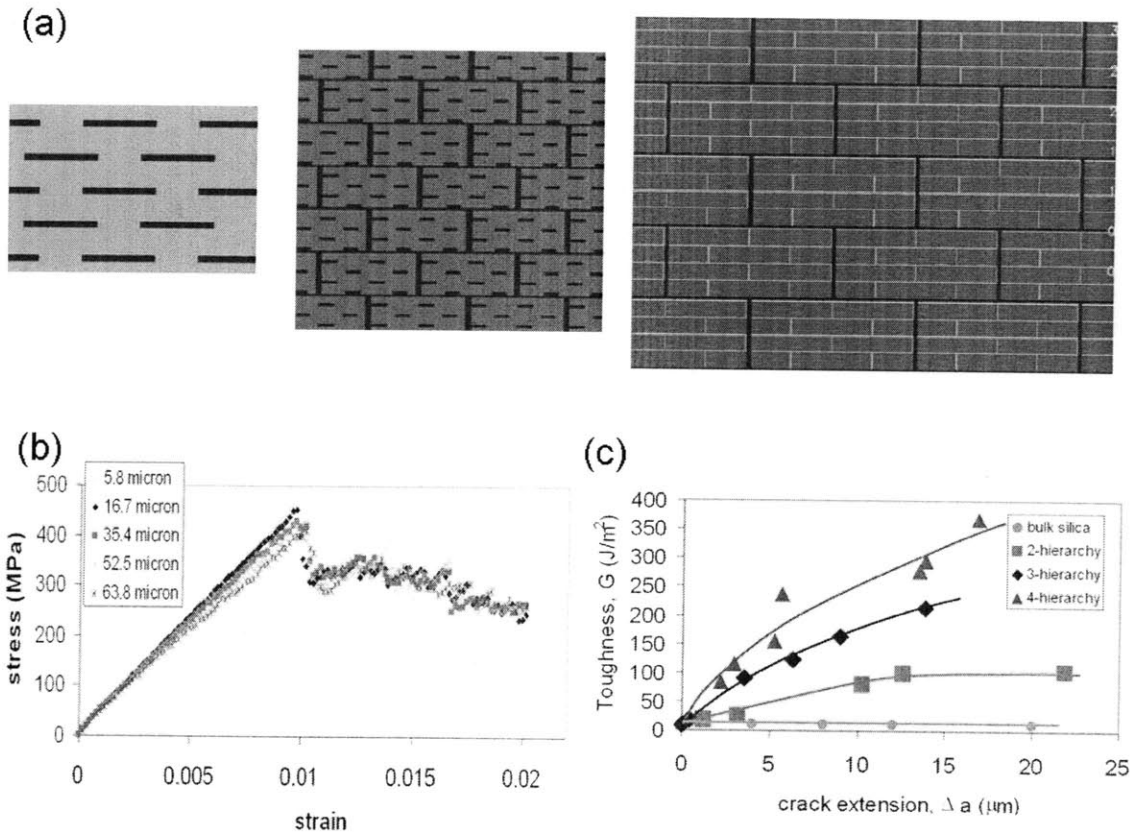

Figure 6-8: 4-hierarchy structure morphology, stress-strain plots and R-curve behavior. (a) shows the 2-hierarchy, 3-hierarchy and 4-hierarchy structures for comparison, with the 4-hierarchy structure having a 2nd hierarchical level that is biocalcite-like, while the 3rd and 4th levels are bone-like. In the 4-hierarchy structure, the color scheme is: bulk silica–red, nanoporous silica–green and blue, to show the 4 levels clearly. The overall volume fraction of the bulk-silica constituent is still maintained at 80%. The overall sample size is 108 μm by 140 μm in the X-Y plane, and 100 nm in the Z-direction. (b) shows the stress-strain curves for the 4-hierarchy structure with various crack sizes from ≈6 μm to ≈64 μm. Almost no change in fracture strength is seen over this very large change in crack size. The defect-tolerance has thus increased substantially over 2-hierarchy and 3-hierarchy structures. (c) shows the R-curve behavior over 1, 2, 3, and 4 levels of hierarchy structures. The R-curve measures changes in fracture toughness as a crack propagates through the change in energy released per unit length of stable crack advance.

in a material with a rising R-curve, unstable crack advance only occurs when the following conditions are satisfied,

$$G_{app} = G_{Ic} \; ; \qquad \frac{\partial G_{app}}{\partial a} = \frac{\partial G_{Ic}}{\partial a}. \tag{6.1}$$

where, G_{app} is the applied energy release rate, G_{Ic} is the fracture toughness from the R-curve, and a is the crack length. This, along with the load/energy-release relation for an edge crack, implies that the load at which a certain crack size will propagate unstably causing fracture, can be calculated by marking off the crack size on the negative-X axis of an R-curve, and constructing the tangent to the R-curve passing through this point. The slope of this curve is proportional to the load/ fracture stress at which this crack propagates unstably. This also implies that for a rising R-curve, the higher the rate of rise with crack advance, the lesser the sensitivity of fracture stress to crack size, and thus the higher the defect-tolerance length scale. Defect-tolerance length scales are thus closely linked to not only absolute values of fracture-crack initiation values [36], but also to the rising part of the R-curve through the slope of the R-curve.

This relation is clarified through the results shown in Figures 6-10 and 6-11. Fracture stress is measured for 2-, 3- , and 4-hierarchy structures for different crack sizes. The loss of strength as a percentage of the strength of the no-cracked samples has been plotted in Figure 6-10 for all the levels of hierarchy. We observe that the sensitivity of fracture strength to crack size goes down with increasing hierarchy level. If a 10% loss in strength is fixed as a defect-tolerance length scale, Figure 6-11 shows how this length scale increases non-linearly with the number of hierarchies.

6.3 Discussion and Conclusions

In this study, we study the fracture mechanics of hierarchical structures with 2 - 4 levels of hierarchy, using an atomistically-informed mesoscale method. We span

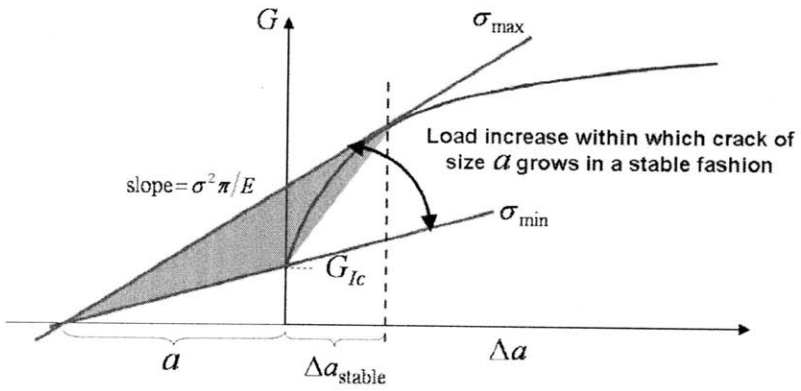

Figure 6-9: R-curve behavior in a material with a rising R-curve resistance, and link to unstable crack propagation. All hierarchical structures shown in Figure 6-8(a) show rising R-curve behavior, where the toughness grows with crack propagation from its initiation value. The load, at which a certain crack size will propagate unstably causing fracture, can be calculated by marking off the crack size on the negative-X axis of an R-curve, and constructing the tangent to the R-curve passing through this point. The slope of this curve is proportional to the load/ fracture stress at which this crack propagates unstably.

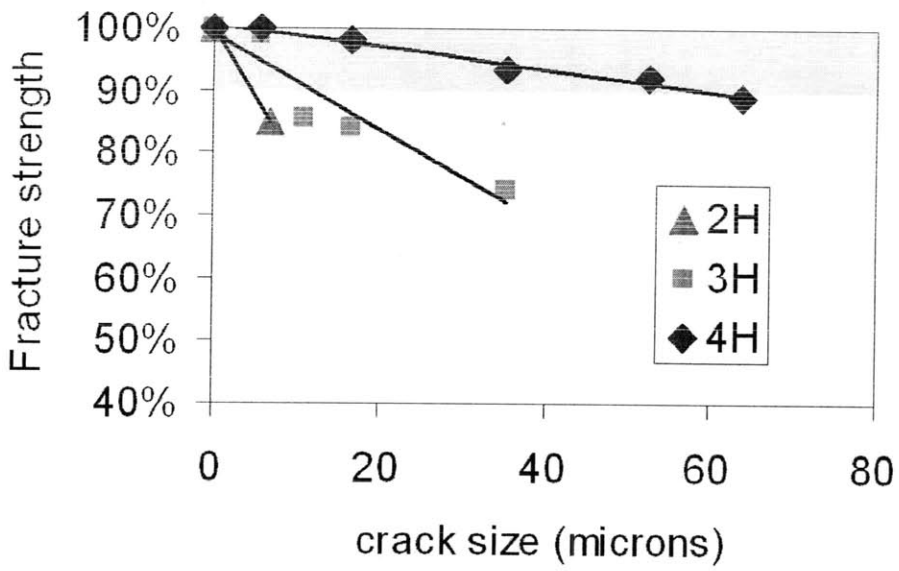

Figure 6-10: This shows the fracture stress, as a percentage loss from the strength of structures with no cracks, measured for 2-, 3- , and 4-hierarchy structures for different crack sizes. The shaded region shows the crack sizes for which there is a 10% loss in strength. We observe that the sensitivity of fracture strength to crack size goes down with increasing hierarchy level.

structures from sub-micron length scales to several hundreds of microns in size. The basic constituent of these structures is silica, which are nanostructured into porous form, inspired by diatom morphology, as shown in Chapter 4. Composites are created out of nanoporous silica and bulk silica as constituents.

We begin the study with the design of periodic ordered composite structures of bulk silica/nanoporous silica, classifying them into two representative systems; one in which the soft/tough material is the continuous phase, with the hard/brittle material dispersed in platelet form within the matrix, mimicking several hierarchy levels in bone and nacre. The second representative system is where the hard/brittle constituent is the continuous phase, with regions of soft/tough material embedded within the hard matrix. These structures are found in biocrystals, where protein material is encapsulated in a hard crystal, such as biological calcite single crystals. We observe that the biocalcite-like structures have a larger defect tolerance, *i.e.*, the sensitivity in change in fracture strength with crack size is smaller. We observe that this can be correlated to diffuse microcracking throughout the material even in the

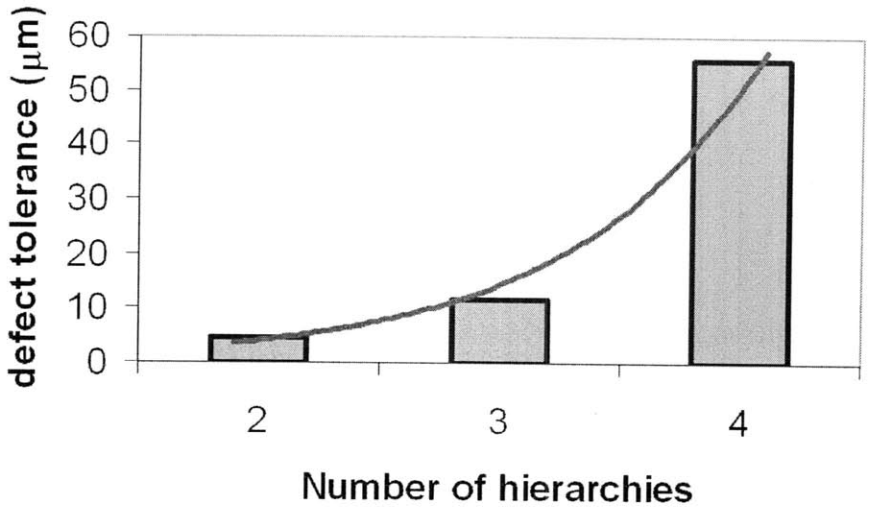

Figure 6-11: A defect-tolerant length scale is calculated to be the crack size at which the material retains 90% of its fracture strength. This figure shows how this length scale increases non-linearly with the number of hierarchies. The defect-tolerance reaches up to ≈60 μm with 4 levels of hierarchy. The red line represents an exponential fit of $L = 1.17e^{1.255N}$, where L is the defect-tolerant length scale in microns, and N is the number of hierarchy levels. The limiting value of 1 level of hierarchy, *i.e.*, bulk silica, does not show any defect-tolerant response to crack size.

presence of stress-concentrators such as small cracks.

Subsequently, we design 3- and 4-hierarchy level structures using different combinations of the bone-like and biocalcite-like templates. We observe that the defect tolerance length scale increases with number of hierarchy length scales. R-curves, which capture change in fracture toughness per unit length stable crack advance in a material, are measured for all hierarchy levels. The defect-tolerance property is then correlated with a rising R-curve behavior, in particular the slope of the R-curve. It is seen that the R-curve increases in both magnitude and slope as the number of hierarchy levels increase. Experimentally, R-curves have been measured for fracture samples of hierarchical biological materials such as bone, nacre, and dentin, and a similarly rising R-curve behavior is seen [196, 184, 197, 198].

The improvement in the defect-tolerance property, which captures both increase in crack initiation toughness [36], and the increase in the R-curve slope, is captured numerically through a length scale at which the structure loses 10% of its no-crack fracture strength. We observe that this quantity increases rapidly with number of

hierarchy levels, reaching ≈60 μm for 4 levels of hierarchy.

The use of several levels of hierarchy is thus shown to impact toughness through many effects. Apart from higher absolute toughness values, we find that the use of hierarchies also increases the rate of increase of toughness per unit crack advance. These together lead to a higher defect tolerance for structures with greater number of hierarchy levels. This behavior can provide an explanation for the use of multiple hierarchies in biological materials. Stable crack advance is not catastrophic or disabling for biological materials, since many materials, such as bone, have the ability to self-heal over time. A rising R-curve behavior, across several microns or higher length scales, promotes stable crack advance in the material and allows it to be useful beyond its fracture initiation load point. Thus large loads, which would shatter a single hierarchy material with a single crack propagating right through the material, dissipate energy in multiple-hierarchy materials through several cracks being initiated and arrested at different length scales (see Figures 6-3(b) and 6-7(b) and (c)). If the load doesn't rise to unstable propagation values, this probably provides the material time to heal, and still carry load. We observe that a higher number of hierarchies is provides a better rising R-curve behavior.

Future work could be aimed at optimizing the entire R-curve behavior over several microns or higher length-scale of crack advance. Both the number of hierarchies, and design of individual hierarchy levels, would have different effects on the entire R-curve shape. Our mesoscale model is a stepping stone that can be utilized for design-optimization to maximize R-curve magnitude and slope improvements. The model can also be extended to larger length scales, potentially sub-mm, such that R-curve toughness improvement is seen over length scales comparable to the macroscopic sample size.

Chapter 7

Conclusion

This chapter summarizes key findings of this thesis, and discusses the significance of results obtained from simulation and theoretical considerations of the importance of (a) nanostructuring and (b), the use of hierarchical assembly in bio-inspired materials. The ability to use mechanically 'poor' materials as building blocks to obtain structures that optimize disparate mechanical properties simultaneously, is the goal of mimicking biological mechanical design, and a bottom-up design methodology to achieve this has also been outlined. Also, later in this chapter, we touch on directions for future research to improve and build on these results.

7.1 Summary of key findings and significance

Mimicking biological materials design is an important frontier in materials design. This is driven by several enviable properties of biological materials, primary of which is they utilize very 'poor' engineering materials such as protein, silica, hydroxyapatite to build animal skeletons and protective armors. They also combine these 'poor' engineering materials to make composites that possess a combination of the best of the properties of their constituents. As an example, this behavior is easily captured through Ashby materials properties' charts of stiffness versus toughness for biological materials and engineering materials (see Figure 1-1). Engineering materials, such as metals, alloys, ceramics, and their composites, show a 'banana-curve' behavior where

one of these properties is improved at the cost of another [4]. Biological materials, made of protein and calcite/hydroxyapatite, such as bone, antler, enamel etc. show an 'inverse banana-curve' behavior where these materials combine the high toughness of the protein constituent with the high stiffness of the mineral constituent [2]. Biological materials also present multi-functionality and optimization of several desirable properties. Finally, they also show robustness, or resistance to catastrophic damage. Due to the heterogeneous, hierarchical nature of the design structure of these biological materials, and the presence of a wide variety of designs, it is key to be able to discover key underlying universal design principles that can then be transferred and applied to any common engineering constituents. In this work, we identified three general design principles,

- nanostructuring according to nano-motifs found in several biological systems,
- use of 'poor' materials as structural building blocks,
- use of several hierarchy levels to reach from the nanoscale structure to macroscale, using well-defined assembly at each level of intermediate hierarchy.

We began our analysis by firstly, selecting the platelet-matrix nanostructure of bone and nacre, as a design template to mimic. Since these nanostructures are composed of hard/stiff calcite/hydroxyapatite platelets embedded in a soft/ductile protein matrix, we chose hard and soft metals to replace the bone constituents. We thus designed metal-matrix composites with geometric design inspired by bone nanostructure in Chapter 3, and studied their mechanical properties under tensile loading. We found significant dependence of flow strength of these nanocomposites on the geometry parameters of the bone nanostructure, and found size limits which maximized the strength of these composites. Or analysis also revealed that there exist fundamental, intrinsic length scales that control their plastic deformation mechanism and strength properties. Specifically, we found that the use of elongated platelets in the composite, of high aspect ratio and staggered arrangement of platelets for optimal load transfer, and control of spacing between layers of platelets are critical factors in strengthening

the material. The spacing between platelets perpendicular to the direction of loading was found to have a Hall-Petch like effect on the flow strength. We also observed that the strength of the platelet/matrix interface determines the optimal size of the platelets at which the maximal flow strength is observed for the nanocomposite. The interfacial strength between matrix and platelets turned out to be key in determining the importance of sliding and decohesion as deformation mechanisms at small platelet sizes, and inter-platelet spacing. This leads to a peak flow strength for the nanocomposite as a function of platelet size. Analysis of the mechanisms behind this plateauing of strength, revealed that there exists a few fundamental length scales that depend only on material parameters and the particular geometry, that control the plastic deformation mechanism in small crystals under confined conditions. Theoretical analysis shows that these characteristic length scales separate regimes of no dislocation activity, partial dislocation plasticity, and complete dislocation plasticity at crack tips in ductile metals. We confirmed this effect by direct atomistic simulation of shear loading of a model ductile single crystal system. Thus, geometrically confined ductile phases, in the metal-matrix nanocomposites under loading, will show a transition to homogeneous shear based plasticity below a critical length scale. This could provide important guidance for the optimal design of such nanocomposites, as below a certain size scale of the ductile constituent, it will fail at its theoretical strength and any further reduction in the critical dimension will not increase the failure strength.

Metals, however are economically costly constituents to use in design. Is it possible to design bio-inspired structures using cheap and readily available materials? An example is silica, which is abundantly found as sand; economically very inexpensive but also possessing 'poor' mechanical properties. In particular, it is brittle and possesses low fracture toughness, and cannot be used as a structural material in its bulk form, whether its amorphous glassy form or crystalline quartz form. However, in biological materials, silica is abundantly used to create protective exoskeletons in many species of diatoms and sea sponges. We, thus, next moved to the use of this 'poor' engineering material, silica, instead of metals for creating bio-inspired structures in Chapter 4. We turn to the structure of diatom exoskeleton (see Figure 1-2) for inspiration. The

mechanics of diatom-inspired nanoporous silica structures under tensile loading were investigated using molecular dynamics simulation and theoretical analysis. We found that the elastic modulus of the nanoporous structures is geometry dependent, and can be modified for a given porosity by changing the microstructure. Moreover, we found that the stress-strain loading curves for these silica structures exhibit plasticity below a certain size scale. We were able to establish a size-dependent brittle-to-ductile transition in nanoporous silica structures. The aspect ratio and shape of pores can be modified to control the yield strength of these structures, and obtain large amounts of ductility of up to 120% strain. The structures that show plastic yielding also show large toughness improvement over bulk silica. These results reveal that nanostructuring with control of porous geometry can lead to application of silica in carrying loads in small devices.

The advantages of this nanoporous design, however, come at a cost; these structures lose up to 90% of the stiffness of bulk silica. Since hierarchical design is hypothesized to be a methodology to achieve multiple property optimization, is it possible to use hierarchies to improve stiffness of the nanoporous silica structures up to bulk silica values? Moreover, can this be accomplished by engineering silica alone, *i.e.*, use of a single constituent material? In Chapter 5, we demonstrated that it is possible to enhance the toughness of silica while retaining its stiffness, without using any other material, through the use of structural hierarchies. We developed an atomistically-informed mesoscale model that can model bulk silica and nanoporous silica behavior at the micron length scale. By design of a randomly-dispersed composite structure of the bulk silica/ nanoporous silica, we are able to retain stiffness up to 70% of bulk silica while increasing toughness four times over its value. This improvement in toughness and retaining of stiffness of bulk silica by designing small regions of nanoporous geometry ($\approx$14%) in the bulk phase point to a design methodology for obtaining stiff and tough materials out of an inherently brittle material (silica) to begin with. Thus we were able to achieve a hierarchical structure with high stiffness and toughness through the use of a single material – silica – which is traditionally considered an undesirable (mechanically inferior) structural material due to its brit-

tleness, by arranging it in a hierarchical pattern with substructures that scale from the nanoscale to microscale dimensions.

We then proceeded to the analysis of several levels of hierarchical arrangement of bulk silica/ nanoporous silica composites on toughness, in Chapter 7. We observed that the structural R-curve shows a rising characteristic for additional levels of hierarchy. Thus both the absolute value of toughness, and the slope of the R-curve increase with the number of hierarchy levels (see Figure 6-8. This leads to an increasing defect-tolerance, *i.e.*, fracture strength loses its sensitivity to changes in crack length (see Figure 6-10). We showed a non-linear increase in this defect-tolerance length with additional levels of hierarchy (see Figure 6-11). This behavior can be linked to the use of multiple hierarchies in biological materials. Stable crack advance is not catastrophic or disabling for biological materials, since many materials, such as bone, have the ability to self-heal over time. A rising R-curve behavior, across several microns or higher length scales, promotes stable crack advance in the material, and allows it to be useful beyond its fracture initiation load point.

This thesis established a direction and methodology in understanding and applying universal design principles that can be gleaned from biological materials for materials design for structural applications. Fully-atomistic and mesoscale modeling showcased a bottom-up fully computational approach to implementing these design principles.

7.2 Opportunities for future research

The previous section discussed the atomistic, theoretical and mesoscale modeling of implementation of bio-inspired design principles in hierarchical structures based on metals and silica. The purpose of this section is to illustrate the shortcomings of the current work and propose directions for future research on computational design of bio-inspired hierarchical materials.

The design and manufacturing of bone-inspired metal-matrix nanocomposites requires the simulation of actual metal/metal composite systems. Model materials, as used in Chapter 3, provide broad design guidelines, but the question of exactly which

metal constituents to use can be settled by atomistic simulations with well-developed metal and metal alloy interatomic potentials. The thermodynamic and kinetic stability of interfaces between the constituents and the equilibrium configuration of the interfaces are also important considerations to the mechanical behavior that can only be settled through simulations of particular metal/metal systems and experiments.

The study of the design of diatom-inspired nanoporous silica structures can be enhanced by analyzing their mechanical properties in a hydrated environment. This is because the presence of water has been shown to have an effect on silica mechanical properties, both in bulk and nanoscale [157]. Some preliminary investigations have been performed on the response of these nanoporous structures in the presence of hydrogen and water [156]. Silica surface termination is also affected by the environment and nature of the exposed crystal surface, and the nanoporous structures possess sufficient surface area such that the surface mechanical response is important. Also, these designs experiments can be undertaken for amorphous silica, which is the form in which bio-silica in diatoms is found.

The study of hierarchical assemblies of silica through atomistically-informed mesoscale models, as seen in Chapters 5 and 6, can be regarded as a preliminary attempt in this emerging area of computational study of hierarchies in materials. Mesoscale models have been used for several other biological systems with hierarchies, such as collagen fibrils, amyloids, spider silk, and is a promising approach to extracting qualitative design information about the requirement and advantages of hierarchical design. This can be contrasted with fractal continuum-level approaches [36, 187] which are much coarser in the details of geometry and deformation they capture. In further studies, mesoscale models of hierarchical materials, can be used along with design optimization techniques such as genetic algorithms, to optimize material distribution and arrangement over several length scales of hierarchy. In particular, it may be possible to optimize R-curve shape over several levels of hierarchy and length-scale to increase crack propagation toughness, and stop and repair cracks before they cause complete failure.

Bibliography

[1] J. Y. Rho, L. Kuhn-Spearing, and P. Zioupos. Mechanical properties and the hierarchical structure of bone. *Medical Engineering and Physics*, 20(2):92–102, 1998.

[2] M. F. Ashby, L. J. Gibson, U. Wegst, and R. Olive. The mechanical properties of natural materials. i. material property charts. *Proceedings: Mathematical and Physical Sciences*, 450(1938):123–140, 1995.

[3] P. Fratzl, H. S. Gupta, E. P. Paschalis, and P. Roschger. Structure and mechanical quality of the collagenmineral nano-composite in bone. *Journal of Materials Chemistry*, 14(14):2115–2123, 2004.

[4] M.F. Ashby. *Materials selection in mechanical design*. Butterworth-Heinemann, 2005.

[5] S. A. Wainwright, W. D. Biggs, J. D. Currey, and J. M. Gosline. *Mechanical design in organisms*. Princeton University Press, 1976.

[6] J. D. Currey. The design of mineralised hard tissues for their mechanical functions. *The Journal of experimental biology*, 202:3285–3294, 1999.

[7] M. A. Meyers, P. Y. Chen, A. Y. M. Lin, and Y. Seki. Biological materials: Structure and mechanical properties. *Progress in Materials Science*, 53(1):1–206, 2008.

[8] H. H. Pattee. *Hierarchy Theory: The Challenge of Complex Systems*. George Braziller, 1973.

[9] M. Idan, M. Johnson, and A. J. Calise. Hierarchical approach to adaptive control for improved flight safety. *Journal of Guidance, Control, and Dynamics*, 25(6):1012–1020, 2002.

[10] J. Wu and J. L. David. A spatially explicit hierarchical approach to modeling complex ecological systems: theory and applications. *Ecological Modelling*, 153(1-2):7–26, 2002.

[11] M. E. Csete and J. C. Doyle. Reverse engineering of biological complexity. *Science*, 295(5560):1664, 2002.

[12] J. Stelling, U. Sauer, Z. Szallasi, F. J. Doyle, and J. Doyle. Robustness of cellular functions. *Cell*, 118(6):675 685, 2004.

[13] T. Ackbarow and M.J. Buehler. Hierarchical coexistence of universality and diversity controls robustness and multi-functionality in protein materials. *Theoretical and Computational Nanoscience*, 5(7):1193 1204, 2008.

[14] I. A. Aksay and S. Weiner. Biomaterials is this really a field of research? *Current Opinion in Solid State & Materials Science*, 3(3):219 220, 1998.

[15] T. Christman, A. Needleman, and S. Suresh. An experimental and numerical study of deformation in metal–ceramic composites. *Acta Metall.*, 37(11):3029–3050, 1989.

[16] J. Delmonte. *Metal/Polymer Composites*. Van Nostrand Reinhold, 1990.

[17] P. M. Ajayan, L. S. Schadler, C. Giannaris, and A. Rubio. Single-walled carbon nanotube/polymer composites: Strength and weakness. *Advanced Materials*, 12(10):750–753, 2000.

[18] E. Flahaut, A. Peigney, C. Laurent, C. Marlire, F. Chastel, and A. Rousset. Carbon nanotubemetaloxide nanocomposites: microstructure, electrical conductivity and mechanical properties. *Acta Materialia*, 48(14):3803–3812, 2000.

[19] P. M. Derlet, A. Hasnaoui, and H. Van Swygenhoven. Atomistic simulations as guidance to experiments. *Scripta Materialia*, 49(7):629–635, 2003.

[20] M. J. Buehler, Y. Kong, and H. Gao. Deformation mechanisms of very long single-wall carbon nanotubes subject to compressive loading. *Journal of Engineering Materials and Technology*, 126:245, 2004.

[21] D. Wolf, V. Yamakov, S. R. Phillpot, A. Mukherjee, and H. Gleiter. Deformation of nanocrystalline materials by molecular-dynamics simulation: relationship to experiments? *Acta Materialia*, 53(1):1 40, 2005.

[22] R. Lakes. Materials with structural hierarchy. *Nature*, 361(6412):511–515, 1993.

[23] P. Fratzl and R. Weinkamer. Nature's hierarchical materials. *Progress in Materials Science*, 52(8):1263–1334, 2007.

[24] L. Bertalanffy. *General system theory: Foundations, development, applications*. G. Braziller, New York, 1973.

[25] H. Kitano. Systems biology: A brief overview. *Science*, 295:1662–1664, 2002.

[26] D.R. Carter and D.A.N.M. Spengler. Mechanical properties and composition of cortical bone. *Clinical Orthopaedics and Related Research*, 135:192, 1978.

[27] D. Losic, R. J. Pillar, T. Dilger, J. G. Mitchell, and N. H. Voelcker. Atomic force microscopy (afm) characterisation of the porous silica nanostructure of two centric diatoms. *Journal of Porous Materials*, 14(1):61–69 , 2007.

[28] J. Aizenberg, J. C. Weaver, M. S. Thanawala, V. C. Sundar, D. E. Morse, and P. Fratzl. Skeleton of euplectella sp.: Structural hierarchy from the nanoscale to the macroscale. *Science*, 309(5732):275–278, 2005.

[29] J. D. Currey. Materials science: Hierarchies in biomineral structures. *Science*, 309(5732):253–254, 2005.

[30] A. Woesz, J. C. Weaver, M. Kazanci, Y. Dauphin, J. Aizenberg, D. E. Morse, and P. Fratzl. Micromechanical properties of biological silica in skeletons of deep-sea sponges. *Journal of Materials Research*, 21(8):2068–2078, 2006.

[31] M.J. Buehler. Strength in numbers. *Nat. Nanotechnol*, 5(3):172–174, 2010.

[32] R. K. Nalla, J. J. Kruzic, and R. O. Ritchie. On the origin of the toughness of mineralized tissue: microcracking or crack bridging? *Bone*, 34(5):790–798, 2004.

[33] H. Gao, B. Ji, I.L. Jäger, E. Arzt, and P. Fratzl. Materials become insensitive to flaws at nanoscale: Lessons from nature. *P. Natl. Acad. Sci. USA*, 100(10):5597–5600, 2003.

[34] B. L. Smith, T. E. Schaeffer, M. Viani, J. B. Thompson, N. A. Frederick, J. Kindt, A. Belcher, G. D. Stucky, D. E. Morse, and P. K. Hansma. Molecular mechanistic origin of the toughness of natural adhesives, fibres and composites. *Nature*, 399(6738):761–763, 1999.

[35] M. E. Launey, M. J. Buehler, and R. O. Ritchie. On the mechanistic origins of toughness in bone. *Annu. Rev. Mater. Res*, 40:25–53, 2010.

[36] H. Gao. Application of fracture mechanics concepts to hierarchical biomechanics of bone and bone-like materials. *International Journal of Fracture*, 138(1):101–137, 2006.

[37] S. Mann, D. D. Archibald, J. M. Didymus, T. Douglas, B. R. Heywood, F. C. Meldrum, and N. J. Reeves. Crystallization at inorganic-organic interfaces: Biominerals and biomimetic synthesis. *Science*, 261(5126):1286–1292, 1993.

[38] P. Gilbert, M. Abrecht, and B. H. Frazer. The organic-mineral interface in biominerals. *Reviews in Mineralogy and Geochemistry*, 59(1):157–185, 2005.

[39] C. E. Hamm, R. Merkel, O. Springer, P. Jurkojc, C. Maier, K. Prechtel, and V. Smetacek. Architecture and material properties of diatom shells provide effective mechanical protection. *Nature*, 421(6925):841–843, 2003.

[40] N. Almqvist, Y. Delamo, B. L. Smith, N. H. Thomson, A. Bartholdson, R. Lal, M. Brzezinski, and P. K. Hansma. Micromechanical and structural properties of a pennate diatom investigated by atomic force microscopy. *Journal of Microscopy*, 202(3):518–532, 2001.

[41] D. Losic, K. Short, J. G. Mitchell, R. Lal, and N. H. Voelcker. Afm nanoindentations of diatom biosilica surfaces. *Langmuir*, 23(9):5014 5021, 2007.

[42] M.J. Buehler. *Atomistic modeling of materials failure*. Springer Verlag, 2008.

[43] BJ Alder and TE Wainwright. Studies in molecular dynamics. i. general method. *The Journal of Chemical Physics*, 31:459, 1959.

[44] A. Rahman. Correlations in the motion of atoms in liquid argon. *Phys. Rev*, 136(2A):405–411, 1964.

[45] M. Springborg. *Density-functional methods in chemistry and materials science*. Wiley Chichester, 1997.

[46] M.J. Buehler and Y.C. Yung. Deformation and failure of protein materials in physiologically extreme conditions and disease. *Nature materials*, 8(3):175–188, 2009.

[47] H. J. C. Berendsen, J. P. M. Postma, W. F. Van Gunsteren, A. DiNola, and J. R. Haak. Molecular dynamics with coupling to an external bath. *The Journal of Chemical Physics*, 81:3684, 1984.

[48] S. Nose. Constant-temperature molecular dynamics. *Journal of Physics: Condensed Matter*, 2, 1990.

[49] T. Schneider and E. Stoll. Molecular-dynamics study of a three-dimensional one-component model for distortive phase transitions. *Physical Review B*, 17(3):1302–1322, 1978.

[50] G.J. Martyna, D.J. Tobias, and M.L. Klein. Constant pressure molecular dynamics algorithms. *constraints*, 4(9):0, 1994.

[51] M. Parrinello and A. Rahman. Polymorphic transitions in single crystals: A new molecular dynamics method. *Journal of Applied Physics*, 52(12):7182–7190, 1981.

[52] M.P. Allen and D.J. Tildesley. *Computer simulation of liquids*. Clarendon Press, 1989.

[53] S. M. Foiles, M. I. Baskes, and M. S. Daw. Embedded-atom-method functions for the fcc metals cu, ag, au, ni, pd, pt, and their alloys. *Physical Review B*, 33(12):7983–7991, 1986.

[54] L.A. Girifalco and VG Weizer. Application of the morse potential function to cubic metals. *Physical Review*, 114(3):687 690, 1959.

[55] M. S. Daw and M. I. Baskes. Embedded-atom method: Derivation and application to impurities, surfaces, and other defects in metals. *Physical Review B*, 29(12):6443 6453, 1984.

[56] M. S. Daw, S. M. Foiles, and M. I. Baskes. The embedded-atom method: a review of theory and applications. *Materials Science Reports(The Netherlands)*, 9(7):251–310, 1993.

[57] R. A. Johnson. Phase stability of fcc alloys with the embedded-atom method. *Physical Review B*, 41(14):9717–9720, 1990.

[58] R. A. Johnson. Alloy models with the embedded-atom method. *Physical Review B*, 39(17):12554 12559, 1989.

[59] MI Baskes, JS Nelson, and AF Wright. Semiempirical modified embedded-atom potentials for silicon and germanium. *Physical review B*, 40(9):6085–6100, 1989.

[60] MI Baskes and RA Johnson. Modified embedded atom potentials for hcp metals. *Modelling and Simulation in Materials Science and Engineering*, 2:147, 1994.

[61] A. C. T. van Duin, S. Dasgupta, F. Lorant, and W. A. Goddard Iii. Reaxff: a reactive force field for hydrocarbons. *J. Phys. Chem. A*, 105(41):9396 9409, 2001.

[62] A. C. T. van Duin, A. Strachan, S. Stewman, Q. Zhang, X. Xu, and W. A. Goddard Iii. Reaxff sio reactive force field for silicon and silicon oxide systems. *J. Phys. Chem. A*, 107(19):3803–3811, 2003.

[63] A. Strachan, A. C. T. van Duin, D. Chakraborty, S. Dasgupta, and W. A. Goddard Iii. Shock waves in high-energy materials: The initial chemical events in nitramine rdx. *Physical Review Letters*, 91(9):98301, 2003.

[64] A. K. Rappe and W. A. Goddard Iii. Charge equilibration for molecular dynamics simulations. *The Journal of Physical Chemistry*, 95(8):3358 3363, 1991.

[65] K. Chenoweth, S. Cheung, A.C.T. Van Duin, W.A. Goddard III, and E.M. Kober. Simulations on the thermal decomposition of a poly (dimethylsiloxane) polymer using the reaxff reactive force field. *J. Am. Chem. Soc*, 127(19):7192–7202, 2005.

[66] K. Chenoweth, A.C.T. van Duin, and W.A. Goddard III. ReaxFF reactive force field for molecular dynamics simulations of hydrocarbon oxidation. *J. Phys. Chem. A*, 112(5):1040 1053, 2008.

[67] A. Strachan, E.M. Kober, A.C.T. van Duin, J. Oxgaard, and W.A. Goddard III. Thermal decomposition of rdx from reactive molecular dynamics. *The Journal of chemical physics*, 122:054502, 2005.

[68] M. J. Buehler, A. C. T. van Duin, and W. A. Goddard III. Multiparadigm modeling of dynamical crack propagation in silicon using a reactive force field. *Physical Review Letters*, 96(9):95505, 2006.

[69] M. J. Buehler, A. Cohen, and D. Sen. Multi-paradigm modeling of fracture of a silicon single crystal under mode ii shear loading. *Journal of Algorithms & Computational Technology*, 2(2):203–221, 2008.

[70] D. Sen, C. Thaulow, S. V. Schieffer, A. Cohen, and M. J. Buehler. Atomistic study of crack-tip cleavage to dislocation emission transition in silicon single crystals. *Physical Review Letters*, 104(23), 2010.

[71] D. E. Yilmaz, C. Bulutay, and T. agin. Pathways of bond topology transitions at the interface of silicon nanocrystals and amorphous silica matrix. *Physical Review B*, 77(15):155306, 2008.

[72] T. C. Germann, K. Kadau, and P. S. Lomdahl. 25 tflop/s multibillion-atom molecular dynamics simulations and visualization/analysis on bluegene/l. In *Proc. Supercomputing*, pages –, 2005.

[73] T. C. Germann and K. Kadau. Trillion-atom molecular dynamics becomes a reality. *Int. J. Mod. Phys. C*, 19:1315–1319, 2008.

[74] K. Kadau, T. C. Germann, P. S. Lomdahl, and B. L. Holian. Microscopic view of structural phase transitions induced by shock waves. *Science*, 296:1681 1684, 2002.

[75] A. Nakano, R.K. Kalia, K. Nomura, A. Sharma, P. Vashishta, F. Shimojo, A.C.T. van Duin, W.A. Goddard, R. Biswas, and D. Srivastava. A divide-and-conquer/cellular-decomposition framework for million-to-billion atom simulations of chemical reactions. *Computational Materials Science*, 38(4):642–652, 2007.

[76] R. Phillips and M. S. Kuczma. Crystals, defects and microstructures: modeling across scales. *Applied Mechanics Reviews*, 55:B42, 2002.

[77] P. Hohenberg and W. Kohn. Inhomogeneous electron gas. *Physical Review*, 136(3B):864 871, 1964.

[78] W. Kohn and L. J. Sham. Self-consistent equations including exchange and correlation effects. *Physical Review*, 140(4A):1133–1138, 1965.

[79] M. C. Payne, M. P. Teter, D. C. Allan, T. A. Arias, and J. D. Joannopoulos. Iterative minimization techniques for ab initio total-energy calculations: molecular dynamics and conjugate gradients. *Reviews of Modern Physics*, 64(4):1045–1097, 1992.

[80] A. Szabo and N. S. Ostlund. *Modern quantum chemistry*. McGraw-Hill New York, 1989.

[81] F. F. Abraham, J. Q. Broughton, N. Bernstein, and E. Kaxiras. Spanning the length scales in dynamic simulation. *Computers in Physics*, 12:538, 1998.

[82] J. Q. Broughton, F. F. Abraham, N. Bernstein, and E. Kaxiras. Concurrent coupling of length scales: methodology and application. *Physical Review B*, 60(4):2391–2403, 1999.

[83] E. B. Tadmor, M. Ortiz, and R. Phillips. Quasicontinuum analysis of defects in solids. *Philosophical Magazine A*, 73(6):1529–1563, 1996.

[84] J. Knap and M. Ortiz. An analysis of the quasicontinuum method. *Journal of the Mechanics and Physics of Solids*, 49(9):1899–1923, 2001.

[85] W. A. Curtin and R. E. Miller. Atomistic/continuum coupling in computational materials science. *Modelling and Simulation in Materials Science and Engineering*, 11:R33, 2003.

[86] M. J. Buehler. Nature designs tough collagen: Explaining the nanostructure of collagen fibrils. *Proceedings of the National Academy of Sciences*, 103(33):12285, 2006.

[87] D. Sen and M. J. Buehler. Chemical complexity in mechanical deformation of metals. *Int. J. for Multiscale Comput. Engg*, 5:181–202, 2007.

[88] D. H. Tsai. The virial theorem and stress calculation in molecular dynamics. *The Journal of Chemical Physics*, 70:1375, 1979.

[89] M. Zhou. A new look at the atomic level virial stress: on continuum-molecular system equivalence. *Proceedings of the Royal Society A: Mathematical, Physical and Engineering Sciences*, 459(2037):2347–2392, 2003.

[90] J. Li. Least-square atomic strain, http://mt.seas.upenn.edu/archive/graphics/a/annotate_atom

[91] J. A. Zimmerman, C. L. Kelchner, P. A. Klein, J. C. Hamilton, and S. M. Foiles. Surface step effects on nanoindentation. *Physical Review Letters*, 87(16):165507, 2001.

[92] C.L. Kelchner, SJ Plimpton, and JC Hamilton. Dislocation nucleation and defect structure during surface indentation. *Physical Review B*, 58(17):11085–11088, 1998.

[93] D. Faken and H. Jónsson. Systematic analysis of local atomic structure combined with 3d computer graphics. *Computational Materials Science*, 2(2):279–286, 1994.

[94] W. Humphrey, A. Dalke, and K. Schulten. VMD: visual molecular dynamics. *Journal of molecular graphics*, 14(1):33–38, 1996.

[95] J. Li. Atomeye: an efficient atomistic configuration viewer. *Modelling and Simulation in Materials Science and Engineering*, 11(2):173–177, 2003.

[96] D.L. Thompson, J.A. Braun, R. Ford, Visualiztion, and Inc Imagery Solutions. *OpenDX: Paths to Visualization.* Visualization and imagery solutions, Inc., 2001.

[97] A. Stukowski. Visualization and analysis of atomistic simulation data with ovito–the open visualization tool. *Modelling and Simulation in Materials Science and Engineering*, 18:015012, 2010.

[98] O. Wilhelmsson, M. Rasander, M. Carlsson, E. Lewin, B. Sanyal, U. Wiklund, O. Eriksson, and U. Jansson. Design of nanocomposite low-friction coatings. *Advanced Functional Materials*, 17(10):1611–1616, 2007.

[99] Y. S. Lee, E. D. Wetzel, and N. J. Wagner. The ballistic impact characteristics of kevlar woven fabrics impregnated with a colloidal shear thickening fluid. *Journal of Materials Science*, 38(13):2825–2833, 2003.

[100] D. Sen and M. J. Buehler. Shock loading of bone-inspired metallic nanocomposites. *Solid State Phenomena*, 139:11–22, 2008.

[101] E. Menendez, G. Salazar-Alvarez, A. P. Zhilyaev, S. Surinach, M. D. Baro, J. Nogues, and J. Sort. Cold consolidation of metal-ceramic nanocomposite powders with large ceramic fractions. *Advanced Functional Materials*, 18(20):3293–3298, 2008.

[102] A. M. Leach, M. McDowell, and K. Gall. Deformation of top-down and bottom-up silver nanowires. *Advanced Functional Materials*, 17(1):43–53, 2007.

[103] I. Jager and P. Fratzl. Mineralized collagen fibrils: A mechanical model with a staggered arrangement of mineral particles. *Biophysical Journal*, 79(4):1737–1746, 2000.

[104] M. J. Buehler. Molecular nanomechanics of nascent bone: fibrillar toughening by mineralization. *Nanotechnology*, 18(295102):295102, 2007.

[105] N.C. Broedling, A. Hartmaier, M.J. Buehler, and H. Gao. The strength limit in a bio-inspired metallic nanocomposite. *J. Mech. Phys. Sol.*, 56(3):1086–1104, 2008.

[106] D. Sen and M.J. Buehler. Size and geometry effects on flow stress in bioinspired de novo metal-matrix nanocomposites. *Advanced Engineering Materials*, 11(10):774–781, 2009.

[107] Y. Mishin, M. J. Mehl, D. A. Papaconstantopoulos, A. F. Voter, and J. D. Kress. Structural stability and lattice defects in copper: Ab initio, tight-binding, and embedded-atom calculations. *Physical Review B*, 63(22):224106, 2001.

[108] M.J. Buehler and H. Gao. Dynamical fracture instabilities due to local hyperelasticity at crack tips. *Nature*, 439:307–310, 2006.

[109] S. P. Chen, D. J. Srolovitz, and A. F. Voter. Computer simulation on surfaces and [001] symmetric tilt grain boundaries in ni, al and ni 3 al. *J. Mater. Res*, 1989, 1989.

[110] J. A. Zimmerman, H. Gao, and F. F. Abraham. Generalized stacking fault energies for embedded atom fcc metals. *Modelling and Simulation in Materials Science and Engineering*, 8(2):103–116, 2000.

[111] J. R. Rice. Dislocation nucleation from a crack tip: an analysis based on the peierls concept. *J. Mech. Phys. Solids*, 40(2):239–271, 1992.

[112] Z. Bangwei and O. Yifang. Theoretical calculation of thermodynamic data for bcc binary alloys with the embedded-atom method. *Physical Review B*, 48(5):3022–3029, 1993.

[113] J. W. D. Connolly and A. R. Williams. Density-functional theory applied to phase transformations in transition-metal alloys. *Physical Review B*, 27(8):5169–5172, 1983.

[114] E. O. Hall. The deformation and ageing of mild steel: Iii discussion of results. *Proceedings of the Physical Society. Section B*, 64:747–753, 1951.

[115] N. J. Petch. The cleavage strength of polycrystals. *J. Iron Steel Inst*, 174(1):25–28, 1953.

[116] J. Schiøtz, FD Di Tolla, and KW Jacobsen. Softening of nanocrystalline metals at very small grain sizes. *Nature*, 391:561, 1998.

[117] TG Nieh and J. Wadsworth. Hall-petch relation in nanocrystalline solids. *Scripta Metallurgica et Materialia*, 25(4):955–958, 1991.

[118] S. Yip. The strongest size. *Nature*, 391(6667):532–533, 1998.

[119] M. Chen, E. Ma, K.J. Hemker, H. Sheng, Y. Wang, and X. Cheng. Deformation twinning in nanocrystalline aluminum. *Science*, 300(5623):1275, 2003.

[120] M.A. Haque and M.T.A. Saif. Mechanical behavior of 30-50 nm thick aluminum films under uniaxial tension. *Scripta Materialia*, 47(12):863–867, 2002.

[121] MA Haque and MTA Saif. Deformation mechanisms in free-standing nanoscale thin films: A quantitative in situ transmission electron microscope study. *Proceedings of the National Academy of Sciences of the United States of America*, 101(17):6335, 2004.

[122] AH Chokshi, A. Rosen, J. Karch, and H. Gleiter. On the validity of the hall-petch relationship in nanocrystalline materials. *Scripta Metallurgica*, 23(10):1679–1684, 1989.

[123] Z. Shan, EA Stach, JMK Wiezorek, JA Knapp, DM Follstaedt, and SX Mao. Grain boundary-mediated plasticity in nanocrystalline nickel. *Science*, 305(5684):654, 2004.

[124] XZ Liao, F. Zhou, EJ Lavernia, SG Srinivasan, MI Baskes, DW He, and YT Zhu. Deformation mechanism in nanocrystalline al: Partial dislocation slip. *Applied Physics Letters*, 83(4):632–634, 2003.

[125] H. Tada, P. C. Paris, and G. R. Irwin. *The Stress Analysis of Cracks Handbook*. ASME Press, New York, 2000.

[126] S. Ogata, J. Li, and S. Yip. Ideal pure shear strength of aluminum and copper. *Science*, 298(5594):807, 2002.

[127] EB Tadmor and S. Hai. A peierls criterion for the onset of deformation twinning at a crack tip. *Journal of the Mechanics and Physics of Solids*, 51(5):765–793, 2003.

[128] Y. Sun and G.E. Beltz. Dislocation nucleation from a crack tip: a formulation based on anisotropic elasticity. *Journal of the Mechanics and Physics of Solids*, 42(12):1905–1932, 1994.

[129] D. Sen and M. J. Buehler. Crystal size controlled deformation mechanism: Breakdown of dislocation mediated plasticity in single nanocrystals under geometric confinement. *Physical Review B*, 77(19):195439, 2008.

[130] J. Schiotz and K.W. Jacobsen. A maximum in the strength of nanocrystalline copper. *Science*, 301(5638):1357, 2003.

[131] H. Van Swygenhoven, PM Derlet, and A. Hasnaoui. Atomic mechanism for dislocation emission from nanosized grain boundaries. *Physical Review B*, 66(2):24101, 2002.

[132] V. Yamakov, D. Wolf, S.R. Phillpot, A.K. Mukherjee, and H. Gleiter. Dislocation processes in the deformation of nanocrystalline aluminium by molecular-dynamics simulation. *Nature Materials*, 1(1):45 49, 2002.

[133] M.J. Buehler, A. Hartmaier, and H. Gao. Hierarchical multi-scale modelling of plasticity of submicron thin metal films. *Modelling and Simulation in Materials Science and Engineering*, 12:S391, 2004.

[134] M.R. Sørensen, M. Brandbyge, and K.W. Jacobsen. Mechanical deformation of atomic-scale metallic contacts: structure and mechanisms. *Physical Review B*, 57(6):3283–3294, 1998.

[135] B. H. Ji and H. J. Gao. Mechanical properties of nanostructure of biological materials. *Journal Of The Mechanics And Physics Of Solids*, 52(9):1963 1990, 2004.

[136] D. M. DeLongchamp and P. T. Hammond. High-contrast electrochromism and controllable dissolution of assembled prussian blue/polymer nanocomposites. *Advanced Functional Materials*, 14(3):224–232, 2004.

[137] A.A. Griffith. The phenomena of rupture and flow in solids. *Philosophical transactions of the royal society of london. Series A*, 221:163–198, 1921.

[138] GI Barenblatt. The mathematical theory of equilibrium cracks in brittle fracture. *Advances in applied mechanics*, 7(55-129):104, 1962.

[139] L. J. Gibson and M. F. Ashby. *Cellular solids: structure and properties*. Cambridge Univ Pr, 1999.

[140] F. E. Round, R. M. Crawford, and D. G. Mann. *The diatoms: biology & morphology of the genera*. Cambridge Univ Press, Cambridge, 1990.

[141] N. Krger. Prescribing diatom morphology: toward genetic engineering of biological nanomaterials. *Current opinion in chemical biology*, 11(6):662–669, 2007.

[142] D. Losic, J. G. Mitchell, and N. H. Voelcker. Diatomaceous lessons in nanotechnology and advanced materials. *Advanced Materials*, 21(29):2947–2958, 2009.

[143] N. Lundholm, O. Moestrup, G. R. Hasle, and K. Hoef-Emden. A study of the pseudo-nitzschia pseudodelicatissima/cuspidata complex (bacillariophyceae): what is p. pseudodelicatissima? *Journal of Phycology*, 39(4):797–813, 2003.

[144] S. W. Fowler and N. S. Fisher. Viability of marine phytoplankton in zooplankton fecal pellets. *Deep Sea Research Part A. Oceanographic Research Papers*, 30(9):963–969, 1983.

[145] C. Hamm and V. Smetacek. Armor: why, when, and how. *Evolution of Primary Producers in the Sea*, pages 311–332, 2007.

[146] T. Yanagisawa, T. Shimizu, K. Kuroda, and C. Kato. Trimethylsilyl derivatives of alkyltrimethylammonium-kanemite complexes and their conversion to microporous silica materials. *Bull. Chem. Soc. Jpn*, 63:1535–1537, 1990.

[147] N. K. Raman, M. T. Anderson, and C. J. Brinker. Template-based approaches to the preparation of amorphous, nanoporous silicas. *Chem. Mater*, 8(8):1682–1701, 1996.

[148] H. Ni, X. Li, and H. Gao. Elastic modulus of amorphous sio nanowires. *Applied Physics Letters*, 88:043108, 2006.

[149] L. Tong, J. Lou, Z. Ye, G. T. Svacha, and E. Mazur. Self-modulated taper drawing of silica nanowires. *Nanotechnology*, 16:1445–1448, 2005.

[150] X. D. Han, K. Zheng, Y. F. Zhang, X. N. Zhang, Z. Zhang, and Z. L. Wang. Low-temperature in situ large-strain plasticity of silicon nanowires. *ADVANCED MATERIALS-DEERFIELD BEACH THEN WEINHEIM-*, 19(16):2112, 2007.

[151] A. P. Garcia, D. Sen, and M. J. Buehler. Hierarchical silica nanostructures inspired by diatom algae yield superior deformability, toughness and strength. *Metallurgical and Materials Transactions A*, accepted, 2010.

[152] A. P. Garcia and M. J. Buehler. Bioinspired nanoporous silicon provides great toughness at great deformability. *Computational Materials Science*, 48(2):303–309, 2010.

[153] D. E. Yilmaz, C. Bulutay, and T. agin. Analysis of strain fields in silicon nanocrystals. *Applied Physics Letters*, 94:191914, 2009.

[154] A. Thompson. Grasp (general reactive atomistic simulation program), http://www.cs.sandia.gov/capabilities/materialsmodelingsimulation/index.html.

[155] G. M. Rignanese, A. De Vita, J. C. Charlier, X. Gonze, and R. Car. First-principles molecular-dynamics study of the (0001) -quartz surface. *Physical Review B*, 61(19):13250–13255, 2000.

[156] A. P. Garcia. Hierarchical and size dependent mechanical properties of silica and silicon nanostructures inspired by diatom algae. Master's thesis, MIT, 2010.

[157] E.C.C.M. Silva, J. Li, D. Liao, S. Subramanian, T. Zhu, and S. Yip. Atomic scale chemo-mechanics of silica: nano-rod deformation and water reaction. *Journal of Computer-Aided Materials Design*, 13(1):135–159, 2006.

[158] H. D. Espinosa, J. E. Rim, F. Barthelat, and M. J. Buehler. Merger of structure and material in nacre and bone-perspectives on de novo biomimetic materials. *Progress in Materials Science*, 54(8):1059–1100, 2009.

[159] D. Losic, J. G. Mitchell, R. Lal, and N. H. Voelcker. Rapid fabrication of micro- and nanoscale patterns by replica molding from diatom biosilica. *Advanced Functional Materials*, 17(14):2439 2446, 2007.

[160] M. Hildebrand. Diatoms, biomineralization processes, and genomics. *Chem. Rev*, 108(11):4855 4874, 2008.

[161] S. L. Walter, B. D. Flinn, and G. Mayer. Mechanisms of toughening of a natural rigid composite. *Materials Science and Engineering: C*, 27(3):570 574, 2007.

[162] C. Levi, J. L. Barton, C. Guillemet, E. Bras, and P. Lehuede. A remarkably strong natural glassy rod: the anchoring spicule of themonorhaphis sponge. *Journal of Materials Science Letters*, 8(3):337 339, 1989.

[163] M. Sarikaya, H. Fong, N. Sunderland, B. D. Flinn, G. Mayer, A. Mescher, and E. Gaino. Biomimetic model of a sponge-spicular optical fiber-mechanical properties and structure. *J. Mater. Res.*, 16(5):1420 1428, 2001.

[164] D. Sen, A. P. Garcia, and M. J. Buehler. Mechanics of nano-honeycomb silica structures: A size-dependent brittle-to-ductile transition. *under review.*

[165] D. Sen and M. J. Buehler. Atomistically-informed mesoscale model of deformation and failure of bioinspired hierarchical silica nanocomposites. *International Journal of Applied Mechanics*, 2(4), 2010.

[166] A. Carpinteri, B. Chiaia, and S. Invernizzi. Numerical analysis of indentation fracture in quasi-brittle materials. *Engineering Fracture Mechanics*, 71(4-6):567–577, 2004.

[167] M. Ostoja-Starzewski. Lattice models in micromechanics. *Applied Mechanics Reviews*, 55:35–60, 2002.

[168] G. A. Buxton, C. M. Care, and D. J. Cleaver. A lattice spring model of heterogeneous materials with plasticity. *Modelling and Simulation in Materials Science and Engineering*, 9:485–497, 2001.

[169] M. Grah, K. Alzebdeh, P. Y. Sheng, M. D. Vaudin, K. J. Bowman, and M. Ostoja-Starzewski. Brittle intergranular failure in 2d microstructures: Experiments and computer simulations. *Acta Materialia*, 44(10):4003–4018, 1996.

[170] E. Schlangen and E. J. Garboczi. Fracture simulations of concrete using lattice models: computational aspects. *Engineering Fracture Mechanics*, 57(2-3):319–332, 1997.

[171] W. A. Curtin and H. Scher. Brittle fracture in disordered materials: A spring network model. *Journal of Materials Research*, 5(3):535–553, 1990.

[172] G. N. Hassold and D. J. Srolovitz. Brittle fracture in materials with random defects. *Physical Review B*, 39(13):9273–9281, 1989.

[173] T. Scholz, G. A. Schneider, J. Munoz-Saldana, and M. V. Swain. Fracture toughness from submicron derived indentation cracks. *Applied Physics Letters*, 84:3055, 2004.

[174] M. W. Barsoum. *Fundamentals of ceramics.* Taylor & Francis, New York, 2003.

[175] S. Plimpton. Fast parallel algorithms for short-range molecular dynamics. *Journal of Computational Physics*, 117(1):1–19, 1995.

[176] J. A. Begley and J. D. Landes. The j integral as a fracture criterion. In *Fracture Toughness, Proceedings of the 1971 National Symposium on Fracture Mechanics, Part II*, pages 1–20–. ASTM, 1972.

[177] J. R. Rice. A path independent integral and the approximate analysis of strain concentration by notches and cracks. *Journal of applied mechanics*, 35(2):379–386, 1968.

[178] B. Moran and C. F. Shih. Crack tip and associated domain integrals from momentum and energy balance. *Engineering Fracture Mechanics*, 27(6):615 642, 1987.

[179] R. Khare, S. L. Mielke, J. T. Paci, S. Zhang, R. Ballarini, G. C. Schatz, and T. Belytschko. Coupled quantum mechanical/molecular mechanical modeling of the fracture of defective carbon nanotubes and graphene sheets. *Physical Review B*, 75(7):75412, 2007.

[180] Y. Jin and F. G. Yuan. Atomistic simulations of j-integral in 2d graphene nanosystems. *Journal of Nanoscience and Nanotechnology*, 5(12):2099–2107, 2005.

[181] A. G. McLellan. Virial theorem generalized. *American Journal of Physics*, 42:239, 1974.

[182] C. D. Bencher, A. Sakaida, K. T. V. Rao, and R. O. Ritchie. Toughening mechanisms in ductile niobium-reinforced niobium aluminide (nb/nb 3 al) in situ composites. *Metallurgical and Materials Transactions A*, 26(8):2027–2033, 1995.

[183] B. T. Polyak. The conjugate gradient method in extremal problems* 1. *USSR Computational Mathematics and Mathematical Physics*, 9(4):94–112, 1969.

[184] R. K. Nalla, J. J. Kruzic, J. H. Kinney, and R. O. Ritchie. Mechanistic aspects of fracture and r-curve behavior in human cortical bone. *Biomaterials*, 26(2):217–231, 2005.

[185] T. Ackbarow, D. Sen, C. Thaulow, and M. J. Buehler. Alpha-helical protein networks are self-protective and flaw-tolerant. *PloS one*, 4(6):e6015, 2009.

[186] R.O. Ritchie, M.J. Buehler, and P.K. Hansma. Plasticity and toughness in bone. *Phys. Today*, 62(6):41–47, 2009.

[187] A. Carpinteri and N.M. Pugno. Mechanics of hierarchical materials. *International Journal of Fracture*, 150(1):221–226, 2008.

[188] S. Bechtle, S.F. Ang, and G.A. Schneider. On the mechanical properties of hierarchically structured biological materials. *Biomaterials*, 2010.

[189] H. Yao and H. Gao. Mechanics of robust and releasable adhesion in biology: bottom-up designed hierarchical structures of gecko. *Journal of the Mechanics and Physics of Solids*, 54(6):1120–1146, 2006.

[190] H. Yao and H. Gao. Multi-scale cohesive laws in hierarchical materials. *International Journal of Solids and Structures*, 44(25-26):8177 8193, 2007.

[191] T. Ackbarow and M.J. Buehler. Alpha-helical protein domains unify strength and robustness through hierarchical nanostructures. *Nanotechnology*, 20:075103, 2009.

[192] Z. Qin, S. Cranford, T. Ackbarow, and M.J. Buehler. Robustness-strength performance of hierarchical alpha-helical protein filaments. *International Journal of Applied*, 1(1):85 112, 2009.

[193] M.J. Buehler. Tu(r)ning weakness to strength. *Nano Today*, 2010.

[194] A. Berman, L. Addadi, A. Kvick, L. Leiserowitz, M. Nelson, and S. Weiner. Intercalation of sea urchin proteins in calcite: study of a crystalline composite material. *Science*, 250(4981):664, 1990.

[195] J. Aizenberg. Nanomechanics of biological single crystals. *Nanomechanics of Materials and Structures*, pages 99–108, 2006.

[196] CL Malik, SM Stover, RB Martin, and JC Gibeling. Equine cortical bone exhibits rising r-curve fracture mechanics. *Journal of biomechanics*, 36(2):191–198, 2003.

[197] J.J. Kruzic, R.K. Nalla, J.H. Kinney, and RO Ritchie. Crack blunting, crack bridging and resistance-curve fracture mechanics in dentin: effect of hydration. *Biomaterials*, 24(28):5209–5221, 2003.

[198] F. Barthelat. Biomimetics for next generation materials. *Philosophical Transactions of the Royal Society A: Mathematical, Physical and Engineering Sciences*, 365(1861):2907, 2007.